Terahertz magnetospectroscopy of HgTe-based heterostructure materials

Dissertation

zur Erlangung des Doktorgrades
der Naturwissenschaften (Dr. rer. nat.)
der Fakultät Physik
der Universität Regensburg

vorgelegt von

Maximilian Otteneder

aus Passau

im Jahr 2021

Promotionsgesuch eingereicht am: 25.10.2021

Die Arbeit wurde angeleitet von: Prof. Dr. Sergey D. Ganichev

Prüfungsauschuss

Vorsitzender: Prof. Dr. Jaroslav Fabian

1. Gutachter: Prof. Dr. Sergey D. Ganichev

2. Gutachter: Prof. Dr. Christian Schüller

weiterer Prüfer: Prof. Dr. Jörg Wunderlich

Contents

1 Introduction

Since its first synthesis in 1958, mercury cadmium telluride (HgCdTe or MCT) has become one of the most prominent materials for infrared detection because of its highly tunable band gap that covers a wide range of frequencies from the near infrared up to the terahertz range [1, 2]. In the early years, this material was considered so significant that the research in the United States was even classified until the late '60s because of its potential military applications [2]. Due to this technological importance, great efforts have been made to enhance the fabrication technologies for growing MCT-based crystals and heterostructures, resulting in a well-controlled fabrication process that allows for high material quality and carrier mobilities nowadays [3–5]. Besides conventional narrow-gap semiconductors or semimetals, it is also possible to realize novel, topological phases in the MCT material class. This is attributed to the peculiar band structure of mercury telluride (HgTe), where strong spin-orbit coupling leads to an energetic inversion of the s- and p-like bands [6, 7]. Topologically non-trivial phases can be realized, e.g., in $Cd_xHg_{1-x}Te$ crystals with cadmium contents x below a specific temperature-dependent critical value x_c [8, 9], or in two-dimensional CdTe/HgTe/CdTe quantum well (QW) structures wider than the critical thickness $d_c \approx 6.3\,\mathrm{nm}$ [10–12]. In these systems, time-reversal symmetry-protected boundary states with extraordinary properties form at the interface to trivially insulating materials [7, 13]. These states exhibit a linear energy dispersion that is described by the Dirac equation for massless particles [14]. Due to a locking of spin and momentum directions, they are effectively protected from backscattering, yielding dissipationless electrical transport of the boundary states [12].

While the existence of these protected boundary states in the MCT system was already predicted in the '80s [15, 16], it took two decades until technological advancements in material fabrication enabled the experimental observation of the helical edge states in HgTe quantum wells in the context of the quantum spin Hall effect [10, 11]. From that point on, extensive studies of MCT-based materials led to the observation of a variety of fascinating phenomena, such as terahertz radiation-induced photocurrents carried by the helical edge states in topologically non-trivial HgTe QWs [17], or surface state cyclotron resonance in three-dimensional topologically insulating strained HgTe films [18, 19]. Furthermore, giant terahertz-induced photocurrents were detected in HgTe QWs

corresponding to topologically trivial and non-trivial phases [20] as well as the Dirac-like transition regime where the band gap shrinks to zero [21]. These findings demonstrate that optoelectronic techniques, such as photocurrent or photoconductivity measurements, provide very powerful methods for the study of the electronic properties of such systems, important for both fundamental science as well as applications. In particular, this approach allows to optically probe spin-dependent phenomena [22] involving the spin-momentum-locked topological boundary states. For such studies, the terahertz (THz) range of frequencies is of particular importance since it provides photon energies that are smaller than the bulk energy gap in these materials, which effectively prevents the optical excitation of bulk carriers across the gap. Consequently, this work is devoted to the study of MCT-based heterostructures employing techniques such as terahertz spectroscopy and magnetophotoconductivity. Despite the number of investigations that have already been carried out on this material class, there are still many open questions to be answered. An important goal of this work is to obtain a better understanding of the topological boundary states in these materials and their influence on electro-optical effects. The investigations focus on two-dimensional HgTe quantum wells as well as three-dimensional $Cd_xHg_{1-x}Te$ films in both topologically trivial and non-trivial regimes. Using continuous and pulsed terahertz excitation, fascinating optoelectronic phenomena were discovered in the course of this study.

A detailed investigation of the terahertz photoconductivity in HgTe QWs with inverted and non-inverted parabolic as well as linear band dispersion revealed that these structures manifest a distinct sign-alternating photoresponse in magnetic field [23]. Upon increase of the external, out-of-plane magnetic field, the photoconductivity systematically changes its sign. This remarkable effect was observed in QWs corresponding to both topologically trivial and non-trivial regimes. Additionally, it was studied in samples with different geometries including conventional Hall bar and Corbino disk design. Notably, the analysis of the photoconductivity in Corbino disk samples brought up an elegant optoelectronic method to probe the carrier mobility in such systems.

During the research on the sign-alternating photoconductivity, a qualitatively different behavior of the photoresponse was observed in a high-mobility 20 nm QW. Instead of a single or double sign inversion in magnetic field, pronounced ω/ω_c-periodic oscillations were observed in photoresistivity for the Fermi energy lying in the conduction band [23]. Further analysis demonstrated that

these oscillations have the same origin as microwave-induced resistance oscillations (MIRO), which have previously been observed only in systems with ultra-high mobility, such as ultra-clean high-mobility GaAs quantum wells, under illumination with microwave radiation [24–26]. Similar to Shubnikov-de Haas oscillations, which result from an interplay of Fermi energy E_F and cyclotron energy $\hbar\omega_\mathrm{c}$, MIRO express the commensurability between the photon energy $\hbar\omega$ and $\hbar\omega_\mathrm{c}$. Recently, their terahertz analogue, the terahertz-induced resistance oscillations (TIRO), were observed in GaAs quantum wells [27, 28] as well as in three-dimensional HgTe topological insulators [29]. The results presented in this work represent the first observation of such MIRO-like oscillations in HgTe quantum wells.

In addition to two-dimensional systems, the optoelectronic properties of three-dimensional $\mathrm{Cd}_x\mathrm{Hg}_{1-x}\mathrm{Te}$ films were studied in the last part of this thesis. The investigation of topologically non-trivial $\mathrm{Cd}_x\mathrm{Hg}_{1-x}\mathrm{Te}$ films with an inverted band ordering revealed cyclotron resonance involving the two-dimensional surface states [30]. The surface state resonance was detected in terahertz radiation transmission as well as photogalvanic experiments. However, it was absent in the investigated $\mathrm{Cd}_x\mathrm{Hg}_{1-x}\mathrm{Te}$ films with higher cadmium contents corresponding to the topologically trivial regime, demonstrating the origin of the resonance in the surface state carriers. Moreover, experiments with different film designs showed the importance of sharp interfaces between topologically trivial and non-trivial layers for the formation of fully two-dimensional topological surface states.

This thesis is arranged in the following way: Chapter 2 covers the essential concepts and phenomena relevant for this work. First, the concept of topological insulators and their basic properties are outlined in Sec. 2.1, including a model based on the relativistic Dirac Hamiltonian that allows the description of the time-reversal protected boundary states. In the following, Sec. 2.2 presents the basic properties of bulk cadmium telluride (CdTe) and mercury telluride as well as their respective band dispersions. It is illustrated how topological insulators can be constructed from two-dimensional HgTe quantum wells or three-dimensional $\mathrm{Cd}_x\mathrm{Hg}_{1-x}\mathrm{Te}$ crystals. Section 2.3 gives a short introduction into radiation-induced optoelectronic effects in semiconductors. Particular focus lies on the photogalvanic effect (see Sec. 2.3.1), which is described by a phenomenological approach as well as several microscopic mechanisms including photocurrents in strained topological HgTe films. Furthermore, the effect

of photoconductivity (see Sec. 2.3.2) is outlined phenomenologically and microscopically by considering μ-photoconductivity caused by radiation-induced carrier heating. Section 2.4 introduces the phenomenon of cyclotron resonance in systems with parabolic as well as linear dispersion. In Chap. 3, the experimental methods are described, including the optically pumped terahertz molecular gas laser setup (see Sec. 3.1) and the techniques for electrical signal detection (see Sec. 3.2). Chapter 4 gives an overview on the properties of the investigated samples. During the course of this work, six HgTe quantum wells with various widths (described in Sec. 4.1) and five $Cd_xHg_{1-x}Te$ films with different Cd content (described in Sec. 4.2) were studied. Subsequently, the presentation of the experimental results starts with Chap. 5 and the description of the sign-alternating photoconductivity in HgTe quantum wells. The findings are compared for different QW widths and sample geometries in Sec. 5.1 and afterwards discussed in Sec. 5.2. Chapter 6 continues with the presentation of the MIRO-like oscillatory photoresponse observed in a 20 nm QW. The experimental data are shown in Sec. 6.1 and discussed in Sec. 6.2 in the context of the interplay between cyclotron and photon energies. Chapter 7 is focused on the investigation of the three-dimensional $Cd_xHg_{1-x}Te$ films. The main part of this chapter addresses the cyclotron resonance of topological surface states that was observed in topologically non-trivial samples. The corresponding results are presented in Sec. 7.1. Additionally, resonances caused by magnetic field-mediated ionization of impurities were detected. These are analyzed in Sec. 7.2, followed by a detailed discussion of all results in Sec. 7.3 as well as a theoretical modeling of the topological surface states in $Cd_xHg_{1-x}Te$ films that demonstrates a strong influence of the film design on their properties. Finally, this thesis concludes with a brief summary and an outlook on future investigations in Chap. 8.

2 Physical basics

This chapter introduces the fundamental concepts that are relevant for this thesis. The first section gives an overview of the novel material class of topological insulators and its fascinating properties. Subsequently, the characteristics of bulk CdTe and HgTe, as well as HgTe quantum wells and $Cd_xHg_{1-x}Te$ alloys are presented. In the next section, radiation-induced optoelectronic effects are addressed. Particular focus lies on the photogalvanic effect, photoconductivity, and the phenomenon of cyclotron resonance which is outlined in the last section of this chapter.

2.1 Topological insulators

In the most descriptive way, topological insulators are often portrayed as materials that are insulating in the bulk but host conducting states on their boundary to surrounding vacuum or other non-topological materials [7, 13, 14]. These conducting states can be of different nature. In the most prominent cases, they appear either as two-dimensional surface states enclosing a three-dimensional piece of topological insulator [31], or as one-dimensional edge states in topological insulators where the charge carrier movement is quantum mechanically confined to two dimensions [13]. The existence of this peculiar states originates from the inverted band ordering of topologically non-trivial materials and the resulting crossing of the bands at the interfaces of these materials to topologically trivial ones with a regular band ordering. Because of this necessary band crossing, the band gap of the insulating bulk closes and conducting states with an approximately linear, gapless dispersion emerge at the boundaries [12].

So to put it simply, topologically trivial and non-trivial materials are distinguished by their different band ordering. Mathematically, this is expressed in different values of so called topological invariants. One of these invariants, originally introduced within the mathematical context of fiber bundles but later adopted to the physical context of band structures, is the Chern number c [32]. For the n-th band in a solid-state system, the Chern number [12]

$$c_n = \frac{1}{2\pi} \int_{\mathcal{S}} \boldsymbol{\Omega}_n(\boldsymbol{k}) \, \mathrm{d}^2\boldsymbol{k} \tag{1}$$

can be calculated as an integral over the surface of the Brillouin zone $\mathcal{S}$ using the Berry curvature [14, 33]

$$\boldsymbol{\Omega}_n = \nabla_{\boldsymbol{k}} \times i \left\langle u_{n,\boldsymbol{k}} \right| \nabla_{\boldsymbol{k}} \left| u_{n,\boldsymbol{k}} \right\rangle \ . \tag{2}$$

The latter can be described as a gauge-invariant expression of the geometric properties of the Bloch wave functions $u_{n,\boldsymbol{k}}$ in reciprocal space. Summation over all bands yields the total Chern number $c = \sum_{n=1}^{N} c_n$ of the system. This integer number is a distinct property that remains constant under smooth transformations of the Hamiltonian of the corresponding system. It, however, yields different values for topologically (in the sense of the Chern number or $\mathbb{Z}$-classification) non-identical systems, whose respective Hamiltonians cannot be smoothly transformed into each other without shutting the energy gap [12]. In 1982, it was shown by Thouless, Kohmoto, Nightingale, and den Nijs that in two-dimensional electron systems subjected to a strong perpendicular magnetic field, the Chern number is equal to the Landau level filling factor of the corresponding quantum Hall state. In the quantum Hall effect, the current flow is carried by edge states which naturally arise at the borders of the conduction channel as a consequence of the transition between materials with different Chern numbers. These edge states have the remarkable property that they propagate in opposite directions at opposite edges of the conduction channel, and are therefore called chiral [12]. Because of the lack of accessible states in opposite propagation direction at the same edge, backscattering is not possible, which renders these states robust against disorders [12, 13].

The quantum Hall states require an applied magnetic field that breaks time-reversal symmetry. In strong contrast, the protected boundary states in $\mathbb{Z}_2$ topological insulators arise without external magnetic field, when time-reversal symmetry remains unbroken [12]. Thus, such insulators define a new topological class of materials characterized by their non-trivial $\mathbb{Z}_2$ topological invariant. They exhibit remarkable properties that are linked to both spin-orbit coupling and time-reversal symmetry, which describes the symmetry of physical laws under the time-reversal transformation $t \mapsto -t$. In systems with half-integer spin, such a time reversal is expressed by the anti-unitary operator Θ which reverses the momentum and spin of a Bloch eigenstate of the system according to [14]

$$\Theta \left| u_{n,\boldsymbol{k},\uparrow} \right\rangle = \beta \left| u_{n,-\boldsymbol{k},\downarrow} \right\rangle \ . \tag{3}$$

Here, β is a simple phase factor. The anti-unitary characteristic of Θ leads to the important property $\Theta^2 = -1$ [34] that results in a degeneracy of the systems eigenstates with respect to opposite crystal momenta and spins. A direct consequence of this fact is Kramers theorem, which states that in systems described by a time-reversal symmetric Hamiltonian, every energy state is degenerate at least twice but either case even-numbered [12, 14]. In systems without spin-orbit interaction, this degeneracy is simply expressed in the spin degeneracy of every state [12]. However, when spin-orbit interaction lifts the spin degeneracy, Eq. (3) ensures the existence of states where the momentum and the spin direction are strongly coupled. These so called helical states have the peculiar property that states with equal spin orientation move in the same spatial direction, whereas an opposing spin alignment of states results in contrary propagation directions [14]. This property is commonly known as spin-momentum locking. An important consequence of this entanglement of spin and momentum is that for helical states, backscattering is forbidden or, to be more precise, possible only for scattering processes that involve a spin flip [14]. In the ideal case, i.e. in the absence of spin-flip scattering, electrical transport of helical states is dissipationless [35].

Another direct consequence of Kramers theorem is that for a time-reversal invariant Hamiltonian, the states are required to be degenerate at points of high symmetry in k-space, e.g. at $k = 0$ and $k = \pi/a$ for one-dimensional edge states. Here, a is the corresponding lattice constant. Away from these time-reversal symmetric k-points, spin-orbit interaction can split the spin-degeneracy and helical boundary states can arise in the gap [12]. However, there are two principally different ways these helical bands can form connecting the degenerate high-symmetry points. They can be linked either pairwise, i.e. two bands emerge and end in the same set of degenerate k-points, as shown in Fig. 1 (a). This leads to an even number of boundary states present in the system at all times independent of the actual Fermi level. In Fig. 1 (a), the bands are exemplarily arranged in such a way that two states are populated for the given Fermi energy E_F. However, by smoothly transforming the corresponding Hamiltonian, the bands can just as well be moved out of the energy gap, which would render the system topologically trivial. The other option, illustrated in Fig. 1 (b), is that the Kramers-degenerate k-points are connected in a way that no bands originate and end in the same two degenerate k-points. In that event, there is always an odd number of intersections of the boundary

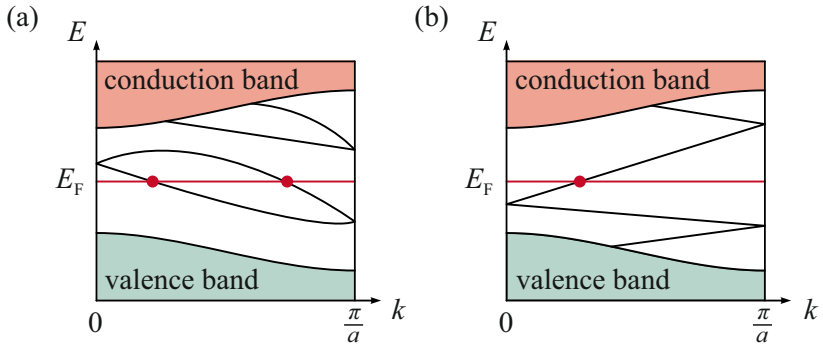

Figure 1: Schematic band dispersions of an insulator with boundary states in the energy gap between the two Kramers-degenerate points $k = 0$ and $k = \pi/a$. In panel (a), the Fermi energy E_F crosses an even number of boundary states, which renders them topologically trivial. In contrast, in (b), the odd number of states crossed by E_F ensures that they are topologically protected. Because of time-reversal symmetry, the second half of the Brillouin zone is a mirror image and not shown here. Adapted from Ref. [12].

states with the Fermi level and the bands can no longer be pushed out of the energy gap by continuous transformations [12]. These two cases are distinguished with the help of the $\mathbb{Z}_2$ topological invariant $\nu \in \{0, 1\}$ [14, 36]. The topologically trivial case sketched in Fig. 1 (a), where the Kramers points are connected pairwise, is characterized by $\nu = 0$ and the edge states are not protected. In contrast, the second situation, depicted in Fig. 1 (b), is characterized by $\nu = 1$ and describes the topologically non-trivial $\mathbb{Z}_2$ phase, where the helical boundary states are protected by time-reversal symmetry. For mathematical definitions of the $\mathbb{Z}_2$ topological invariant see, e.g., Refs. [36] or [14].

For three-dimensional insulators, this classification can be extended analogously with the use of four $\mathbb{Z}_2$ topological invariants $(\nu_0; \nu_1, \nu_2, \nu_3)$ with $\nu_0 \in \{0, 1\}$ and $\nu_1, \nu_2, \nu_3 \in \mathbb{Z}$ [31]. In the surface Brillouin zone of a three-dimensional insulator, Kramers theorem requires the existence of four degenerate, time-reversal symmetric points $\Gamma_{1,2,3,4}$ which now form two-dimensional Dirac points in the surface band structure [14], as sketched in Fig. 2 (c). Again, the decisive criteria for topologically non-trivial behavior is how these Kramers-degenerate points are connected by the surface band dispersion. The number of intersections of the Fermi surface with the straight line linking any pair of time-reversal invariant points Γ_a and Γ_b defines whether the surface states are topologically protected along this momentum direction or not. For each of this possible directions, an even number of intersections results in topologically trivial behavior, whereas for an odd number of crossings, the surface states are topologically protected, in analogy to the situation illustrated in Figs. 1 (a)

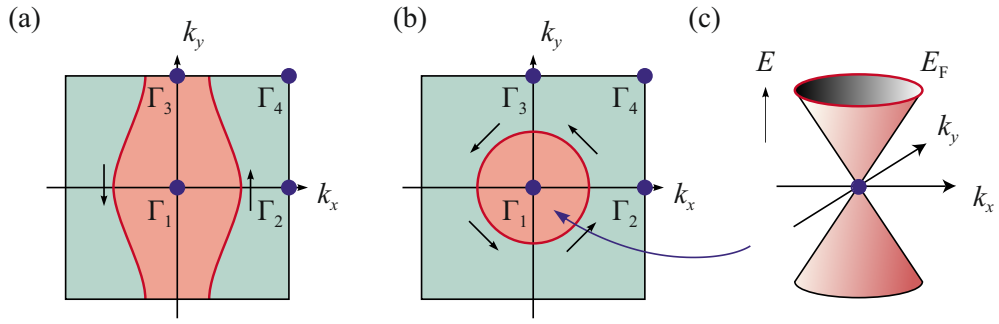

Figure 2: Sketch of the two-dimensional surface-state Brillouin zone with the Kramers invariant points Γ_1, Γ_2, Γ_3, and Γ_4. Red lines exemplarily sketch the evolution of the Fermi energy for a weak topological insulator with $\nu_0 = 0$ (a) and in case of a strong topological insulator described by $\nu_0 = 1$ (b). In the STI depicted in panel (b), the Fermi energy encloses a single Dirac point at Γ_1 with the cone-like band dispersion of the surface states illustrated in panel (c). Adapted from Ref. [12].

and (b) [31]. Figure 2 illustrates two possible shapes of the Fermi surface which result in principally different topological properties. In the first scenario, displayed in Fig. 2 (a), the Fermi surface encloses two Kramers-degenerate points Γ_1 and Γ_3 intersecting the connection lines between pairs Γ_1-Γ_2 and Γ_3-Γ_4. Such a material can, e.g., be constructed by stacking weakly coupled layers of two-dimensional quantum spin Hall insulators in y-direction, as illustrated in Fig. 2 (a) [13]. Under such circumstances, the topologically protected helical edge states of the individual layers form anisotropic surface states which are no longer protected by time-reversal symmetry [13, 14]. This case is referred to as weak topological insulator (WTI) described by $\nu_0 = 0$ and (ν_1, ν_2, ν_3) which may be understood as Miller indices defining the orientation of the layers [12]. In general, the $\mathbb{Z}_2$ topological invariant ν_0 reflects whether the Fermi surface encloses an even ($\nu_0 = 0$) or odd ($\nu_0 = 1$) number of Dirac points [14]. The simplest scenario for the so called strong topological insulator (STI) with $\nu_0 = 1$ is sketched in Fig. 2 (b). Here, the Fermi surface encloses a single Dirac point at Γ_1 and intersects the connection lines between pairs Γ_1-Γ_2 and Γ_1-Γ_3. In contrast to the WTI, in a strong topological insulator, the surface states are protected by time-reversal symmetry and form a unique two-dimensional topological metal where, unlike to an ordinary metal, states are not spin-degenerate [12]. Due to spin-momentum locking, the spin rotates with $\boldsymbol{k}$ around the Fermi surface, which is illustrated by the arrows in Fig. 2 (b).

In general, the dispersion relation of such time-reversal symmetry-protected boundary states can be deduced from the relativistic Dirac Hamiltonian for

spin-1/2 particles [37, 38]

$$\mathcal{H} = c\,\boldsymbol{p}\cdot\boldsymbol{\alpha} + mc^2\beta\ , \tag{4}$$

where c is the speed of light, m and $\boldsymbol{p}$ represent the mass and the momentum of the particle, respectively, and α_i and β denote the Dirac matrices which can be expressed in terms of the Pauli matrices

$$\sigma_x = \begin{pmatrix} 0 & 1 \\ 1 & 0 \end{pmatrix}, \quad \sigma_y = \begin{pmatrix} 0 & -i \\ i & 0 \end{pmatrix}, \quad \sigma_z = \begin{pmatrix} 1 & 0 \\ 0 & -1 \end{pmatrix}\ . \tag{5}$$

In one dimension, the two Dirac matrices α_x and β are any two of the three Pauli matrices, e.g. $\alpha_x = \sigma_x$ and $\beta = \sigma_z$. For the two-dimensional case, the Dirac matrices are equal to the Pauli matrices, i.e. $\alpha_x = \sigma_x$, $\alpha_y = \sigma_y$, and $\beta = \sigma_z$ [14]. In three dimensions, the four-dimensional Dirac matrices are given by

$$\alpha_i = \begin{pmatrix} 0 & \sigma_i \\ \sigma_i & 0 \end{pmatrix} \text{ and } \beta = \begin{pmatrix} \mathbb{1}_2 & 0 \\ 0 & -\mathbb{1}_2 \end{pmatrix}\ , \tag{6}$$

with $\mathbb{1}_2$ being the 2×2 identity matrix. Solving the Schrödinger equation yields the associated eigenenergies of the Dirac Hamiltonian [14]

$$E_\pm = \pm\sqrt{m^2c^4 + p^2c^2}\ . \tag{7}$$

Here, the two positive solutions describe an electron in spin-up and spin-down state, whereas the negative solutions define the energy of a positron in either spin-up or spin-down configuration. These two particle dispersions are separated by an energy gap of $2mc^2$. In the case of a vanishing particle mass, the mass-proportional term in Eq. (7) becomes zero and the dispersion is described by $E_\pm = \pm\,|cp|$ linear in velocity and momentum. It is important to note that the Dirac equation is symmetrical in its positive and negative energy solutions and, therefore, invariant under the transformation $m \to -m$ and $\beta \to -\beta$ [14].

The Dirac equation for massless spin-1/2 particles is a good starting point for the description of boundary states in topological insulators. In solid-state systems, the solutions with different signs correspond to electron and hole states, each double-degenerate reflecting the two different spin configurations.

However, due to the symmetry of the Dirac equation, a topological distinction between systems with positive mass (i.e. positive electron dispersion and negative hole dispersion) and negative mass (resulting in negative electronic and positive hole energies) is not possible [38]. The easiest way to resolve this problem is to simply assign the first case as topologically non-trivial. A physically more accurate attempt is to introduce a quadratic correction to the rest-mass term in the Dirac Hamiltonian given by Eq. (4) to topologically distinguish between these two cases: [14]

$$\mathcal{H} = v\ \boldsymbol{p}\cdot\boldsymbol{\alpha} + \left(mc^2 - \widetilde{B}\boldsymbol{p}^2\right)\beta \tag{8}$$

Here, the speed of light has been replaced with the velocity v of the charge carriers in the solid and $\widetilde{B}$ is a parameter with the dimension of inverse mass. The quadratic correction proportional to $\widetilde{B}$ breaks the symmetry for positive and negative masses [14]. Under the condition $m\widetilde{B} > 0$, Eq. (8) is topologically distinct from the original Dirac Hamiltonian and describes a topologically non-trivial system (corresponding to a $\mathbb{Z}_2$ invariant of $\nu = 1$) which hosts protected boundary states [38]. In contrast, for $m\widetilde{B} \leq 0$, Eq. (8) characterizes a topologically trivial system with $\nu = 0$ [38]. In the framework of this modified Dirac Hamiltonian, a two-dimensional topological insulator with a boundary at $x = 0$ is then described by [14]

$$\mathcal{H}_{\mathrm{2D}} = vp_x\sigma_x \pm vp_y\sigma_y + \left(mv^2 - \widetilde{B}p^2\right)\sigma_z\ . \tag{9}$$

Using the relation $p_i = \hbar k_i$, the dispersion of the topologically protected states forming at the interface to a topologically trivial material at $x = 0$ is then given by

$$E_{\pm} = \pm v\hbar k_y\,\mathrm{sgn}(\widetilde{B}) \propto k_y\ , \tag{10}$$

where the plus and minus sign reflect the different spin configurations of the helical edge states propagating along the edge [14]. An analysis of the corresponding eigenstates shows that the current density of the spin current which is carried by the edge states decays exponentially away from the boundary [14]. In case of a three-dimensional topological insulator, the resulting surface states at the interface to a topologically trivial material (which is exemplarily

defined as the yz-plane) are characterized by [14]

$$E_{\pm} = \pm v\hbar\,\mathrm{sgn}(\widetilde{B})\sqrt{k_y^2 + k_z^2} \propto \sqrt{k_y^2 + k_z^2}\ . \tag{11}$$

This defines a Dirac cone dispersion of the two-dimensional protected states on the surface of the TI, as illustrated in Fig. 2 (c).

As already pointed out earlier, spin-orbit interaction is an important prerequisite for the formation of protected boundary states in topologically insulating materials since it lifts the spin degeneracy away from the Kramers-invariant points in k-space. In general, spin-orbit coupling (SOC) has to be considered when a charged particle moves inside an electrostatic potential at relativistic velocities. It describes the relativistic interaction of the particle's spin with the motion-related magnetic field $\boldsymbol{B}'$, which leads to a modification of the particle's eigenenergies described by [39]

$$\mathcal{H}_{\mathrm{SO}} = \frac{g\mu_{\mathrm{B}}}{2}\boldsymbol{B}' \cdot \boldsymbol{S}' = -\frac{g\mu_{\mathrm{B}}}{2}\frac{1}{c^2}\left(\boldsymbol{v} \times \boldsymbol{E}\right) \cdot \boldsymbol{S}\ . \tag{12}$$

Here, g is the g-factor, μ_{B} the Bohr magneton, c the speed of light, $\boldsymbol{S}$ the spin operator, and primed variables indicate quantities in the rest frame of the particle, whereas variables without prime correspond to the lab frame. Due to the relativistic movement of the particle at velocity $\boldsymbol{v}$, in its rest frame, it senses a magnetic field $\boldsymbol{B}'$ oriented normal to its direction of motion and the electric field $\boldsymbol{E}$ resulting from the electrostatic potential [39].

In solid-state systems, SOC of electrons moving inside the periodic potential of the positively charged nuclei can therefore induce a splitting of otherwise spin-degenerate energy bands. Prominent examples of the consequences of such spin-orbit interaction are the spin-orbit split-off band in all diamond or zinc-blende semiconductors, as well as the Dresselhaus and Bychkov-Rashba effects [39]. The Dresselhaus effect describes the spin splitting of bands in non-centrosymmetric bulk crystals lacking inversion symmetry [40]. Here, the intrinsic asymmetry in the lattice potential, also called bulk inversion asymmetry (BIA), leads to a momentum-dependent splitting of the energy bands into spin-aligned and anti-aligned subbands. The Bychkov-Rashba effect describes a similar band splitting, but in contrast, here the asymmetric potential that couples with the electron spin arises due to the structure inversion asymmetry (SIA) [41–43]. In two-dimensional epitaxially grown heterostructures, the charge carriers can, e.g., be trapped in a confinement potential without spatial

inversion symmetry, which gives rise to a net electric field in growth direction causing the Bychkov-Rashba type spin splitting. Due to this correlation with the specific structure design, in this case, one speaks of structure inversion asymmetry. It is worth noting that the strength of SIA can also be modified by applying an external electric field via a gate electrode [39]. Besides two-dimensional heterostructures or surface states, the Rashba effect can also appear in three-dimensional uniaxial crystals, such as wurtzite type ones [41].

Due to the influence of the nuclear charge on the electric potential and the resulting field, SOI is larger in heavier atoms and, therefore, typically becomes more important in materials composed of heavier atoms [13]. Mercury telluride is a prominent example for such a material where strong spin-orbit coupling due to the heavy mercury atoms lays the foundation for topologically non-trivial behavior. As we will see in the next chapter, two- and three-dimensional topological insulators with variable band gap energies can be realized by alloys and heterostructures made of mercury telluride and cadmium telluride.

2.2 Mercury cadmium telluride based materials

Mercury telluride and cadmium telluride are both part of the II-VI group of semiconductor compound materials. Both materials have a zinc-blende lattice structure and exhibit a tetrahedral crystal symmetry as part of the T_d point group [7]. An important consequence that comes with this crystal structure is the absence of a center of inversion [6]. Their similar lattice constants of 6.48 Å (CdTe) and 6.45 Å (HgTe) allow to build alloys with variable material compositions and make them suitable for the design of nanoscale structures, such as quantum wells or quantum dots [44]. Despite the similarities mentioned above, HgTe and CdTe differ in the sequence of the fundamental band edges [7].

The conduction and valence band in HgTe are formed, respectively, by $5p$ electrons from the tellurium atoms and $6s$ electrons from the mercury atoms, whereas in CdTe they are comprised of the $5s$ electrons from the cadmium as well as the $5p$ electrons of the tellurium atoms [6, 11]. For the calculation of the respective band structures in these two materials, the consideration of relativistic corrections like the Darwin-Term, mass-velocity correction, and the spin-orbit interaction is essential. If relativistic effects are ignored, the gap energy E_in between the valence and conduction band is similar in both materials [6]. However, when the relativistic corrections are taken into account,

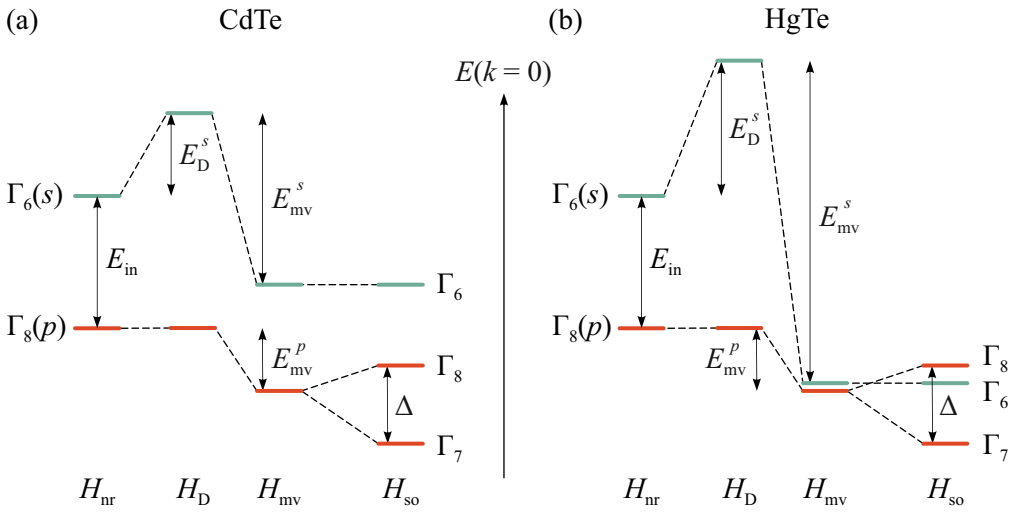

Figure 3: Evolution of the energies of the s-like Γ_6 and p-like Γ_8 bands for $\boldsymbol{k} = 0$ in CdTe (a) and HgTe (b). Starting with the initial non-relativistic Hamiltonian H_{nr}, the relativistic corrections for the Darwin term H_{D}, the mass-velocity H_{mv}, and the spin-orbit interaction H_{so} are included from left to right. A strong energy shift E^s_{mv} due to the mass-velocity correction in HgTe leads to the inversion of the Γ_6 and Γ_8 bands after the spin-orbit interaction-induced splitting of the Γ_8 bands. Picture after Ref. [6].

the energies of the resulting s-type Γ_6 and the p-type Γ_8 bands deviate strongly in the two materials, as shown in Fig. 3. In HgTe, the mass-velocity correction leads to a drastic lowering of the Γ_6 band due to the big mass of mercury. As a result of the additional spin-orbit interaction-induced splitting of the three times degenerate Γ_8 band (when neglecting degeneracy due to spin) into the double-degenerate Γ_8 and the Γ_7 bands, the Γ_8 bands shift above the Γ_6 band in pure HgTe [6]. This results in the inverted band structure of HgTe, where the Γ_8 bands are situated energetically higher than the Γ_6 band [7], see Fig. 4 (b). Therefore, at the interfaces of HgTe to materials without band inversion, topologically protected boundary states form as a result of the transition from inverted to non-inverted band dispersion. In CdTe the situation is different. Due to a much weaker influence of the mass-velocity correction (see Fig. 3 (a)), the bands have a trivial ordering with a band gap of around 1.6 eV at the Γ point between the Γ_6 conduction and the Γ_8 valence bands consisting of a heavy and light hole band, see Fig. 4 (a) [46]. The Fermi energy typically lies inside the band gap, which results in CdTe being an ordinary narrow-gap semiconductor.

In HgTe, however, the Fermi level is situated between the double-degenerate Γ_8 bands, see Fig. 4 (b). Therefore, no energy gap is present in the system, which makes HgTe effectively a zero-gap semiconductor. However, the absence of an

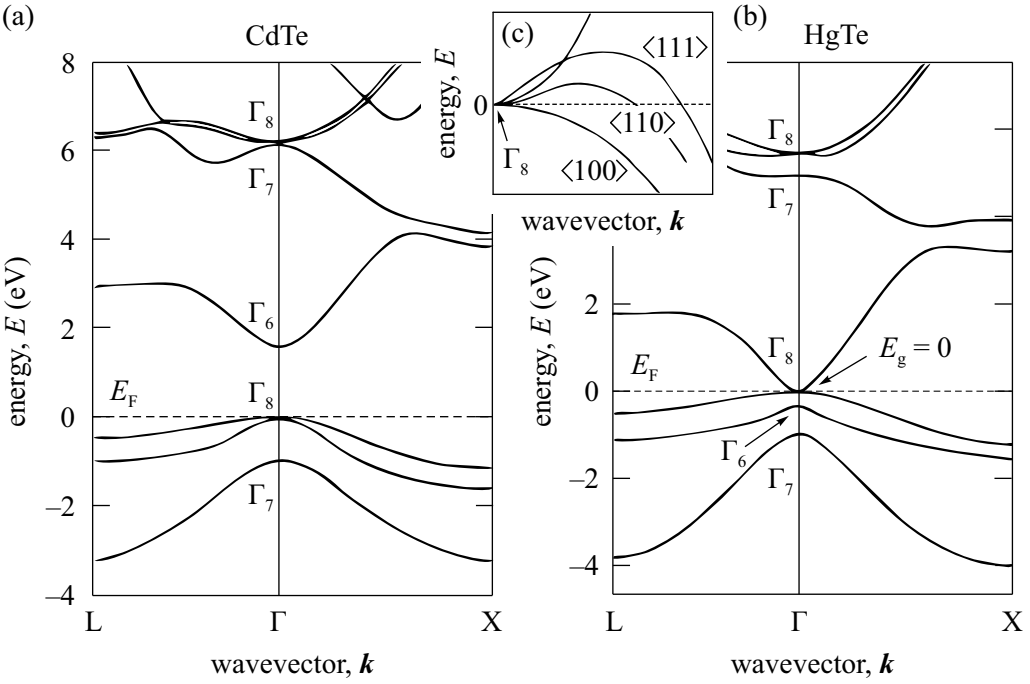

Figure 4: Calculated band spectrum of CdTe (a) and HgTe (b) around the Γ point using an empirical pseudopotential method. Dashed lines at $E = 0$ indicate the position of the Fermi level in the material. Panel (a) shows the trivial band ordering in CdTe. Panel (b): In HgTe, the Γ_8 bands are shifted above the Γ_6 band and the Fermi level intersects the Γ_8 bands. Panel (c) illustrates the conduction and valence bands in HgTe for different crystallographic directions. In directions away from $\langle 100 \rangle$, the valence band maximum shifts away from $\boldsymbol{k} = 0$ to slightly higher energies making HgTe a topological semimetal. Pictures (a) and (b) adapted from Ref. [44]. Picture (c) according to Refs. [6] and [45].

inversion center in the zinc-blende structure gives rise to linear terms in $E(\boldsymbol{k})$. In HgTe, these corrections, despite being negligible for the Γ_6 band, result in a shift of the Γ_8 valence band maximum away from $\boldsymbol{k} = 0$, as shown for certain crystallographic directions in Fig. 4 (c) [6]. This slight displacement of the band maximum away from the Γ point leads to a small overlap of conduction and valence bands effectively rendering HgTe a topological semimetal [7, 44]. The maximum overlap is found along the $\langle 111 \rangle$ direction, whereas the effect vanishes along the $\langle 100 \rangle$ direction [6]. Another important consequence of the inverted band ordering in HgTe is the unusual temperature dependence of the gap energy E_g [6]. Contrary to ordinary semiconductors, where the gap energy decreases with temperature (i.e. $\partial E_g / \partial T < 0$) due to the thermal expansion of the crystal and the interaction of carriers with phonons (for example in CdTe, as shown in the curve for $x = 1$ in Fig. 7 (a)), in HgTe, the gap energy was shown to increase with temperature (i.e. $\partial E_g / \partial T > 0$), as illustrated in

Fig. 7 (a). Note that in both HgTe and CdTe, spin-orbit interaction induces a split-off Γ_7 valence band [6].

To realize a topologically insulating state in HgTe, the Γ_8 degeneracy has to be lifted by opening a band gap between the conduction and valence bands while, at the same time, maintaining the inverted band ordering in the material. This can be done, for example, by introducing uniaxial tensile strain in a thin layer of HgTe by growing it onto CdTe which exhibits a slightly larger lattice constant [7, 18, 19, 47, 48]. This anisotropic deformation disturbs the symmetry of the crystal structure and, in this way, lifts the band degeneracy at the Γ_8 point [6]. Moreover, the Γ_8 degeneracy can also be lifted by quantum confinement in HgTe-based heterostructures [14, 49].

The most prominent example for such a structure is the HgTe quantum well, where a thin layer of HgTe with thickness d is sandwiched between two CdTe or $Cd_xHg_{1-x}Te$ barriers building a type III quantum well [10]. Here, the six relevant bands ($|\Gamma_6, \frac{1}{2}\rangle$, $|\Gamma_6, -\frac{1}{2}\rangle$, $|\Gamma_8, \frac{3}{2}\rangle$, $|\Gamma_8, \frac{1}{2}\rangle$, $|\Gamma_8, -\frac{1}{2}\rangle$, $|\Gamma_8, -\frac{3}{2}\rangle$) combine to form three spin-degenerate quantum well subbands E1, HH1 and LH1. At the Γ point, the $|\mathrm{E1}, m_J\rangle$ subband state is composed of a linear combination of the $|\Gamma_6, m_J = \pm\frac{1}{2}\rangle$ and $|\Gamma_8, m_J = \pm\frac{1}{2}\rangle$ states, whereas the $|\mathrm{HH1}, m_J\rangle$ quantum well state is formed from the $|\Gamma_8, m_J = \pm\frac{3}{2}\rangle$ states [10]. The LH1 subband is energetically split off the other two bands [10]. Away from $\boldsymbol{k} = 0$, where m_J is no longer a good quantum number, the E1 and HH1 states can mix [10].

Due to the influence of the trivial band ordering in the barrier material CdTe, where the Γ_6 band energetically exceeds the Γ_8 bands, the dispersion of the QW states depends on the thickness d of the HgTe layer [10], as illustrated in Fig. 5 (a). For thin HgTe films with $d < d_\mathrm{c}$, the influence of the CdTe barrier prevails and the E1 band is located above the HH1 states (shown in Fig. 5 (b)), resulting in an ordinary band ordering resembling the one in CdTe [10, 11]. However, if the QW width exceeds a certain threshold d_c, the influence of the HgTe dispersion dominates and the HH1 band shifts above the E1 band (depicted in Fig. 5 (c)), resulting in an inverted band ordering [10]. Since these two dispersion types are characterized by a different $\mathbb{Z}_2$ topological order and cannot be transformed into one another with only smooth deformations of the corresponding Hamiltonian, there has to be an inevitable crossing of the E1 and HH1 bands at the threshold width d_c [10], as highlighted in Fig. 5 (a). Such quantum wells with $d = d_\mathrm{c}$ are characterized by an almost linear dispersion without an energy gap and described by the theory of massless Dirac fermions

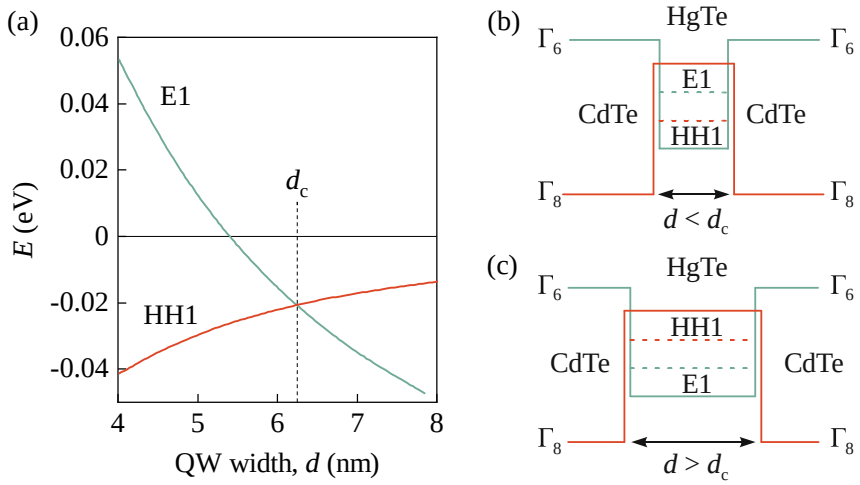

Figure 5: Panel (a): Calculations of the energies of the E1 (turquoise) and HH1 (orange) bands with respect to the quantum well thickness d at $k_{\|} = 0$. Here $k_{\|}$ denotes the k-vector in the QW plane. At $d_c \approx 6.3\,\text{nm}$ the two bands cross each other. Panels (b) and (c): Schematic depiction of the energetic positions of the Γ_6, Γ_8, E1, and HH1 bands in a HgTe QW with CdTe barriers for $d < d_c$ (b) and $d > d_c$ (c). Solid lines indicate the energies of the fundamental Γ_6 (turquoise) and Γ_8 (orange) bands in the materials, whereas dashed lines represent the resulting E1 (turquoise) and HH1 (orange) bands in the QW. Pictures according to Ref. [10].

[11]. In literature, this critical threshold thickness is estimated to be around $d_c = 6.3 \pm 0.1\,\text{nm}$ [10, 11, 50]. The exact value of d_c can depend on multiple parameters, such as the interface orientation [50], temperature [51], as well as lattice mismatch-induced strain and, thus, also on the respective composition of the $Cd_xHg_{1-x}Te$ barriers in QW structures where no pure CdTe barriers are used [52].

In the topological non-trivial phase ($d > d_c$), a single pair of gapless helical edge states forms at the interface between the quantum well (inverted band dispersion) and the barrier (trivial band dispersion) as a consequence of their different $\mathbb{Z}_2$ order parameter [10]. These states have an almost linear dispersion, are topologically protected by time-reversal symmetry, and propagate dissipationless along the edges [10, 11]. Due to spin-momentum locking, carriers with opposite spin travel in different directions on opposing edges. In the absence of an external magnetic field, this leads to a spin current along the edges of the QW termed the quantum spin Hall effect [11]. Each spin-resolved edge channel exhibits a distinct quantized conductance of e^2/h characteristic for one-dimensional transport [11]. Note that the states in QWs with critical thickness d_c exhibit no topological protection even though they have a similar band dispersion. Moreover, the topological protection of the edge states in

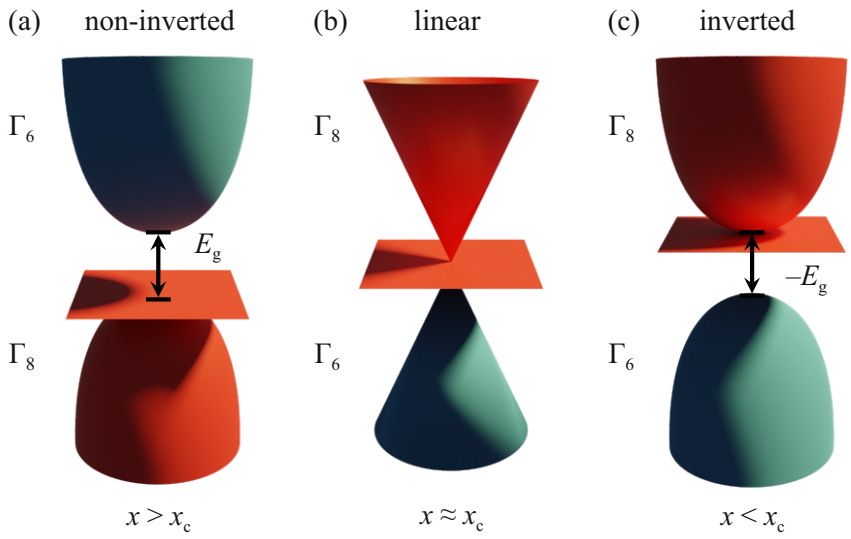

Figure 6: Sketch of the energy dispersion around the Γ point in $Cd_xHg_{1-x}Te$ alloys with different cadmium contents x for a fixed temperature. A turquoise shading of the bands indicates s-like (Γ_6) symmetry, while red coloring marks p-like (Γ_8) bands. Note that in panel (b), the linear bands are in fact a mixture of the Γ_6 and Γ_8 bands. The orange plane between the bands illustrates the flat heavy hole Γ_8 band. Panel (a): For $x > x_c$, the alloy behaves as a typical narrow-gap semiconductor with trivial band ordering and a positive gap energy. Panel (b): At the critical content x_c the gap closes and the material hosts massless Kane fermions. Panel (c): Inverted Γ_8 and Γ_6 bands indicated by a negative gap energy E_g yield topologically non-trivial behavior for $x < x_c$. Picture according to Ref. [9].

QWs with $d > d_c$ can also be removed by breaking time-reversal symmetry, e.g, by applying an external magnetic field. Despite the fact, that topologically protected boundary states were first observed experimentally in HgTe quantum wells, it was predicted long ago that such states also exist in $Cd_xHg_{1-x}Te$ alloys [15, 16].

In such compounds, consisting of HgTe and CdTe with variable composition, the band gap can be tuned over a wide frequency range spanning the entire infrared region [46]. By variation of the cadmium content x, gap energies ranging between around 1.6 eV (for pure CdTe with $x = 1$) and -0.3 eV (for pure HgTe with $x = 0$) can be realized. Note that negative gap energies indicate an inverted ordering of the Γ_8 and Γ_6 bands, whereas positive values correspond to a trivial band ordering. Consequently, $Cd_xHg_{1-x}Te$ is one of the leading materials for photovoltaic detectors in this frequency range [46]. The more mercury in the alloy (i.e. the lower x), the stronger the influence of the heavy atoms on the relativistic mass-velocity and spin-orbit correction. A consecutive lowering of the cadmium content, therefore, has to lead to a phase transition from a topologically trivial to a non-trivial state (similar to

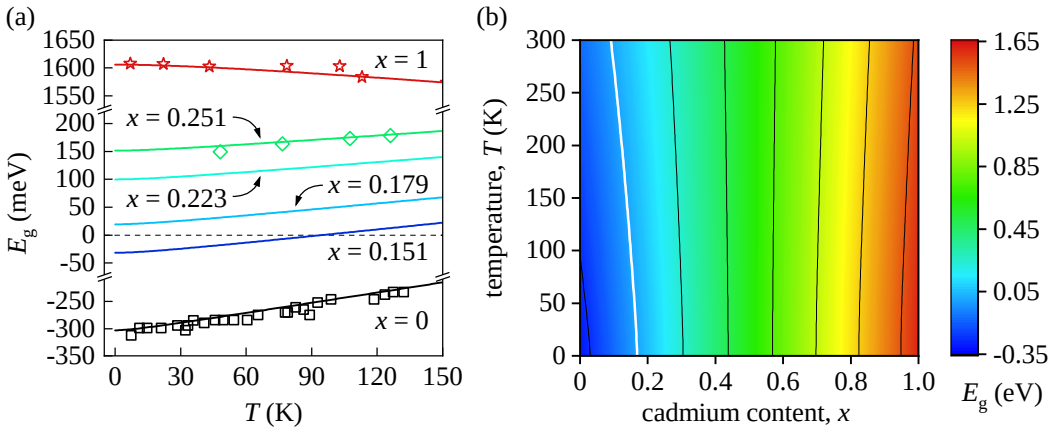

Figure 7: Panel (a): Gap energy E_g in $Cd_xHg_{1-x}Te$ alloys with respect to the temperature T for different cadmium contents x. The curves labeled $x = 1$ and $x = 0$ show the temperature dependence in pure CdTe and HgTe, respectively. Symbols correspond to experimental data collected from different sources: Squares are taken from Ref. [46], stars from Ref. [53], and diamonds were extracted from Ref. [54]. Solid lines are calculations according to Eq. (13). Picture after Ref. [9]. Panel (b): Color plot of the gap energy E_g with respect to cadmium content x and temperature T calculated according to Eq. (13). Solid lines are contour lines at integer multiples of 0.25 eV with the white line indicating the gapless state at $x = x_c$ with $E_g = 0$, as sketched in Fig. 6 (b). In the region to the left of the white line, the band gap is negative, implying inverted band ordering, whereas to the right of the white line, a trivial band ordering is present in the alloy.

the one described above for HgTe quantum wells) at a certain cadmium content (see Fig. 6) since both HgTe and CdTe are characterized by a different $\mathbb{Z}_2$ topological order [8]. This so called critical cadmium content x_c was shown to be dependent on temperature, see Fig. 7 (b) [9]. Figures 6 (a), (b) and (c) sketch the conduction and valence bands for alloys with $x > x_c$, $x \approx x_c$, and $x < x_c$, respectively. Alloys with a critical cadmium content exhibit gapless, approximately linear bands that are intersected by the almost flat heavy hole band at the vertex [8, 9]. In alloys with a Cd content below x_c, the Γ_6 and Γ_8 bands are inverted, rendering the material a three-dimensional topological semimetal with protected surface states at the boundary of the material to trivially insulating materials or vacuum [8]. Note that additional crystallographic strain can open up an energy gap between the Γ_8 bands, similar as in pure HgTe. In this case, the semimetallic character of the $Cd_xHg_{1-x}Te$ alloy changes to a topologically insulating one. If the Cd content is increased beyond x_c, however, the alloy becomes a standard gapped semiconductor and, as a consequence, no topologically protected states are present on the surface.

A topological phase transition can also be induced in alloys with a fixed x

by variation of the temperature [9, 55], see Fig. 7 (a). It was demonstrated that the gap energy can be described empirically as a function of the cadmium content x and temperature T by [46]

$$\begin{aligned} E_{\mathrm{g}}(x,T) = &- 0.303\,(1-x) + 1.606\,x - 0.132\,x\,(1-x) \\ &+ \frac{(6.3\,(1-x) - 3.25\,x - 5.92\,x\,(1-x))\,10^{-4}\,T^2}{11\,(1-x) + 78.7\,x + T}\,[\mathrm{eV}] \end{aligned} \tag{13}$$

within the range $0 \leq x \leq 1$ and $0 \leq T \leq 500$. Figure 7 presents different calculations of the gap energy E_{g} according to Eq. (13) together with experimental data. It is seen that below a certain critical temperature T_{c}, alloys with a sufficiently low cadmium content ($x \lesssim 0.17$) exhibit a negative energy gap corresponding to an inverted band ordering [8, 9]. Alloys with a higher x, however, exhibit positive gap energies in the whole temperature range and, therefore, no such critical temperature exists in this case, see Fig. 7. It is worth mentioning that for a cadmium content of exactly $x = 0.505$, Eq. (13) predicts the gap energy to be independent of temperature [46]. Note that a transition from inverted to non-inverted regime, similar to the temperature- or cadmium content-induced transitions described above, can also be induced by applying hydrostatic pressure to the $\mathrm{Cd}_x\mathrm{Hg}_{1-x}\mathrm{Te}$ alloy [6].

2.3 Radiation-induced optoelectronic effects

Illumination of semiconductors with terahertz radiation can lead to a multitude of photoelectric effects. In most cases, the photon energies in the terahertz range are much smaller than the band gap in conventional semiconductor materials, which prevents direct single-photon excitation of electrons across the energy gap. Thus, the terahertz photoresponse is dominated by redistribution effects of photoexcited carriers in momentum and energy space [56]. As we will discuss in this chapter, such momentum redistribution as a response to uniform terahertz illumination gives rise to a direct electric current in homogeneous materials without any external bias. This phenomenon is termed the photogalvanic effect [57]. Furthermore, terahertz illumination can also alter the conductivity of a material by modifying either the density or the mobility of the charge carriers. In this chapter, an overview over these basic effects is presented, including the phenomenological approach as well as microscopic models.

2.3.1 Photogalvanic effect

The effect of an external electromagnetic field on the electric current density in a material can be phenomenologically described by a series expansion in powers of the electric field strength $\boldsymbol{E}(\omega, \boldsymbol{q})$ inside the medium [56]. For that, the incident radiation field is taken in the form of a planar wave according to

$$\boldsymbol{E}(\boldsymbol{r}, t) = \boldsymbol{E}(\omega, \boldsymbol{q}) e^{i(\boldsymbol{q}\cdot\boldsymbol{r}-\omega t)} + \boldsymbol{E}^*(\omega, \boldsymbol{q}) e^{-i(\boldsymbol{q}\cdot\boldsymbol{r}-\omega t)} \ . \tag{14}$$

Here, $\boldsymbol{q}$ and ω are the photon wavevector and frequency, respectively, and the second term in Eq. (14) is the complex conjugate (denoted by the asterisk) of the first term, which will be abbreviated with *c.c.* in the following. Consequently, the time- and space-dependent current density inside the material up to the second order in $\boldsymbol{E}(\omega, \boldsymbol{q})$ is given by [58]

$$\begin{aligned} j_\alpha(\boldsymbol{r}, t) = &\sum_\beta \left(\sigma^{(1)}_{\alpha\beta} E_\beta(\omega, \boldsymbol{q}) e^{i(\boldsymbol{q}\cdot\boldsymbol{r}-\omega t)} + c.c. \right) \\ &+ \sum_{\beta,\gamma} \left(\sigma^{(2\prime)}_{\alpha\beta\gamma} E_\beta(\omega, \boldsymbol{q}) E_\gamma(\omega, \boldsymbol{q}) e^{2i(\boldsymbol{q}\cdot\boldsymbol{r}-\omega t)} + c.c. \right) \\ &+ \sum_{\beta,\gamma} \left(\sigma^{(2)}_{\alpha\beta\gamma} E_\beta(\omega, \boldsymbol{q}) E^*_\gamma(\omega, \boldsymbol{q}) \right) + \dots \ , \end{aligned} \tag{15}$$

where the indices α, β, and γ take the values of the Cartesian coordinates x, y, and z. Note that effects proportional to the third power of the electric field are omitted in Eq. (15) and are discussed separately in the next chapter. The first term in Eq. (15) represents the linear transport response that averages to zero in case of an alternating terahertz driving field. This term becomes relevant only in case of a dc electric driving field where it is commonly known as Ohm's law with the dc conductivity $\sigma^{(1)}_{\alpha\beta}(\omega = 0)$. The second term, which oscillates in time with a frequency of 2ω, characterizes the phenomenon of second harmonic generation that, as an effect in the second order of the electric field, occurs only in crystals without inversion symmetry [59].

In contrast to the first two current density contributions which both oscillate in time, the third term of Eq. (15) is independent of t and, consequently, describes the generation of a direct current as response to the homogeneous radiation field. The corresponding second-order conductivity $\sigma^{(2)}_{\alpha\beta\gamma}$ can be partitioned

into a photon wavevector-independent and dependent part according to [58]

$$\begin{aligned}\sigma^{(2)}_{\alpha\beta\gamma}(\omega,\boldsymbol{q}) &= \sigma^{(2)}_{\alpha\beta\gamma}(\omega,\boldsymbol{q}=0) + \sigma^{(2)}_{\alpha\beta\gamma}(\omega,\boldsymbol{q}\neq 0) \\ &\simeq \chi_{\alpha\beta\gamma}(\omega) + T_{\alpha\delta\beta\gamma}(\omega) q_\delta \ .\end{aligned} \tag{16}$$

In the last step, only the contributions linear in $\boldsymbol{q}$ were considered for the wavevector-dependent part characterized by the fourth-rank tensor $T_{\alpha\delta\beta\gamma}$. This procedure allows to distinguish two different contributions in the direct current density response to the external radiation field [56]

$$\begin{aligned}j_\alpha(\boldsymbol{r}) &= \sum_{\beta,\gamma} \sigma^{(2)}_{\alpha\beta\gamma}(\omega,\boldsymbol{q}) E_\beta E^*_\gamma \\ &\simeq \underbrace{\sum_{\beta,\gamma} \chi_{\alpha\beta\gamma}(\omega) E_\beta E^*_\gamma}_{\text{photogalvanic effect}} + \underbrace{\sum_{\delta,\beta,\gamma} T_{\alpha\delta\beta\gamma}(\omega) q_\delta E_\beta E^*_\gamma}_{\text{photon drag effect}} \ .\end{aligned} \tag{17}$$

The first term proportional to the third-rank tensor $\chi_{\alpha\beta\gamma}(\omega)$ and independent of the photon wavevector describes the photogalvanic effect, which can only occur in non-centrosymmetric crystals due to symmetry arguments [57, 58]. The second term proportional to the photon wavevector and the fourth-rank tensor $T_{\alpha\delta\beta\gamma}(\omega)$ represents the photon drag effect, which considers a transfer of the photon momentum to the electrons in the material. In contrast, this effect is also allowed in centrosymmetric crystals because of the fact that due to the linear proportionality to the photon wavevector, a spatial inversion also leads to a change of sign of $T_{\alpha\delta\beta\gamma}(\omega) q_\delta$ [58].

Both effects can be further examined in terms of their polarization dependence. For that, the product $E_\beta E^*_\gamma$ is mathematically decomposed into a sum of the real part $\left\{E_\beta E^*_\gamma\right\} = \frac{1}{2}\left(E_\beta E^*_\gamma + E_\gamma E^*_\beta\right)$, which is symmetrical with respect to the permutation of the indices β and γ, and the antisymmetrical, purely imaginary part $\left[E_\beta E^*_\gamma\right] = \frac{1}{2}\left(E_\beta E^*_\gamma - E_\gamma E^*_\beta\right)$ according to [56]

$$E_\beta E^*_\gamma = \left\{E_\beta E^*_\gamma\right\} + \left[E_\beta E^*_\gamma\right] \ . \tag{18}$$

While a similar analysis can also be carried out for the photon drag effect, in the following the treatment will be exemplarily demonstrated for the photogalvanic effect. Because of the contraction of the tensor $\chi_{\alpha\beta\gamma}$ with $E_\beta E^*_\gamma$ in the photogalvanic effect (see Eq. (17)), the symmetries of the real and imaginary parts of $E_\beta E^*_\gamma$ also reflect in $\chi_{\alpha\beta\gamma}$. Thus, the real part of $\chi_{\alpha\beta\gamma}$ is symmet-

ric in the indices $\beta\gamma$, while the imaginary part is antisymmetric in $\beta\gamma$ [57]. The antisymmetric, imaginary part can be reduced to the real, second-rank pseudotensor $\xi_{\alpha\nu}$ with the help of the antisymmetric Levi-Civita permutation tensor $\epsilon_{\nu\beta\gamma}$ according to [56]

$$\begin{aligned}\sum_{\beta,\gamma}\chi_{\alpha\beta\gamma}\left[E_\beta E_\gamma^*\right] =& i\cdot\sum_{\nu,\beta,\gamma}\xi_{\alpha\nu}\epsilon_{\nu\beta\gamma}\left[E_\beta E_\gamma^*\right]=\sum_{\nu}\xi_{\alpha\nu}i\left(\boldsymbol{E}\times\boldsymbol{E}^*\right)_\nu \\ =&\sum_{\nu}\xi_{\alpha\nu}\hat{e}_\nu P_{\mathrm{circ}}E^2\ .\end{aligned} \tag{19}$$

Introducing the cross product in Eq. (19) highlights that this contribution to the photogalvanic effect is proportional to the degree of circular polarization $P_{\mathrm{circ}}\in[-1,1]$ of the radiation incident along the direction of the unit vector $\hat{\boldsymbol{e}}=\boldsymbol{q}/q$. Hence, this term describes the current density resulting from the circular photogalvanic effect (CPGE), which occurs only in gyrotropic media as a result of illumination with circularly polarized radiation [56]. The total photogalvanic current density is then given by

$$j_\alpha = \underbrace{\sum_{\beta,\gamma}\chi_{\alpha\beta\gamma}\left\{E_\beta E_\gamma^*\right\}}_{\text{linear photogalvanic effect}} + \underbrace{\sum_{\nu}\xi_{\alpha\nu}i\left(\boldsymbol{E}\times\boldsymbol{E}^*\right)_\nu}_{\text{circular photogalvanic effect}}\ . \tag{20}$$

Here, the first term proportional to $\chi_{\alpha\beta\gamma}=\chi_{\alpha\gamma\beta}$ accounts for the linear photogalvanic effect (LPGE) which is excited by linearly polarized radiation in non-centrosymmetric crystals, whereas the second term represents the CPGE. The phenomenological approach presented above allows to conveniently deduce key properties of radiation-induced currents, such as their dependence on polarization or angle of incidence, from the symmetry group of the studied materials [58]. However, it is important to note that the underlying microscopic origin of current generation is of great significance for understanding the exact characteristics of the photogalvanic currents. In the following, two microscopic mechanisms for the photogalvanic effect are described exemplarily. For a detailed description of the multitude of photogalvanic mechanisms please refer to, e.g., Refs. [57], [56] or [58].

In many cases, photogalvanic currents caused by homogeneous illumination arise because of an asymmetry in the relaxation rates of photoexcited free carriers. When considering the scattering rate $W_{\boldsymbol{p},\boldsymbol{p}'}$, which describes the probability that a carrier with initial momentum $\boldsymbol{p}$ adopts the momentum $\boldsymbol{p}'$ after an elastic scattering event, time-reversal symmetry and spatial sym-

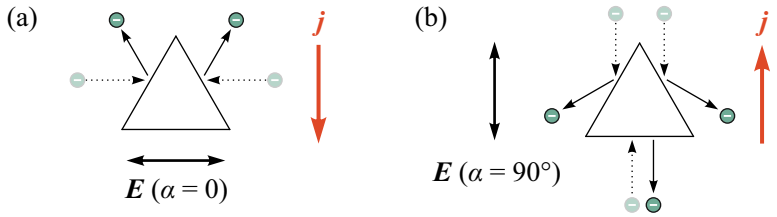

Figure 8: Sketch of the microscopic mechanism of the LPGE in structures with C_{3v} symmetry as a result of asymmetric elastic scattering. Electrons (indicated by lightly transparent and solid cyan circles before and after scattering, respectively) in the system are accelerated along the oscillating electric field $\boldsymbol{E}$ and scatter on equally oriented, equilateral triangles which represent the symmetry of this point group. Panels (a) and (b) illustrate this process for two perpendicular orientations of the radiation field. Due to the shape of the triangles, the preferred scattering direction of the electrons is different for the two polarization angles α, resulting in an opposite direction of the generated photocurrents depicted by the red arrows. Adapted from Refs. [56, 57, 60].

metry usually ensure that $W_{\boldsymbol{p},\boldsymbol{p}'} = W_{-\boldsymbol{p}',-\boldsymbol{p}}$ (called the reciprocity theorem) and $W_{\boldsymbol{p},\boldsymbol{p}'} = W_{-\boldsymbol{p},-\boldsymbol{p}'}$, respectively [57]. In systems where one of these two symmetries is broken, the principle of detailed balance $W_{\boldsymbol{p},\boldsymbol{p}'} = W_{\boldsymbol{p}',\boldsymbol{p}}$ [57] is no longer valid, resulting in asymmetric scattering [56]. For instance, in non-centrosymmetric structures, spatial inversion symmetry is broken, i.e. $W_{\boldsymbol{p},\boldsymbol{p}'} \neq W_{-\boldsymbol{p},-\boldsymbol{p}'}$, which leads to a violation of the principle of detailed balance, i.e. $W_{\boldsymbol{p},\boldsymbol{p}'} \neq W_{\boldsymbol{p}',\boldsymbol{p}}$. Furthermore, also the breaking of time-reversal symmetry due to, e.g., an external magnetic field can lead to an asymmetric relaxation rate, even in centrosymmetric systems [56].

One of the simplest examples that allows an easy graphical demonstration of the underlying microscopic mechanism of the LPGE are triangular structures exhibiting a C_{3v} symmetry [60, 61]. This symmetry group includes structures with a three-fold rotational symmetry, three mirror planes, and no inversion center. In such systems, the lack of spatial inversion symmetry causes an asymmetry in the relaxation rate that results in directed photogalvanic currents when incident linearly polarized, homogeneous, terahertz radiation is absorbed by free carriers [56]. The microscopic current generation process can be illustrated by considering elastic scattering on equally oriented, equilateral triangles, as sketched in Fig. 8. Illumination with a linearly polarized, alternating electric field $\boldsymbol{E}$ leads to an optical alignment of the momenta of carriers which are accelerated along the direction of $\boldsymbol{E}$. Due to the oscillatory nature of the excitation, this alone does not lead to a directed photocurrent. However, when the excited, momentum-aligned carriers relax because of elastic scattering on the triangle structures, the preferred scattering direction strongly

depends on the orientation of the wedge structures with respect to the electric field, causing an asymmetric scattering probability [56]. For an electric field oriented parallel to one of the triangle's sides, as illustrated in Fig. 8 (a), carriers are predominantly scattered perpendicular to the direction of the driving field, resulting in a net photogalvanic current normal to the applied electric field. In contrast, a rotation of the electric field by 90°, as shown in Fig. 8 (b), results in a change of the preferred scattering direction that leads to a sign inversion of the resulting current [57]. This behavior gives rise to a polarization dependence of the observed LPGE characteristic for the respective symmetry group of a material. Note that this model can also be extended to include inelastic scattering [57].

Photocurrents resulting from asymmetric photoexcitation and energy relaxation of free carriers have also been observed in three-dimensional topological insulators on the basis of strained HgTe films [18, 19]. Strong magnetic field-induced resonances were observed in the photocurrents, which were shown to originate from the surface states of the film. The applied magnetic field modifies the electron scattering rate according to

$$W_{\boldsymbol{p},\boldsymbol{p}'} = W^{(0)}_{\boldsymbol{p},\boldsymbol{p}'} + W^{(1)}_{\boldsymbol{p},\boldsymbol{p}'} B \ , \tag{21}$$

where $W^{(0)}_{\boldsymbol{p},\boldsymbol{p}'}$ describes the scattering rate at zero field and $W^{(1)}_{\boldsymbol{p},\boldsymbol{p}'}$ represents an asymmetric correction that results from the mixing of electronic states due to the magnetic field [62]. This magnetic field-induced asymmetry in the scattering rate, in turn, leads to the generation of a directed current as a result of scattering of photoexcited electrons on phonons or static defects. The corresponding distribution $f_{\boldsymbol{p}}$ of the surface state electrons can be deduced from the Boltzmann equation [18]

$$e\left(\boldsymbol{v} \times \boldsymbol{B}\right) \cdot \frac{\partial f_{\boldsymbol{p}}}{\partial \boldsymbol{p}} = g_{\boldsymbol{p}} - \frac{f_{\boldsymbol{p}} - \langle f_{\boldsymbol{p}} \rangle_{\boldsymbol{p}}}{\tau} \ , \tag{22}$$

where the momentum and velocity of the electrons are given by $\boldsymbol{p}$ and $\boldsymbol{v}$, respectively, $g_{\boldsymbol{p}}$ denotes the generation rate of electrons with momentum $\boldsymbol{p}$, τ designates the momentum relaxation time, and $\langle f_{\boldsymbol{p}} \rangle_{\boldsymbol{p}}$ implies the average of the distribution function over all momentum directions. This equation can be rewritten in terms of the photocurrent density $\boldsymbol{j} = \sum_{\boldsymbol{p}} e\boldsymbol{v} f_{\boldsymbol{p}}$ by multiplication

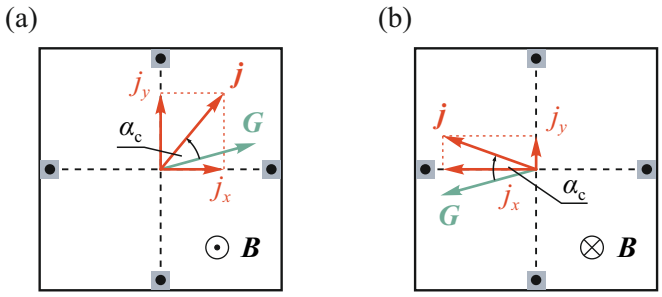

Figure 9: Illustration of the generated photocurrents (depicted as red arrows) with respect to the direction of the generation vector $\boldsymbol{G}$ (indicated by the turquoise arrow) for two antiparallel orientations of the external magnetic field $\boldsymbol{B}$, shown in panels (a) and (b). For the depicted orientation of $\boldsymbol{G}$, the x-component of the photogalvanic current $\boldsymbol{j}$ behaves antisymmetrically in magnetic field, i.e., inverts its sign when the direction of $\boldsymbol{B}$ is inverted, whereas j_y is symmetric in $\boldsymbol{B}$. Note that the direction of $\boldsymbol{j}$ systematically deviates from $\boldsymbol{G}$ by the Hall angle $\alpha_c = \arctan(\omega_c \tau)$ due to the Lorentz force. Adapted from Ref. [18].

with $e\boldsymbol{v}$ and summation over all momenta $\boldsymbol{p}$ according to [18]

$$-\boldsymbol{j} \times \boldsymbol{\omega}_c = \boldsymbol{G} - \frac{\boldsymbol{j}}{\tau} \,. \tag{23}$$

Here, $\boldsymbol{\omega}_c = \omega_c \hat{\boldsymbol{z}}$ is a vector pointing in z-direction whose absolute value corresponds to the cyclotron frequency $\omega_c = eB_z/m^*$ and $\boldsymbol{G} = \sum_{\boldsymbol{p}} e\boldsymbol{v} g_{\boldsymbol{p}}$ denotes the rate of current generation. Certainly, the direction and magnitude of the current generation vector $\boldsymbol{G}$ depend on the asymmetry in the rate of surface electron scattering as well as on the absorbed radiation intensity [18]. As already demonstrated in the example of elastic scattering in the C_{3v} point group, the scattering asymmetry strongly depends on the symmetry of the system. Consequently, the direction of $\boldsymbol{G}$ is also affected by the symmetry of the material. Since (013)-grown HgTe structures are part of the C_1 point group, they possess no non-trivial symmetry operation. Thus, in such systems, the scattering asymmetry is not bound to certain crystallographic axes and the magnetic field-assisted photocurrent generation rate is given in the general form [18]

$$\boldsymbol{G} = \boldsymbol{\gamma} I \eta(\omega) B_z \,, \tag{24}$$

with the radiation intensity I, the absorbance $\eta(\omega)$ of the material, and the vector $\boldsymbol{\gamma}$ whose direction is defined by the magnetic field-induced asymmetry of electron scattering. Solving Eq. (23), the photogalvanic current density from the surface states of three-dimensional (013)-oriented HgTe films is given for

two perpendicular in-plane directions by [18]

$$\begin{aligned} j_x =& \frac{\gamma_x + \omega_c \tau \gamma_y}{1 + \omega_c^2 \tau^2} I \eta(\omega) B_z \\ j_y =& \frac{\gamma_y - \omega_c \tau \gamma_x}{1 + \omega_c^2 \tau^2} I \eta(\omega) B_z \ . \end{aligned} \tag{25}$$

Due to the lack of symmetry operations in the C_1 point group, $\boldsymbol{G} \propto \boldsymbol{\gamma}$ is not constrained to certain crystallographic axes and may depend on multiple parameters, such as temperature, radiation frequency, or applied static electric fields. Figure 9 illustrates that this behavior of the photocurrent generation vector may result in photocurrents which can be even or odd in magnetic field depending on the exact orientation of $\boldsymbol{G}$. In the example sketched in Fig. 9, the respective orientation of $\boldsymbol{G}$ results in a photocurrent whose projections j_x and j_y on the coordinate axes behave odd and even in magnetic field, respectively. Note that the direction of the total photocurrent density $\boldsymbol{j}$ systematically deviates from the direction of $\boldsymbol{G}$ due to the Lorentz force which acts on moving carriers [57].

2.3.2 Photoconductivity

Besides the photogalvanic effect, illumination with terahertz radiation can also lead to a change of the material conductivity, i.e. photoconductivity. This effect is proportional to the third order of the electric field according to [58]

$$j_\alpha(\boldsymbol{r}, t) = \sum_{\beta\gamma\delta} = \sigma^{(3'')}_{\alpha\beta\gamma\delta} E_\beta(\omega, \boldsymbol{q}) E^*_\gamma(\omega, \boldsymbol{q}) E^{(\mathrm{dc})}_\delta(0, 0) \ . \tag{26}$$

Here, the fourth-rank conductivity tensor $\sigma^{(3'')}_{\alpha\beta\gamma\delta}$ describes the interaction between the incident radiation field $\boldsymbol{E}(\omega, \boldsymbol{q})$ and the static electric field $E^{(\mathrm{dc})}_\delta(0, 0)$ caused by the applied bias voltage. Note that $\sigma^{(3'')}_{\alpha\beta\gamma\delta}$ can be separated into symmetric and antisymmetric parts analogously to Eqs. (19) and (20) to distinguish between the linear and circular photoconductivity [58]. As Eq. (26) points out, the photoconductive response is proportional to both the amplitude of the bias field $E^{(\mathrm{dc})}_\delta(0, 0)$ and the intensity $I \propto |\boldsymbol{E}(\omega, \boldsymbol{q})|^2$ of the radiation electric field. In the Drude formalism, the static conductivity without any external fields is given by $\sigma_0 = qn\mu$, with the charge q, density n, and mobility μ of the charge carriers in the system [63, 64]. From this relation it becomes clear that in a material with either electrons or holes with $|q| = e$, one way

to achieve photoconductivity is by a radiation-induced variation of the charge carrier density. Such a change is typically caused by interband transitions in narrow-gap semiconductors that generate electron-hole pairs [63], or by photoionization of deep and shallow impurities, which generates only one specific kind of carriers [56]. Furthermore, the conductivity can also change due to a modification of the carrier mobility. This process is called μ-photoconductivity or electron bolometric photoconductivity and results from Drude absorption of radiation which leads to a heating of the charge carriers that, in turn, modifies their energy distribution and, consequently, also their mobility. This effect becomes especially important if the free-carrier concentration in the material is sufficiently high and the radiation energies are smaller than the band gap of the material, which effectively prevents photoexcitation across the band gap [56]. Strong electron gas heating manifests for a high free-carrier concentration which causes the electron-electron scattering time τ_{ee}, defined as the average time between two consecutive collisions of an electron with other electrons, to be much shorter than the energy relaxation time τ_{ε}. The latter one is a measure of how fast electrons and lattice exchange energy, i.e. how fast electron temperature T_{e} and lattice temperature T_{l} thermalize, e.g. due to inelastic electron-phonon scattering. Under conditions where $\tau_{\mathrm{ee}} \ll \tau_{\varepsilon}$, dominant electron-electron collisions cause a strong energy thermalization between the electrons themselves, which establishes an average electron temperature T_{e} that significantly differs from the lattice temperature T_{l} [56]. The magnitude of T_{e} is defined by the interplay of radiation absorption by the electron subsystem and the energy transfer to the lattice. This is expressed in the balance equation for bulk materials [56]

$$\frac{K(\omega) I \varepsilon_{\mathrm{eff}}}{\hbar\omega} = \langle Q(T_{\mathrm{e}}) \rangle \, n \ . \tag{27}$$

Here, $K(\omega)$ denotes the absorption coefficient that is linearly proportional to the free-carrier concentration n, $\varepsilon_{\mathrm{eff}}$ is the effective energy which is transferred from one photoexcited electron to the electron subsystem via electron-electron collisions, and $\langle Q \rangle = \langle \mathrm{d}\varepsilon/\mathrm{d}t \rangle$ describes the average energy loss per unit time for a single electron. In case of weak heating, μ-photoconductivity can be well approximated by [56]

$$\frac{\Delta\sigma}{\sigma_0} = \frac{1}{\mu} \left. \frac{\partial \mu}{\partial T_{\mathrm{e}}} \right|_{T_{\mathrm{e}}=T_{\mathrm{l}}} \Delta T_{\mathrm{e}} \ , \tag{28}$$

where ΔT_e is the photo-induced change in the electron temperature T_e. It is immediately seen that the sign of the bolometric, photoconductive signal is defined by the derivative $\partial\mu/\partial T_\mathrm{e}$. If the mobility of the electrons increases with rising temperature (i.e. $\partial\mu/\partial T_\mathrm{e} > 1$), one speaks of positive photoconductivity. Such a behavior occurs for example under conditions where charged impurity scattering is the dominant mechanism in the electron momentum loss rate. In contrast, negative photoconductivity caused by a decline of the mobility with temperature (i.e. $\partial\mu/\partial T_\mathrm{e} < 1$) is known to occur in the case of predominant electron-phonon scattering [56, 63]. Electron bolometric photoconductivity is governed by very fast temporal kinetics based on the free-carrier energy relaxation time τ_ε which commonly is in the sub-ps to ns range depending on the particular temperature, material, as well as carrier density [56]. For typical terahertz pulse durations of around 100 ns $> \tau_\varepsilon$ used for investigations of the photoconductivity kinetics in this work, μ-photoconductive signals thus mimic the temporal evolution of the excitation pulse. This effectively allows to distinguish μ-photoconductivity from other photoconductive mechanisms with longer temporal kinetics, such as ionization of impurities or lattice heating. The latter one, for example, can be induced by highly intense radiation pulses but, in contrast, exhibits much slower kinetics determined by the slow cooling of the sample as a whole. This results in a much longer decline time of the corresponding photoconductive signal up to microseconds or longer [56]. It is important to note that despite of the huge radiation intensities of the laser pulses used in parts of this work, their corresponding energy is fairly small. For this reason, lattice heating does not constitute a dominant contribution to the photoconductive signals under the experimental conditions of this work and can be neglected.

In general, the magnitude of both photogalvanic effect and photoconductivity depends on the absorbed radiation power, see e.g. Eqs. (20) and (26). Thus, they are strongly enhanced under conditions of cyclotron resonance where, as we will discuss in the next chapter, resonant absorption of the incident radiation takes place. Hence, measurements of photogalvanic currents, photoconductivity as well as radiation transmission are excellent tools to investigate the cyclotron resonance in materials, as demonstrated, e.g., in Refs. [18–21].

2.4 Cyclotron resonance

The phenomenon of cyclotron resonance (CR) can be described either in a quasiclassical or in a quantum mechanical picture. The full, quantum mechanical description becomes necessary for quantizing magnetic fields including the regime of Shubnikov-de Haas oscillations and the quantum Hall regime. Let us begin with the more basic and physically transparent, classical Drude-Boltzmann description. Particles with charge q moving with velocity $\boldsymbol{v}$ in a magnetic field $\boldsymbol{B}$ are subjected to the Lorentz force $\boldsymbol{F} = q\,(\boldsymbol{v} \times \boldsymbol{B})$ which forces them on circular or helix-like trajectories around the magnetic field axis in real space [63, 65, 66]. In k-space, the charge carriers are constrained to a periodic movement on areas of constant energy normal to the magnetic field [67]. The angular frequency of this circular movement is called cyclotron frequency and is given by [39, 65–68]

$$\omega_\mathrm{c} = \frac{qB}{m} \ , \tag{29}$$

determined by the magnetic field strength B as well as the carrier mass m and charge q. For carriers in solid-state systems, the description is analogous. However, these states are characterized by their effective mass tensor $\hat{m}^*$ which takes into account the surrounding, periodic grid potential of the positively charged ions [64, 65]. The equation of motion for such a system with an isotropic effective mass m^* under the influence of an external, alternating electric field $\boldsymbol{E}$ is given by [63, 65, 68]

$$m^* \frac{\mathrm{d}\boldsymbol{v}}{\mathrm{d}t} = q\,(\boldsymbol{E} + \boldsymbol{v} \times \boldsymbol{B}) - \frac{m^* \boldsymbol{v}}{\tau} \ . \tag{30}$$

Here, an additional damping term proportional to the momentum relaxation rate $1/\tau$ is included that accounts for scattering of the carriers, e.g. on lattice impurities. When the frequency ω of the driving field $\boldsymbol{E}$ matches the cyclotron frequency of the charge carriers, a strong, resonant absorption of radiation is observed which is called cyclotron resonance [63, 65–68]. Sharp, well-defined resonances are obtained under the condition $\omega_\mathrm{c}\tau \gg 1$ [65, 66]. This ensures that carriers can perform closed loops in k-space around the magnetic field axis without being scattered off the cyclotron trajectory by impurities or phonons [67]. For a fixed frequency ω of the electric field, cyclotron resonance occurs

at a magnetic field strength corresponding to

$$B_{\mathrm{CR}} = \frac{m^* \omega}{q} \ . \tag{31}$$

To drive the cyclotron motion, the polarization of the electric field has to match the direction of the circular carrier motion so that resonant energy transfer from the electric field to the charge carriers becomes possible [66]. For a magnetic field with magnitude $|\boldsymbol{B}| = B_{\mathrm{CR}}$, parallel incident radiation is therefore absorbed resonantly by electrons (holes) when the electric field is left-handed (right-handed) circularly polarized [68]. Note that reversing the direction of the applied magnetic field inverts this correlation. This makes it possible to optically determine the prevailing carrier type in semiconductor structures [67]. In the following, magnetic fields for which the incident circularly polarized radiation field is absorbed resonantly are addressed as CR active, in contrast to CR inactive fields for which resonance conditions are not fulfilled.

The time-averaged, optical power absorption P per unit volume in case of right-handed (P_+) or left-handed (P_-) circularly polarized radiation incident parallel to the applied magnetic field is given by the Lorentzian function [63, 68]

$$P_{\pm}(\omega, \omega_{\mathrm{c}}) = \sigma_0 E_0^2 \frac{1}{1 + (\omega \pm \omega_{\mathrm{c}})^2 \tau^2} \ . \tag{32}$$

Here, E_0 is the magnitude of the electric field acting on the electrons and $\sigma_0 = qn\mu = q^2 n\tau/m^*$ denotes the static dc conductivity of a material with carrier density n, mobility μ, and momentum relaxation time τ. As a linear polarization state is represented by a superposition of right-handed and left-handed circular polarization states, resonant stimulation of the carrier cyclotron motion is also achieved for a linearly polarized, incident radiation field. The time-averaged, absorbed optical power per unit volume in this case is given by [65, 68]

$$P_{\mathrm{linear}}(\omega, \omega_{\mathrm{c}}) = \frac{\sigma_0 E_0^2}{4} \left(\frac{1}{1 + (\omega + \omega_{\mathrm{c}})^2 \tau^2} + \frac{1}{1 + (\omega - \omega_{\mathrm{c}})^2 \tau^2} \right) \ . \tag{33}$$

Hence, for linearly polarized radiation at a fixed frequency ω, cyclotron motion of electrons and holes is stimulated both for positive as well as negative

magnetic fields $\pm B_{\mathrm{CR}}$. It is important to mention that Eqs. (32) and (33) allow the extraction of the momentum relaxation time τ or mobility μ of the charge carriers from $P(\omega)$ or $P(B)$ curves with a fixed magnetic field or radiation frequency, respectively. For magnetoabsorption $P(B)$ at fixed radiation frequency, the full width at half maximum (FWHM) at CR is simply given by $\mathrm{FWHM} = \frac{2}{\mu}$ [65].

Note that radiative decay caused by coherent dipole reradiation can lead to an additional broadening of the resonance that has to be taken into account [69–71]. This effect arises when one relates the electric field which is acting on the electrons to the external field of the incoming wave. The external, oscillating field forces the charge carriers in the material to oscillate, which in turn causes them to emit a secondary radiation [69]. Because of strong reflection of the incoming wave near conditions of CR, this phenomenon leads to an additional effective broadening of the resonance linewidth governed by the superradiant decay rate which is given by [70]

$$\Gamma = \frac{n_{\mathrm{s}} e^2}{2\varepsilon_0 m^* c} \tag{34}$$

for a two-dimensional electron system with sheet carrier density n_{s}. The CR linewidth in the system is then determined by the collisional scattering rate $\gamma = 1/\tau$ plus the superradiant decay rate Γ [69]. From the ratio of these two contributions

$$\frac{\Gamma}{\gamma} = \frac{\sigma_0}{2\varepsilon_0 c} \tag{35}$$

it becomes clear that the line broadening due to radiative decay is of particular importance in well conducting systems with a high carrier mobility [69]. In fact, in systems with $\Gamma/\gamma \gg 1$, the main part of the incident radiation is reflected by the two-dimensional electron gas in the immediate vicinity of CR instead of being absorbed or transmitted [69].

In the quantum mechanical approach, CR is defined in terms of resonant, optical transitions between Landau levels [65]. The energy quantization into discrete Landau levels directly follows from solving the Schrödinger equation for a free electric charge subjected to a magnetic and electric field described

by the Hamiltonian [72]

$$\mathcal{H} = \frac{p_x^2}{2m} + \frac{1}{2m}\left(p_y - \frac{qBx}{c}\right)^2 + \frac{p_z^2}{2m} \ , \tag{36}$$

assuming a magnetic field $\boldsymbol{B} = (0, 0, B)$ applied along z-direction. In a solid-state system with a parabolic conduction band minimum, the corresponding Schrödinger equation for the electrons in the effective mass model reads [39, 66]

$$\left[\frac{p_x^2}{2m^*} + \frac{m^*\omega_\mathrm{c}^2}{2}\left(x - \frac{\hbar k_y}{m^*\omega_\mathrm{c}}\right)^2 + \frac{p_z^2}{2m^*}\right]\psi = E(\boldsymbol{k})\,\psi \ . \tag{37}$$

It is seen that Eq. (37) resembles the Schrödinger equation of a harmonic oscillator shifted in x-direction by $\frac{\hbar k_y}{m^*\omega_\mathrm{c}}$ and, thus, can be rewritten in the frame of the relative coordinate $\xi = x - \frac{\hbar k_y}{m^*\omega_\mathrm{c}}$ as [65, 66]

$$\left[\frac{p_\xi^2}{2m^*} + \frac{m^*\omega_\mathrm{c}^2}{2}\xi^2\right]\psi(\xi, \boldsymbol{k}) = \left[E_l(k_z) - \frac{\hbar^2 k_z^2}{2m^*}\right]\psi(\xi, \boldsymbol{k}) \ . \tag{38}$$

The energy of the l-th Landau level in systems with parabolic band dispersion is then given by [65, 66]

$$E_l(k_z) = \hbar\omega_\mathrm{c}\left(l + \frac{1}{2}\right) + E_z(k_z) \ , \qquad \text{with} \qquad E_z(k_z) = \frac{\hbar^2 k_z^2}{2m^*} \ , \tag{39}$$

and $l \in \mathbb{N}$. In this case, the Landau levels have an equidistant energy spacing of $\Delta_l = \hbar\omega_\mathrm{c} = \hbar qB/m^*$, see Fig. 10 (a). Due to dipole selection rules, optical transitions are only allowed between neighboring Landau levels [65, 66]. Note that the corresponding cyclotron magnetic field $B_\mathrm{CR} = |m^*\omega/q|$ scales linearly with radiation frequency ω. Moreover, B_CR is independent of the Fermi energy, as shown in Fig. 10 (a) for two different Fermi levels.

In two-dimensional systems with linear dispersion $E(\boldsymbol{k}) = \hbar v_\mathrm{F}\sqrt{k_x^2 + k_y^2}$, such as the surface states of three-dimensional topological insulators, the situation is different. Here, the energy of the l-th Landau level is calculated as [73–76]

$$E_l = \mathrm{sgn}(l)\,\hbar v_\mathrm{F}\sqrt{\frac{2eB\,|l|}{\hbar}} \ , \tag{40}$$

with the Fermi velocity v_F and the Landau level number $l \in \mathbb{Z}$. Positive level numbers $l > 0$ correspond to positive, electron-like Landau levels, whereas

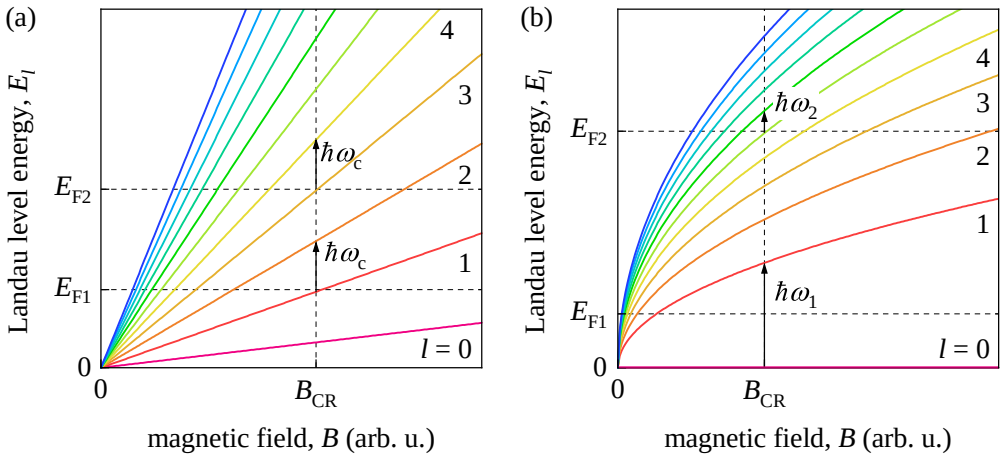

Figure 10: Panel (a) illustrates the Landau level spectrum in a system with parabolic dispersion. Shown are the energies E_l with respect to magnetic field B for the first Landau levels up to $l = 10$ and $E_z(k_z) = 0$. The transition energies $\hbar\omega_c$ between adjacent Landau levels and at a constant magnetic field are independent of the Fermi energy E_F, which is illustrated exemplarily for two Fermi levels E_{F1} and E_{F2}. Panel (b) depicts the Landau level spectrum for a two-dimensional system with linear dispersion. Shown is the upper part of the Landau spectrum with $l \geq 0$ (electron-like levels) up to $l = 10$. The cyclotron-resonant transition with energy $\hbar\omega_1$ at the bottom illustrates the quantum mechanical limit where $E_{F1} < \hbar\omega_1$. It is seen that in this case, the cyclotron frequency scales with the square root of B. In the semiclassical limit for $E_{F2} \gg \hbar\omega_2$, which is sketched in the upper transition, the cyclotron frequency approaches an almost linear scaling with magnetic field.

negative energies obtained for $l < 0$ represent hole-like Landau levels [76]. It is important to highlight that the Landau levels, in this case, scale with the square root of the magnetic field as well as the square root of the Landau level number, see Eq. (40). As a consequence, the quantized levels are no longer equidistant, but the energy difference Δ_l between two adjacent levels

$$\Delta_l = E_{l+1} - E_l = \hbar\omega_c = \hbar v_F \sqrt{\frac{2eB}{\hbar}} \left(\mathrm{sgn}(l+1)\sqrt{|l+1|} - \mathrm{sgn}(l)\sqrt{|l|} \right), \tag{41}$$

and therefore also the cyclotron frequency ω_c become dependent on B and l [74].

In the strict, quantum mechanical limit where the Fermi energy is smaller than the resonant photon energy, i.e. $E_F < \hbar\omega_c$, the cyclotron frequency scales with the square root of the magnetic field according to Eq. (41) [75]. This case is sketched in Fig. 10 (b) for the transition from the $l = 0$ to the $l = 1$ state at $E_{F1} < \hbar\omega_1$. However, in the semiclassical limit where the Fermi energy is much

larger than the radiation energy, i.e. $E_\mathrm{F} \gg \hbar\omega_\mathrm{c}$, the cyclotron frequency scales approximately linear with magnetic field [74]. This is illustrated in Fig. 10 (b) for the transition at $E_\mathrm{F2} \gg \hbar\omega_2$. In this limit of high Landau levels with $l \gg 1$, the cyclotron frequency can be expressed as [74]

$$\omega_\mathrm{c} = v_\mathrm{F}\sqrt{\frac{2eB}{\hbar}}\left(\sqrt{l+1}-\sqrt{l}\right) \approx v_\mathrm{F}\sqrt{\frac{2eB}{\hbar}}\frac{1}{2\sqrt{l}} \; . \tag{42}$$

Considering the cyclotron-resonant transition from level l, which has an energy roughly equivalent to the Fermi energy, to level $l+1$ it follows from

$$E_\mathrm{F} \approx E_l \qquad \text{that} \qquad \sqrt{l} \approx \frac{E_\mathrm{F}}{v_\mathrm{F}\sqrt{2\hbar eB}} \; , \tag{43}$$

which, when inserted into Eq. (42), gives [74]

$$\omega_\mathrm{c} \approx \sqrt{\frac{2eB}{\hbar}}\frac{v_\mathrm{F}}{2}\cdot\frac{v_\mathrm{F}}{E_\mathrm{F}}\sqrt{2\hbar eB} = \frac{v_\mathrm{F}^2}{E_\mathrm{F}}eB = \frac{eB}{m^*} \propto B \; . \tag{44}$$

Here, it was taken into account that in systems with linear dispersion, the mass becomes a function of the Fermi energy according to [74, 77]

$$m^* = \frac{E_\mathrm{F}}{v_\mathrm{F}^2} \; . \tag{45}$$

Thus, in the semiclassical limit $E_\mathrm{F} \gg \hbar\omega_\mathrm{c}$, the Landau levels in systems with linear dispersion approach an almost equidistant spacing and the cyclotron frequency exhibits a similar, linear magnetic field dependence as observed in systems with parabolic dispersion. The only difference to the parabolic case is that the cyclotron mass in linear dispersion systems becomes dependent on carrier density [8, 74, 77]. Note that the studies presented in this work mostly focus on the semiclassical regime of high Landau levels.

3 Experimental techniques and methods

This chapter provides an overview of the experimental setup and devices used for terahertz spectroscopy, including a detailed description of the techniques for photocurrent, photoconductivity, and radiation transmission measurements.

3.1 Laser setup

For optical excitation of the investigated samples, terahertz molecular gas lasers in continuous wave (cw) and pulsed operation modes were used. The lasing in this devices is based on rotational transitions in polar molecules with a permanent dipole moment [56, 79, 83]. Methanol, difluoromethane, formic acid, and ammonia were used as active media gases for the measurements in this work. The variety of optical transitions in these molecules gives access to an abundance of different laser lines in the terahertz range of frequencies [56, 83]. Table 1 gives a comprehensive listing of all utilized laser lines, as well as the respective active media, excitation frequencies, and operation modes. The media is optically pumped by mid-infrared radiation that excites vibrational-rotational transitions in the molecules following the selection rules for symmetric top molecules $\Delta\nu = 1$, $\Delta J = 0, \pm 1$, and $\Delta K = 0$ [79], as shown in Fig. 11 (b). Subsequently, far-infrared (FIR) radiation is generated as a result of the purely rotational transitions between J' and $J' - 1$ in the upper, and $J + 1$ and J in the lower vibrational state [79, 83].

The CO_2 lasers, which provide the mid-infrared pumping radiation for the terahertz lasers, consist of a gas mixture of carbon dioxide, nitrogen, and helium and are pumped electronically via high-voltage electron discharge [56, 78]. Radiative transitions take place between different vibrational modes in the CO_2

λ (µm)	f (THz)	E_{ph} (meV)	λ_{CO_2} (µm)	operation mode	active medium
118	2.54	10.5	9.695	cw	methanol (CH_3OH)
148	2.03	8.4	9.676	pulsed	ammonia (NH_3)
184	1.63	6.7	9.210	cw	difluoromethane (CH_2F_2)
432	0.69	2.9	9.271	cw	formic acid (CH_2O_2)

Table 1: Overview of the wavelengths λ, frequencies f, photon energies E_{ph}, corresponding pumping wavelengths λ_{CO_2}, operation modes, and active media gases for the laser lines used in the experiments.

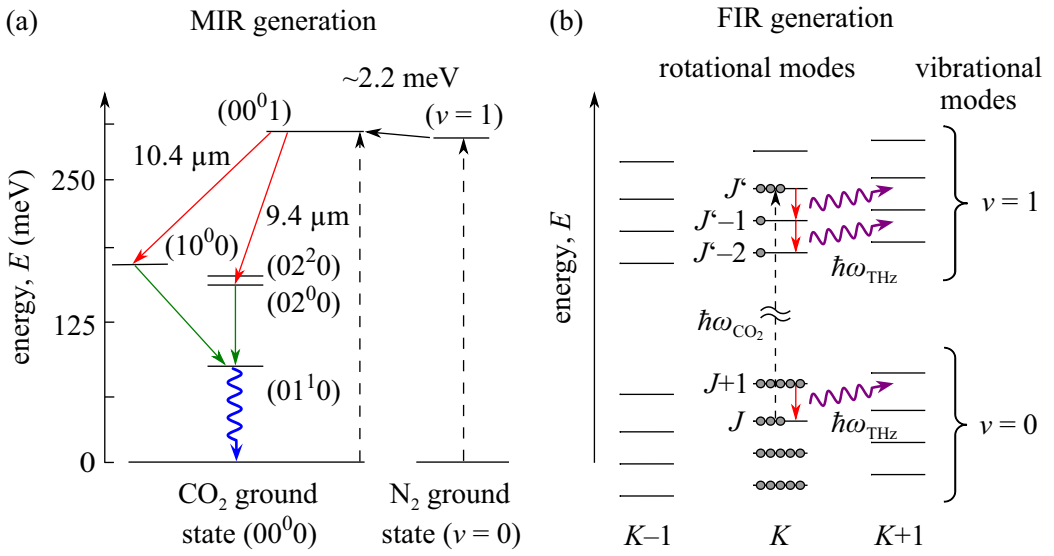

Figure 11: Panel (a): Scheme of the energetic levels and transitions relevant for lasing in the CO_2 laser. Dashed arrows represent the pumping of CO_2 and N_2 molecules by electron collisions, while the solid black arrow indicates the almost resonant energy transfer (with energy difference around 2.2 meV) between the excited N_2 and CO_2 molecules. The red lines mark the lasing transitions with lines centered around 9.4 µm and 10.4 µm, while green and blue arrows highlight radiative and non-radiative transitions, respectively. Note that rotational sublevels are not depicted for clarity of presentation. Figure adapted from Refs. [56] and [78]. Panel (b) shows a sketch of the lasing mechanism in a THz molecular gas laser. Solid black lines indicate the rotational energy sublevels in a symmetric top molecule for the vibrational ground ($\nu = 0$) and first excited ($\nu = 1$) level. K denotes the projection of the angular momentum J on the symmetry axis of the molecule. The dashed arrow indicates optical pumping, while the red arrows illustrate the lasing transitions that emit THz radiation. Figure adapted from Refs. [79] and [56].

molecule [56, 78, 84], as sketched in Fig. 11 (a). The energetically highest mode, the antisymmetric stretching mode (00^{0}1), is excited by both direct collisions with accelerated electrons and resonant collisional energy transfer from nitrogen molecules that have been excited to their first metastable vibrational level by electron impact [56, 78, 84]. From the (00^{0}1) state, radiative transitions take place to the energetically lower bending mode (02^{0}0) at $f = 32$ THz ($\lambda = 9.4$ µm) or to the symmetric stretching mode (10^{0}0) at $f = 29$ THz ($\lambda = 10.4$ µm) [56]. The subsequent depletion of the lower levels is caused by optical transitions allowed due to the Fermi resonance between the (10^{0}0) and (02^{0}0) levels, as well as by non-radiative relaxation processes including collisions with helium atoms [56, 78, 84]. As the energies of the vibrational levels in the CO_2 molecule are further split into rotational sublevels, the vibrational-rotational transitions can be tuned in a wide range around the two center

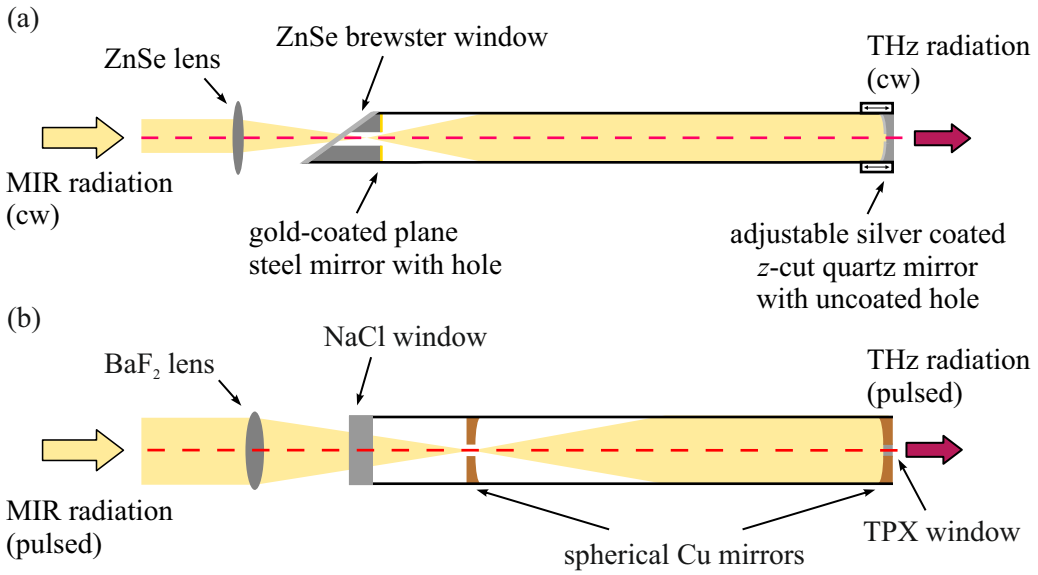

Figure 12: Sketch of the continuous wave (a) and pulsed (b) terahertz molecular gas lasers. Panel (a) shows how cw MIR radiation from a longitudinally pumped CO_2 laser is focused into the resonator of the cw terahertz gas laser (Edinburgh Instruments 295FIR). Panel (b) depicts the resonator of the pulsed terahertz laser which is pumped by pulsed MIR radiation from a TEA CO_2 laser. In both panels, the red dashed line corresponds to the optical path. Picture adapted from Refs. [80], [81] and [82].

frequencies from approximately 27 THz to 33 THz (around 9.2 µm to 10.9 µm) [84]. Please note that two different types of CO_2 lasers were used for optical pumping of continuous wave and pulsed terahertz lasers. The continuous wave molecular gas laser was pumped by a longitudinally-excited flowing gas CO_2 laser (Edinburgh Instruments PL5), operating at a low gas pressure of about 25 mbar and providing radiation powers up to around 50 W. On the other hand, a transversely-excited atmospheric pressure (TEA) CO_2 laser with a pulse duration of about 100 ns and peak pulse powers up to megawatts was used to pump the pulsed terahertz gas laser.

Figures 12 (a) and (b) present sketches of the two different types of resonators used for generating continuous wave and pulsed terahertz radiation, respectively. In the continuous wave system, ZnSe windows are mounted at the Brewster angle $\phi_B = \arctan(n_{window}/n_{air})$ [85] on the radiation exit of the CO_2 and the rear entrance of the terahertz molecular gas resonator to ensure a high degree of linear polarization of the pumping MIR radiation. Here, n_{window} and n_{air} denote the refractive indices of the ZnSe window and air, respectively. The cw FIR resonator consists of a glass cylinder with a gold-coated, steel mirror including a coupling hole in the middle and a movable, silver-coated, z-cut quartz mirror with an uncoated part in the middle to couple out the

generated terahertz beam, but prevent MIR pumping radiation from leaving the resonator [83]. In the pulsed system, the MIR pumping radiation from the TEA CO_2 laser is focused by a BaF_2 lens and coupled into the FIR resonator via a NaCl window. The resonator itself is comprised of a glass cylinder with two spherical Cu mirrors with a hole in the middle. Note that the output hole in the front contains a polymethylpentene (TPX) window which transmits the generated terahertz beam but absorbs residual MIR pumping radiation.

To ensure a linear polarization of the THz beam at all frequencies, linear wire-grid or polyethylene polarizers were used [56, 79]. In general, assuming linearly polarized pumping radiation, the polarization of the generated FIR emission depends on the change of the angular momentum J in the pumping and lasing transitions. If $|\Delta J|$ is the same for both transitions, the electric fields of pump and terahertz beam are polarized parallel to each other. On the other hand, if $|\Delta J|$ is not the same in both cases, the two beams are polarized orthogonally to each other [86]. Furthermore, the degree of linear polarization of the FIR output is high if the pump excites states, where the projection K of the angular momentum J on the symmetry axis of the molecule fulfills the condition $K \ll J$. At the same time, the degree of linear polarization is low for excited molecular levels where K is similar to J [56].

For both the cw and pulsed FIR system, the beam shape was monitored by a pyroelectric camera. The respective parameters were adjusted to obtain a mode shape as close as possible to the Gaussian fundamental mode [56]. A typical beam profile is shown in Fig. 14 (b). Continuous wave beam powers were measured with a power meter and range from around 15 mW to 100 mW depending on the specific laser line. For the pulsed line with $f = 2.03$ THz, a peak power of 70 kW was detected using a photon drag detector. The frequency-dependent beam diameters, defined as the full width at half maximum of detected power, were extracted from the beam profiles and range from 1.5 mm to 3 mm for the laser lines given in Tab. 1. Corresponding radiation intensities I_R were calculated based on the extracted beam diameters and powers.

In the experiments, the initial linear polarization of the FIR laser was further manipulated with the help of $\lambda/2$- or $\lambda/4$-waveplates. These waveplates are made of a birefringent material and exploit the existence of two different refraction indices n_o and n_{eo} for electric fields polarized along the ordinary and extraordinary axes, both oriented at a 90° angle with respect to each other [79]. A phase shift is generated between the two electric field components $E_{\parallel}$

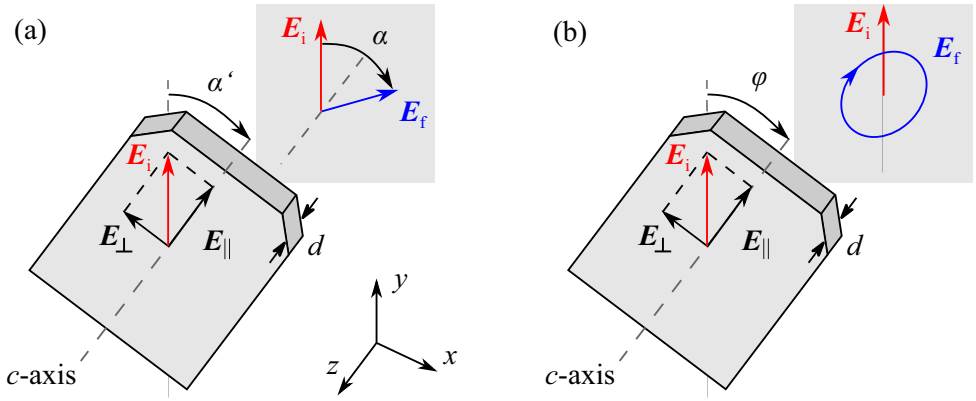

Figure 13: Panels (a) and (b) sketch the function principle of a $\lambda/2$- and $\lambda/4$-waveplate, respectively. In (a), the incoming, linearly polarized electric field $\boldsymbol{E}_\mathrm{i}$ enters the half-wave plate at an angle α' relative to the optical c-axis indicated by the dashed line. The electric field $\boldsymbol{E}_\mathrm{f}$ after the $\lambda/2$-waveplate is rotated by the angle $\alpha = 2\alpha'$ with regard to $\boldsymbol{E}_\mathrm{i}$. In (b), the angle φ between the incident, linearly polarized electric field $\boldsymbol{E}_\mathrm{i}$ and the c-axis leads to an outgoing, elliptically polarized electric field $\boldsymbol{E}_\mathrm{f}$. The thickness of the wave plates is indicated by d. Figures after Refs. [80] and [87].

and $E_\perp$ due to their different propagation velocities inside the medium [79, 85]. Here, $E_\parallel$ and $E_\perp$ denote the field components parallel and normal to the extraordinary or also called optical c-axis. The phase shift [79]

$$\Delta\phi = kd\,(n_\mathrm{o} - n_\mathrm{eo}) = \frac{2\pi}{\lambda} d\Delta n \qquad \text{with} \qquad \Delta n = n_\mathrm{o} - n_\mathrm{eo} \tag{46}$$

is dependent on the thickness d of the waveplate and the wavelength λ (or wavevector $k = \frac{2\pi}{\lambda}$) of the radiation [85].

For $\lambda/2$-waveplates, the phase shift $\Delta\phi$ between the two perpendicular field components is $(2j+1)\pi$, with j being the integer numbering order. Under this condition, the polarization plane of incident linearly polarized light is rotated after the waveplate by the azimuthal angle α [79], as shown in Fig. 13 (a). Here, $\alpha = 2\alpha'$ depends on the angle α' between the incident polarization plane and the c-axis of the $\lambda/2$-waveplate. In case of $\lambda/4$-waveplates, the phase shift inside the birefringent medium is $(2j + \frac{1}{2})\pi$, which can lead to a change of the polarization state from linear to circular or elliptical, or vice versa [79]. Whether incident linearly polarized radiation fields are changed to circular or elliptical polarization depends on the phase angle φ between the incident polarization plane and the optical axis in the $\lambda/4$-waveplate. For $\varphi = l\frac{\pi}{2}$ (with $l \in \mathbb{Z}$), the polarization state is not changed at all, i.e. the final polarization is parallel to the incident one. However, for $\varphi = \frac{\pi}{4} + l\pi$ or $\varphi = \frac{3}{4}\pi + l\pi$, the waveplate changes the incident linear polarization to right-handed (σ^+)

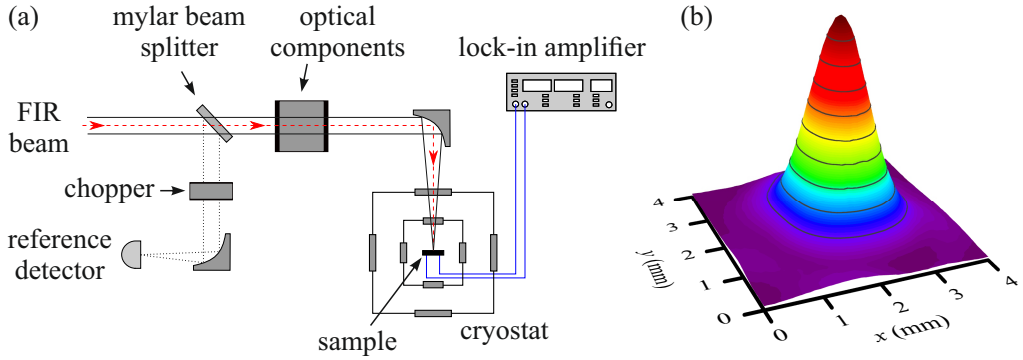

Figure 14: Panel (a): Sketch of the principal measurement setup. Note that the optical components include linear polarizers, half- or quarter-wave plates, as well as an optical chopper which modulates the beam at a given frequency f_{chop}. Figure adapted from Refs. [82] and [87]. Panel (b) depicts an exemplary FIR beam profile obtained with a pyroelectric camera at a radiation frequency of $f = 2.54\,\mathrm{THz}$.

or left-handed (σ^-) circular polarization, respectively. For angles φ between these values, the polarization is changed from linear to elliptical, as sketched in Fig. 13 (b).

For polarization manipulation of the terahertz laser beam used in the experiments, several half-wave and quarter-wave plates made of x-cut crystalline quartz with different thicknesses were used. This material is ideal for this purpose, since it is strongly birefringent with $\Delta n \approx 0.047$ at room temperature as well as highly transparent for terahertz radiation [79, 88].

3.2 Experimental Setup

For the measurements, the samples were placed in an optical helium bath cryostat (Oxford Instruments Spectromag SM4000-8) with windows made of z-cut crystalline quartz or polymethylpentene (TPX), which are both highly transparent in the terahertz range of frequencies [56, 83]. Note that in contrast to the above mentioned x-cut crystalline quartz, z-cut crystalline quartz does not modify the polarization of transmitted light. The THz beam was focused onto the samples using gold-coated off-axis parabolic mirrors, as shown in Fig. 14 (a). A red HeNe laser aligned with the THz beam allowed proper adjustment and position control of the THz spot on the sample [56]. After adjustment, the cryostat windows were completely covered with black polyethylene foil that is transparent in the THz range but inhibits uncontrolled illumination of the samples by room light or near-infrared radiation. To monitor the power output of the FIR laser during the experiments, a small, constant fraction of

the THz beam was deflected onto a pyroelectric reference detector using a mylar beam splitter [56]. In case of continuous wave operation, the reference beam was mechanically chopped and the reference signal was analyzed by a lock-in amplifier tuned to the frequency of modulation. Feeding this signal to a laser stabilizer (Edinburgh Instruments ALS-1) allowed to minimize fluctuations in the continuous wave output power.

Most measurements were carried out at a temperature of $T = 4.2\,\mathrm{K}$, which was obtained by flooding the sample chamber with liquid helium. Even lower temperatures down to $T = 1.6\,\mathrm{K}$ were achieved by additional pumping of the sample chamber to bring the helium into its superfluid state. It was furthermore possible to stabilize the sample at any temperature between liquid helium and room temperature by placing a PID-controlled ohmic heater in proximity to the sample and adjusting the helium flow with a needle valve. The actual sample temperature was monitored by Cernox sensors in close vicinity to the sample mount. All measurement devices were controlled and read out via General Purpose Interface Bus (GPIB) by measurement software written in LabVIEW and Python. For magnetotransport and terahertz magnetospectroscopy, magnetic fields up to 7 T were applied normal as well as parallel to the sample using a liquid helium-cooled superconducting split coil magnet.

Magnetotransport. In all investigated samples, dark magnetotransport measurements were carried out to characterize the electrical properties and extract the carrier densities and mobilities. In most cases, standard low-frequency lock-in amplifier technique in a four-terminal measurement scheme was used. An alternating bias current I_{ac} in the range of $10^{-9}\,\mathrm{A}$ to $16 \cdot 10^{-6}\,\mathrm{A}$ was applied to the sample using an ac voltage source and a series resistor with resistance R_{ac} ranging from $10^6\,\Omega$ to $10^8\,\Omega$. In Hall bar shaped samples the longitudinal R_{xx} and transversal (Hall) resistance R_{xy} were then obtained by measuring the voltage drop parallel and perpendicular to the applied current, respectively, and dividing it through the applied current. Enough distance between the current and voltage probes ensured the current flow between the voltage probes to be as homogeneous as possible under the influence of an external magnetic field applied normally to the sample plane [39]. The Hall bar design allows the extraction of the sheet resistivity ρ_{xx} from the longitudinal

resistance according to [39]

$$\rho_{xx} = R_{xx}\frac{W}{L} \ , \tag{47}$$

simply by considering the width W of the conduction channel and the distance L between the two voltage probes.

Obtaining the sample resistivity in van der Pauw samples required another procedure. For an arbitrary shaped sample with four contacts at the edges termed A, B, C and D, one has to measure the non-local resistance $R_{\mathrm{AB,CD}} = V_{\mathrm{CD}}/I_{\mathrm{AB}}$. After a cyclic permutation of the contacts, and in this way obtaining the resistance $R_{\mathrm{BC,DA}} = V_{\mathrm{DA}}/I_{\mathrm{BC}}$, the relation [89, 90]

$$\exp\left(-\frac{\pi d}{\rho}R_{\mathrm{AB,CD}}\right) + \exp\left(-\frac{\pi d}{\rho}R_{\mathrm{BC,DA}}\right) = 1 \tag{48}$$

can be used to calculate the resistivity

$$\rho = \frac{\pi d}{\ln 2} \cdot \frac{R_{\mathrm{AB,CD}} + R_{\mathrm{BC,DA}}}{2} \cdot F \ . \tag{49}$$

Here, d is the sheet thickness and F denotes the form factor which is dependent on the ratio $R_{\mathrm{AB,CD}}/R_{\mathrm{BC,DA}}$ and derived in Refs. [89, 90]. Given almost square shaped samples where $R_{\mathrm{AB,CD}} \approx R_{\mathrm{BC,DA}}$, the form factor can be assumed as unity and the sheet resistivity is then given by

$$\rho_{xx} \approx \frac{\pi}{\ln 2}R_{\mathrm{AB,CD}} \ . \tag{50}$$

The Hall resistance in van der Pauw samples was measured analogously to Hall bar samples by probing the voltage drop over two contacts perpendicular to the applied current and divide it through the latter. Note that in van der Pauw geometry, the available current and voltage probe directions may not be aligned exactly perpendicular to each other. To account for this fact, the resistance was measured for the two configurations $R_{\mathrm{AC,BD}}(B)$ and $R_{\mathrm{BD,CA}}(B)$. The Hall resistivity was then calculated as [39]

$$\rho_{xy}(B) = \frac{1}{2}\Big(R_{\mathrm{AC,BD}}(B) + R_{\mathrm{BD,CA}}(B) - R_{\mathrm{AC,BD}}(0) - R_{\mathrm{BD,CA}}(0)\Big) \ . \tag{51}$$

In contrast to Hall bar or van der Pauw geometry, Corbino disk samples only have two contacts, i.e. inner and outer ring contact. Thus, this type of sample

geometry only allows two-terminal measurements. The longitudinal conductivity σ_{xx} was extracted from transport measurements of the resistance R between the inner and outer contact according to [39]

$$\sigma_{xx} = \frac{\ln\left(\frac{r_\mathrm{o}}{r_\mathrm{i}}\right)}{2\pi}\frac{1}{R} \ . \tag{52}$$

Here, r_i and r_o denote the radii of the inner and outer ring contact, respectively. It is important to mention that the conductivity obtained in Corbino disk samples usually is smaller than in Hall bar samples made from the same material due to the unavoidable contribution of the contact resistance in two-terminal measurements [39].

From the dark magnetotransport data, the two-dimensional sheet carrier density n_s was obtained in two different ways. In most cases, it was calculated from the slope of the magnetic field dependence of the Hall resistivity $\rho_{xy}(B)$ obtained for a field applied perpendicular to the sample plane. For two-dimensional systems, n_s was additionally extracted from the period of Shubnikov-de Haas oscillations in the magnetic field dependence of the longitudinal sheet resistivity $\rho_{xx}(B)$ [39]. The carrier mobility μ was calculated from the carrier density and sheet resistivity without applied magnetic field via [39]

$$\mu = \frac{1}{n_\mathrm{s} \cdot e \cdot \rho_{xx}(B=0)} \ . \tag{53}$$

Photosignals. The optoelectronic response of the samples to incident terahertz radiation was probed in different ways. Photogalvanic signals were obtained by measuring the current or voltage in the unbiased samples arising due to the incident THz beam. Continuous wave laser radiation was modulated with a mechanical chopper at a frequency f_chop ranging between 70 Hz and 150 Hz, which allows detection of the photosignals by lock-in amplifier technique. For pulsed excitation, the temporal evolution or peak values of the photosignals were monitored by a GHz digital storage oscilloscope. Photovoltage was picked up over two sample contacts by voltage probes with an internal resistance of $R_\mathrm{i} = 10\,\mathrm{M\Omega}$. Photocurrents were measured as the voltage drop ΔV over a load resistor with a defined resistance R_L in parallel to the sample.

From this, the corresponding photocurrent can be calculated by

$$I_{\mathrm{ph}} = \frac{\Delta V}{R_{\mathrm{total}}} = \frac{\Delta V}{\left(\frac{1}{R_{\mathrm{s}}} + \frac{1}{R_{\mathrm{L}}}\right)^{-1}} \approx \frac{\Delta V}{R_{\mathrm{L}}} \ , \tag{54}$$

where in the last step it was assumed that the load resistance R_{L} is significantly smaller than the sample resistance R_{s}.

The radiation-induced change of the sample conductivity or resistivity was measured by additionally applying a constant dc bias V_{dc} to the sample and repeating the measurement for two inverted bias directions $\pm V_{\mathrm{dc}}$. According to Eq. (26), the photoconductive response is proportional to the applied bias, whereas the photogalvanic signal contributions are bias-independent. Therefore, possible photocurrent contributions can be eliminated by subtraction of the two signals obtained at inverted bias directions. Note that an additional division by a factor of 2 is necessary for correct normalization of the photoconductivity. In some cases, photoconductivity was additionally measured with the double-modulation method, where both bias current as well as laser radiation were modulated at different frequencies and the resulting signal was read out by two lock-in amplifiers in series (see for example Refs. [91] or [23]). Instead of the dc bias in the method described earlier, here an ac bias was applied at a low frequency f_{ac} and the laser beam was modulated at a substantially higher frequency $f_{\mathrm{chop}} \gg f_{\mathrm{ac}}$. In this method, the first lock-in amplifier is tuned to the higher frequency f_{chop} and gives an output signal that consists of a constant photogalvanic signal on top of a slowly oscillating component. This signal is then fed into a second lock-in amplifier tuned to f_{ac}, which yields a constant signal proportional to the photo-induced change of conductivity/resistivity. Note that to achieve proper results with this method, amplifier settings such as integration time or band filter slope have to be adjusted properly to the modulation frequencies f_{ac} and f_{chop} [23].

Radiation transmission. In addition to measurements of the photo-induced variation of electrical properties described above, the transmission of terahertz radiation through the samples was also monitored during the experiments. To this end, the samples were mounted on special sample holders with a hole drilled into the back plane. The hole diameter exceeded the frequency-dependent beam diameters of the THz laser radiation. This allowed the transmitted THz beam to exit the cryostat through the rear window, where it was

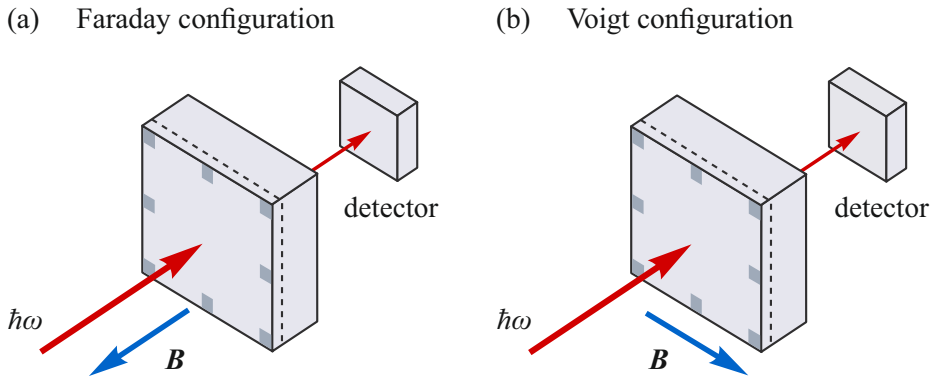

Figure 15: Sketch of the setup for magnetotransmission measurements. Panel (a) shows the Faraday configuration with the terahertz beam incident normally on the sample surface and the external magnetic field applied antiparallel to the beam. In contrast, in Voigt configuration (b) the magnetic field is applied parallel to the sample plane, i.e. perpendicular to the laser beam. Adapted from Ref. [30].

focused onto a pyroelectric detector using a parabolic mirror. The detector measured a voltage signal proportional to the incident power, which was further processed using standard lock-in amplifier technique as described above. For more information on the functional principle of pyroelectric detectors see, e.g., Ref. [79]. In the magnetotransmission experiments, the laser beam typically hit the sample at a normal incidence and an external magnetic field was applied either parallel/antiparallel or normal to the incident THz beam, see Fig. 15. These two measurement configurations depicted in Figs. 15 (a) and (b) are referred to as Faraday and Voigt configuration, respectively.

4 Investigated samples

In this thesis, two different types of heterostructures from the MCT compound system were studied, namely CdHgTe/HgTe/CdHgTe quantum wells with different widths as well as bulk films made from $Cd_xHg_{1-x}Te$ alloys with different compositions of CdTe and HgTe. Both structure types are very attractive semiconductor materials for optoelectronical investigations since they are highly tunable in their gap energy, as pointed out in Chap. 2.2. In particular, topological phase transitions can be easily realized by a variation of characteristic structure parameters, such as the HgTe quantum well width d, the cadmium content x in $Cd_xHg_{1-x}Te$ alloys, and even by changing the temperature. Hence, both structure types provide access to inverted and non-inverted parabolic spectra as well as Dirac-like states directly at the topological transition point. This allows the comparison of phenomena excited for different electronic dispersions in one material system [20]. Several samples from the topologically trivial and non-trivial regime were studied in this work. The wafers used for sample fabrication were grown by S. A. Dvoretsky, N. N. Mikhailov, and their team at the Rzhanov Institute of Semiconductor Physics in Novosibirsk by molecular beam epitaxy. All important technical details on wafer growth and material design, as well as information on the sample fabrication and specifications are presented in this chapter. Furthermore, magnetotransport characterization data are shown along with the extracted sample parameters.

4.1 HgTe quantum wells

First, the HgTe/CdHgTe quantum well structures investigated in this work are addressed. They were grown by molecular beam epitaxy according to the heterostructure design sketched in Fig. 16. On top of the either (013)- or (001)-oriented GaAs substrate, these structures include a 5 nm thick layer of ZnTe, followed by a 6 µm wide CdTe buffer layer, which leads to the adaptation of the lattice constant of CdTe [5]. The barriers on both sides of the HgTe quantum well are formed by 30 nm $Cd_{0.4}Hg_{0.6}Te$ layers, while the thickness d of the HgTe QW itself varies and ranges between 5 nm and 20 nm in the investigated samples. Thin indium δ-doping layers were buried symmetrically inside the otherwise undoped $Cd_{0.4}Hg_{0.6}Te$ barrier layers at a distance of around 10 nm from the HgTe quantum well [92]. On top, all heterostructures were capped

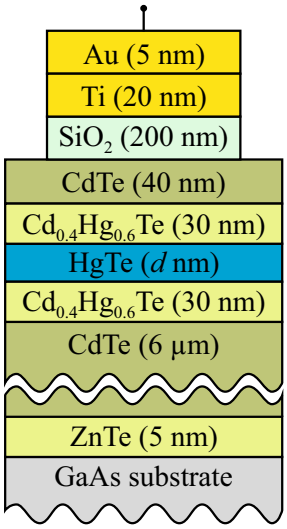

Figure 16: Illustration of the layer structure of the HgTe quantum wells used for preparation of samples #1 to #7. Note that the top part consisting of the SiO_2, gold and titanium layers is only present in sample #1. Adapted from Ref. [23].

with a 40 nm CdTe layer for protection since CdTe is mechanically more robust than HgTe or CdHgTe alloys [2]. During the growth process, the composition and thickness of the layers were controlled by light beam ellipsometry [92].

For electro-optical measurements, the wafers were prepared into samples with Hall bar, Corbino disk and square geometry. The Hall bars with length l and width w were fabricated by optical lithography. Center and outer ring contacts of Corbino disk samples were manufactured on top of the heterostructure via indium diffusion, resulting in a Corbino disk with inner and outer radii r_i and r_o, respectively. Additionally, sample #1 was equipped with a semitransparent gate made of 20 nm titanium and 5 nm gold layers evaporated on top of the heterostructure, separated by a 200 nm wide insulating SiO_2 layer, as illustrated in Fig. 16. As already pointed out in detail in Chap. 2.2, the width d strongly influences the band dispersion of the quantum well. Samples #1 and #2 with $d = 20\,\mathrm{nm}$ as well as sample #3 with $d = 8\,\mathrm{nm}$ exhibit inverted, roughly parabolic bulk bands along with Dirac-like helical edge states lying within the bulk energy gap. By contrast, bulk states with an almost linear spectrum are realized in sample #4 ($d = 6.6\,\mathrm{nm}$) as well as samples #5 and #6 (both $d = 6.5\,\mathrm{nm}$) with QW widths close to the critical thickness d_c. Sample #7 with $d = 5\,\mathrm{nm} < d_\mathrm{c}$ corresponds to a regular narrow-gap semiconductor with trivial band ordering.

All samples were characterized in the absence of irradiation by low-frequency magnetotransport measurements at liquid helium temperature with out-of-

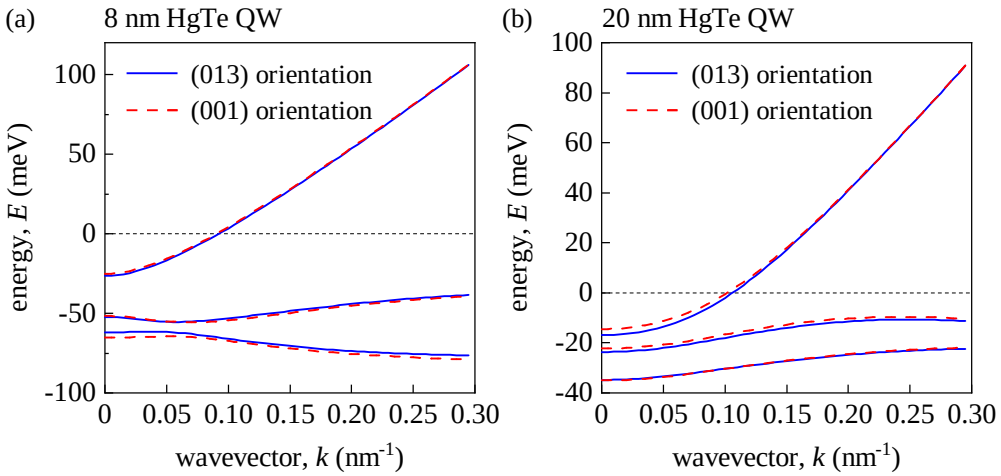

Figure 17: Results of $\boldsymbol{k} \cdot \boldsymbol{p}$ calculations for the bulk band dispersion in HgTe quantum wells with width $d = 8\,\text{nm}$ (a) and $d = 20\,\text{nm}$ (b). The solid blue and dashed red traces show the dispersion of the bands along [100]-direction for (013)- and (001)-oriented samples, respectively. The curves were calculated by G. V. Budkin [93].

plane magnetic fields up to 7 T. Table 3 gives an overview of all QW samples including their respective QW widths, sample geometries, and characteristic parameters. Additionally, $\boldsymbol{k} \cdot \boldsymbol{p}$ calculations of the band structure of the investigated HgTe quantum wells were carried out by Dr. G. V. Budkin from the Ioffe Institute in St. Petersburg. The data for 8 nm and 20 nm wide QWs are presented in Fig. 17. In both cases, a comparison of the relevant energy bands for (013)- and (001)-oriented structures (see solid and dashed lines in Fig. 17) demonstrates that the change of orientation has only a negligibly small influence on the band dispersion.

4.2 $Cd_xHg_{1-x}Te$ bulk films

The $Cd_xHg_{1-x}Te$ films for this study were grown via molecular beam epitaxy in a similar fashion than the HgTe quantum wells described in the previous chapter. Fig. 18 (a) sketches the principal design of such a film. As basis, a (013)-oriented GaAs substrate with epitaxial layers of ZnTe (30 nm) and pure CdTe (6 µm) was used. This structure served as a virtual substrate for the $Cd_xHg_{1-x}Te$ bulk films that were grown on top with a thickness ranging from 5 µm to 12 µm. Samples #A, #B, #D and #E (see Figs. 18 (b), (c), (e) and (f)) have a conventional design with a gradually varying cadmium content x at the bottom and top interface of the film, enclosing a wide region where the cadmium concentration is kept constant at $x = 0.15$ (samples #A and #B),

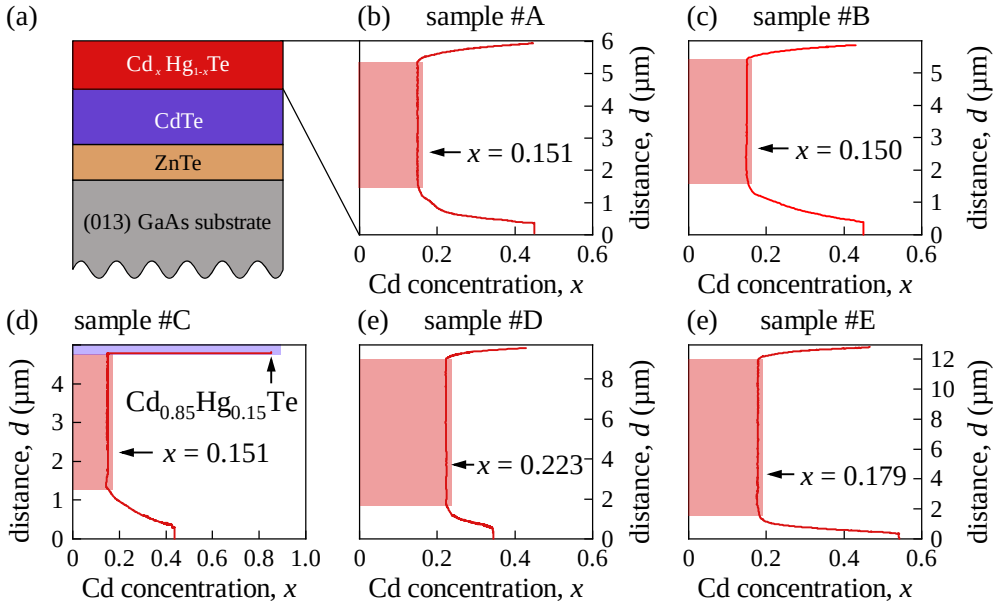

Figure 18: Panel (a): Schematic illustration of the principal structure of all investigated $Cd_xHg_{1-x}Te$ films. The specific design of the individual $Cd_xHg_{1-x}Te$ films is displayed in panels (b) to (f), which show the cadmium concentration profile $x(d)$ as a function of the distance d from the top of the preceding CdTe layer (colored in purple in panel (a)). A light red background highlights the flat regions with a Cd content as indicated in each panel. Note that in contrast to all other structures where $x(d)$ varies smoothly, sample #C has a sharp interface between the flat region with $x = 0.15$ and the 30 nm cap layer with $x = 0.85$, as highlighted by the blue background in panel (d). Adapted from Ref. [30].

$x = 0.18$ (sample #D), or $x = 0.22$ (sample #E). This region ranges from a thickness of around 3 µm to 10 µm depending on the specific structure and will be called flat region in the following. Smooth interfaces with varying x around the flat region were shown to improve optoelectronic and electronic transport properties of the structures [3] due to, e.g., a reduction of interface disorder effects and lattice mismatch-induced strain. However, sample #C (see Fig. 18 (d)) omits the gradual increase of x at the top interface and introduces a sharp transition from the flat region with $x = 0.15$ to a 30 nm thick $Cd_{0.85}Hg_{0.15}Te$ cap layer. This results in a sharp boundary between the flat region with inverted and the cap layer with regular, non-inverted band ordering. Precise information about the structure of all investigated $Cd_xHg_{1-x}Te$ bulk films is presented in Figs. 18 (b) to (f). During preparation, the wafer material was cut into small, square-shaped pieces with a size of around 5 mm × 5 mm. Ohmic indium contacts were soldered to the sample edges and corners, resulting in a van der Pauw geometry. Additionally, micrometer-sized Hall bar samples were fabricated by optical lithography from several wafers to allow for

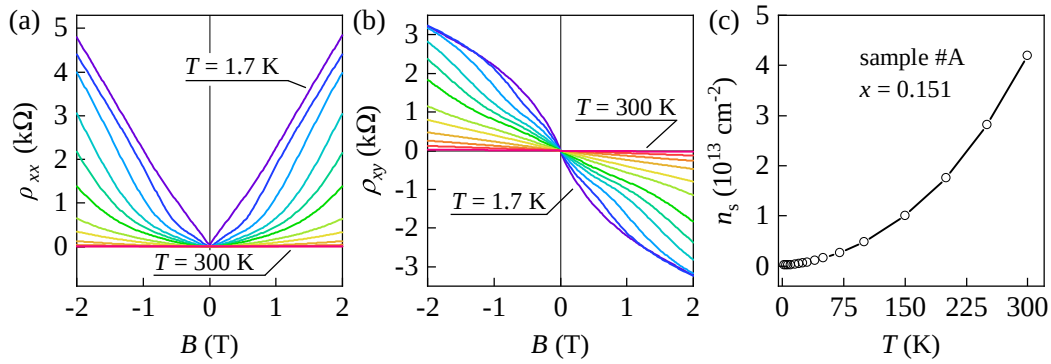

Figure 19: Magnetotransport data of a Hall bar sample made from wafer #A with $x = 0.15$ for different temperatures, $T = 1.7\,\mathrm{K}$ (purple curve), 10 K (dark blue curve), 15 K (light blue curve), 20 K, 25 K, 30 K, 40 K, 50 K (yellow curve), 70 K, 100 K, 150 K, and 300 K (red curve). Panel (a) shows the longitudinal resistivity ρ_{xx}, panel (b) the Hall resistivity ρ_{xy} and panel (c) the sheet electron density n_s extracted from the linear slope of ρ_{xy} at $B = 0$ as a function of temperature. Adapted from Ref. [30].

detailed magnetotransport studies.

Longitudinal and Hall resistivities were extracted directly from Hall bar measurements or calculated from data obtained on van der Pauw samples using the permutation method. The transport studies demonstrate that all samples show a rather similar magnetotransport behavior which seems to be mostly unaffected by the presence of band inversions and the type of interfaces. A typical example of this behavior is presented in Fig. 19 which shows longitudinal and Hall resistivities as well as extracted carrier densities for a Hall bar sample made of wafer #A for different temperatures. At low temperatures, all samples exhibit a strong, positive longitudinal magnetoresistance (see Fig. 19 (a)) and a nonlinear Hall resistance (see Fig. 19 (b)). For small magnetic fields, the Hall slope corresponds to negatively charged carriers, i.e. electrons, while at high magnetic fields, the slope changes to a hole-like one (not shown). This indicates that the hole density slightly exceeds the electron density, whereas electrons exhibit a significantly higher mobility in these structures [94]. The sheet carrier densities and mobilities were extracted from the transport data with a classical two-component Drude model which has been applied successfully for HgTe quantum wells before [19, 95, 96]. Additionally, a simpler single-component Drude model was used that approximates the effective sheet carrier density from the linear slope of the Hall resistivity ρ_{xy} at small magnetic fields. Table 2 displays the values of the sheet electron densities n_s as well as the average volume electron densities n for all investigated samples. The latter were calculated from the respective sheet electron densi-

sample	Cd content, x	band structure	top interface	n_s ($10^{11}\,cm^{-2}$)	n ($10^{14}\,cm^{-3}$)
#A	0.151	inverted	smooth	2.9	4.8
#B	0.150	inverted	smooth	2.2	3.7
#C	0.151	inverted	sharp	3.3	6.7
#D	0.179	normal	smooth	4.2	4.2
#E	0.223	normal	smooth	2.4	1.9

Table 2: Overview of the basic parameters of the investigated $Cd_xHg_{1-x}Te$ films, including the cadmium content x, the corresponding band ordering in the flat region, the type of top interface between the flat region and the cap layer, as well as the sheet electron densities n_s and the volume electron densities n obtained from low-frequency magnetotransport measurements at $T = 4.2\,K$.

ties via $n = n_s/w$, where w is the corresponding thickness of the $Cd_xHg_{1-x}Te$ film extracted from Fig. 18. At low temperatures, the sheet electron densities n_s are rather small and lie in the range of $2 \cdot 10^{11}\,cm^{-2}$ to $4 \cdot 10^{11}\,cm^{-2}$ in all samples, while the sheet hole densities are slightly larger than that. Both electron and hole densities increase for higher temperatures up to an electron sheet density in the range of $2 \cdot 10^{12}\,cm^{-2}$ to $3 \cdot 10^{12}\,cm^{-2}$ at 77 K and between $3 \cdot 10^{13}\,cm^{-2}$ to $1.2 \cdot 10^{14}\,cm^{-2}$ at 300 K.

sample number	QW width, d (nm)	geometry	substrate orientation	n_s (10^{11} cm^{-2})	μ (10^4 cm^2/Vs)	size (mm)
#1	20	gated Hall bar	(001)	1 to 7	17 to 50	$l = 0.25$, $w = 0.05$
#2	20	Hall bar	(013)	8.2	15	$l = 0.25$, $w = 0.05$
#3	8	Hall bar	(013)	7.5	6.7	$l = 0.25$, $w = 0.05$
#4	6.6	Corbino	(013)	12	4.4	$r_i = 0.36$, $r_o = 1.9$
#5	6.5	Corbino	(013)	9.7	11	$r_i = 0.25$, $r_o = 1.9$
#6	6.5	Hall bar	(013)	10	13	$l = 0.25$, $w = 0.05$
#7	5	Corbino	(013)	4.0	0.14	$r_i = 0.32$, $r_o = 1.2$

Table 3: Specifications and parameters of the HgTe quantum well samples. Electron densities and mobilities were extracted from dark magnetotransport measurements performed at $T = 4.2$ K for samples #2 to #7 and $T = 2$ K for sample #1. Please note that the actual mobilities in samples with Corbino disk geometry may be slightly larger than the values given in the table. This is due to the inevitable contribution of the contact resistance in the corresponding two-point measurements. The ranges of densities and mobilities given for gated sample #1 correspond to the values within the gate voltage range of 2 V to 10 V, as shown in Figs. 28 (b) and (c).

5 Sign-alternating terahertz photoconductivity in HgTe quantum wells

This chapter is devoted to the terahertz photoconductivity in HgTe quantum wells with normal and inverted parabolic band structures as well as in QWs with linear dispersion. It will be demonstrated that the application of an out-of-plane magnetic field results in a systematic change of the sign of photoconductivity. In the following, the characteristics of this sign-alternating photoconductivity are presented for different QW widths and sample geometries. Subsequently, the origin of the sign inversion is discussed within the framework of μ-photoconductivity.

5.1 Experimental results

By illumination with modulated terahertz radiation from a continuous wave molecular gas laser, the photoconductive response was investigated in HgTe quantum wells with various widths corresponding to the topologically trivial and non-trivial regimes. Surprisingly, the application of a magnetic field oriented normally to the QW plane resulted in a systematic change of the sign of the photoconductive signal in both regimes. In Corbino disk samples, a sweep of the magnetic field strength revealed two sign inversions at low applied fields. Figure 20 demonstrates this magnetic field dependence of the photoconductivity exemplarily for Corbino disk sample #5. This sample hosts a HgTe quantum well with $d = 6.5\,\mathrm{nm}$ close to critical thickness and is consequently characterized by an almost linear bulk band dispersion [21, 97]. The data presented in Fig. 20 were obtained at liquid helium temperature for excitation of the sample with right-handed circularly polarized terahertz radiation at different frequencies $f = 2.54\,\mathrm{THz}$, $1.63\,\mathrm{THz}$ and $0.69\,\mathrm{THz}$ using a two-terminal setup. At low fields, the photoconductivity $\Delta\sigma_{xx}$ normalized to the incident radiation intensity I_R manifests two distinct sign inversions at $\pm B_\mathrm{inv}$ and $\pm B^*_\mathrm{inv}$ symmetrically around $B = 0$. At higher fields, $1/B$-periodic oscillations with a period corresponding to Shubnikov-de Haas oscillations set in. These high-field quantum oscillations will be discussed in detail later. Let us first focus on the double sign inversion which, in contrast, is detected at substantially lower fields.

Notably, the two inversion fields B_inv and B^*_inv exhibit a different frequency

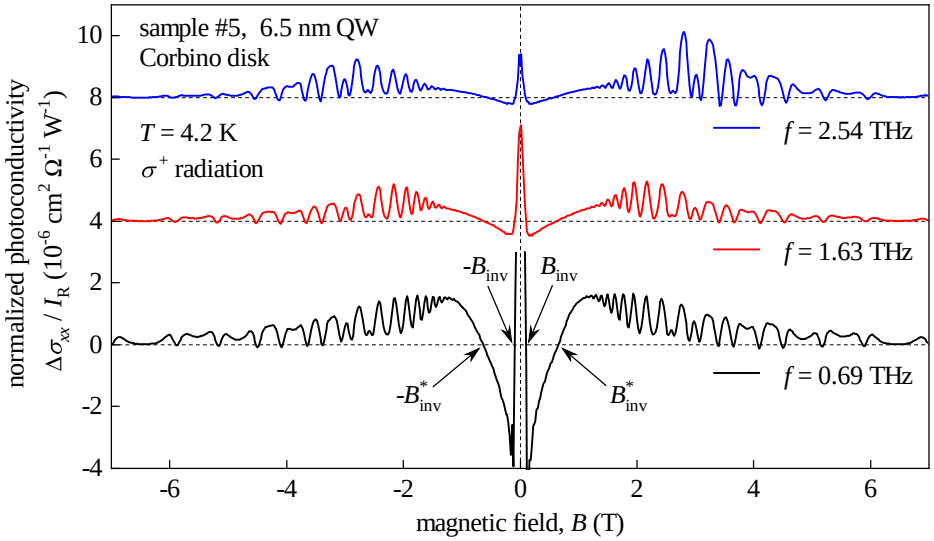

Figure 20: Photoconductivity $\Delta\sigma_{xx}$ normalized to the incident radiation intensity I_R with respect to magnetic field. The data are obtained at $T = 4.2\,\mathrm{K}$ on Corbino disk sample #5 which hosts a QW with $d = 6.5\,\mathrm{nm}$. The sample was illuminated by a right-handed circularly polarized (σ^+ polarized) THz laser beam with frequencies $f = 2.54\,\mathrm{THz}$, $1.63\,\mathrm{THz}$, and $0.69\,\mathrm{THz}$, corresponding to the blue, red, and black traces, respectively. Note that the upper curves are shifted vertically by $4 \cdot 10^{-6}\,\mathrm{cm^2\,\Omega^{-1}\,W^{-1}}$ each and that the low-field values were omitted for the black curve for clarity. The photoconductivity changes sign at magnetic fields $B = \pm B_\mathrm{inv}$ and $B = \pm B^*_\mathrm{inv}$ as highlighted by black arrows for the lowest curve. Adapted from Ref. [23].

dependence. While the first inversion at B_inv is found to be independent of the photon energy, the second inversion at B^*_inv shifts to slightly smaller magnetic fields for higher photon energies, see Fig. 21 (a) and (b). Figure 21 (a) presents the photoconductivity data for all frequencies normalized to the respective photoconductivity $\Delta\sigma_{xx}\,(B = 0)$ at zero magnetic field. These zero-field values accurately follow the expected frequency dependence for μ-photoconductivity, as demonstrated in Fig. 21 (c). Note that in the model of free carrier heating, the photoconductivity is proportional to the classical radiation absorption given by the Drude-Lorentz formula $\Delta\sigma_{xx} \propto (1 + \omega^2\tau^2)^{-1}$ [56] (red dashed line in Fig. 21 (c)), in accordance with the experimental findings. Additionally, the bolometric response is expected to decrease for higher temperatures. This was confirmed in the experiment, where a drastic suppression of the normalized zero-field photoconductivity $\Delta\sigma_{xx}(B = 0)/I_\mathrm{R}$ has been detected at higher temperatures, as shown in Fig. 21 (d).

In strong contrast to the Corbino disk geometry, only a single sign inversion was observed in the low-field photoresponse of Hall bar samples. To directly compare the influence of the sample geometry, Hall bar sample #6 was fabricated

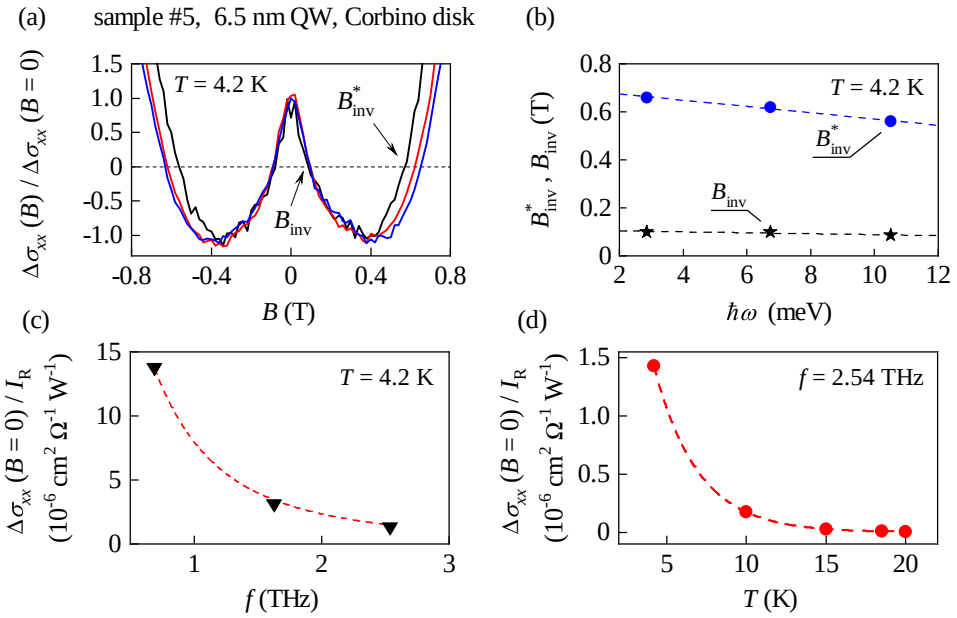

Figure 21: Panel (a) presents a zoom of the low-field part of the photoconductivity data shown in Fig. 20. All three curves obtained at $f = 2.54\,\mathrm{THz}$ (blue trace), 1.63 THz (red trace), and 0.69 THz (black trace) are normalized to the respective photoconductivity $\Delta\sigma_{xx}(B = 0)$ at zero field. Panel (b) displays the extracted magnetic field values B_{inv} and B^*_{inv} for the first and second photoconductivity sign inversion, respectively, plotted against the photon energy $\hbar\omega$. Panel (c) shows the zero-field photoconductivity $\Delta\sigma_{xx}(B = 0)/I_{\mathrm{R}}$ (black triangles) from the data set presented in Fig. 20 with respect to radiation frequency. The red dashed line presents a fit according to $\Delta\sigma_{xx} \propto (1 + \omega^2\tau^2)^{-1}$. Panel (d) features the temperature dependence of the zero-field photoconductivity $\Delta\sigma_{xx}(B = 0)/I_{\mathrm{R}}$ measured on sample #5 at $f = 2.54\,\mathrm{THz}$ (red circles). Here, the red dashed line is a guide for the eye. Adapted from Ref. [23].

from the same wafer as Corbino sample #5 with $d = 6.5\,\mathrm{nm}$. The corresponding 4-terminal-photoresistivity data of Hall bar sample #6 obtained by illumination with a linearly polarized laser beam with $f = 2.54\,\mathrm{THz}$ is presented in Fig. 22. Note that in Hall bar geometry one measures the photoresistivity, i.e. the radiation-induced change $\Delta\rho_{xx}$ of the longitudinal resistivity ρ_{xx}, rather than the photoconductivity $\Delta\sigma_{xx}$ which can be directly extracted from measurements in Corbino disk geometry. For both quantities, the extracted sign inversion magnetic fields are directly comparable with each other since $\Delta\sigma_{xx} = 0$ also yields $\Delta\rho_{xx} = 0$ and vice versa. However, it is important to note that photoresistivity $\Delta\rho_{xx}$ and photoconductivity $\Delta\sigma_{xx}$ consistently have opposite signs at $B = 0$. The Hall bar photoresistivity shown in Fig. 22 (a) is negative at small magnetic fields, and subsequently changes sign at $\pm B^*_{\mathrm{inv}}$(Hall bar). These fields coincide with the inversion fields $\pm B^*_{\mathrm{inv}}$(Corbino) obtained in the corresponding Corbino disk sample under the same conditions. A detailed

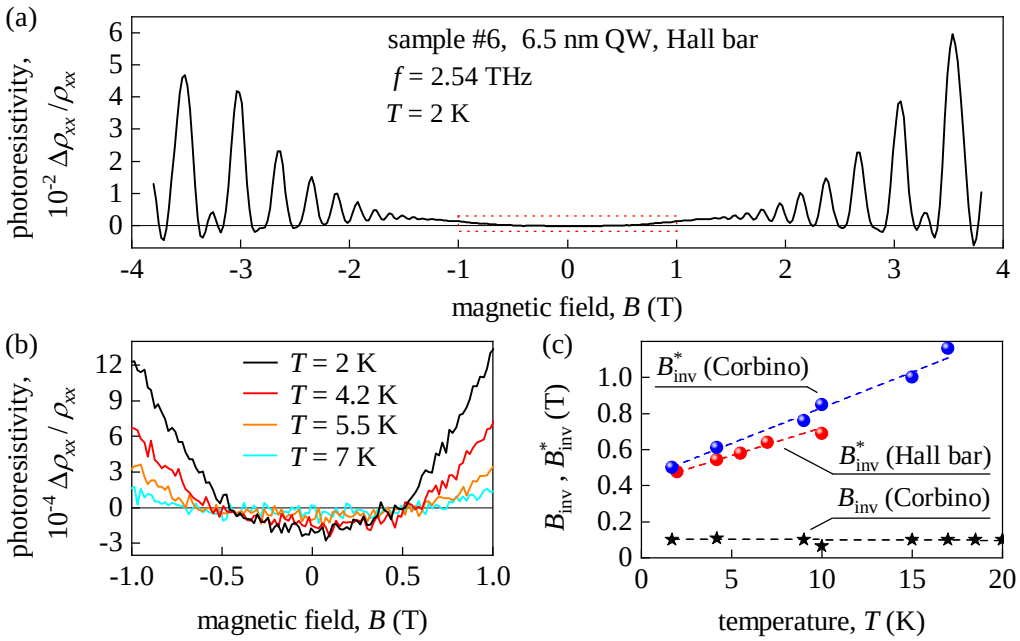

Figure 22: Magnetic field dependence of the photoresistivity $\Delta\rho_{xx}$ normalized to the respective dark resistivity ρ_{xx} obtained in Hall bar sample #6 ($d = 6.5\,\mathrm{nm}$). The data were recorded while the sample was illuminated with modulated linearly polarized terahertz radiation with frequency $f = 2.54\,\mathrm{THz}$ and intensity $I_\mathrm{R} = 1.2\,\mathrm{W/cm^2}$. Panel (a) presents the curve obtained at $T = 2\,\mathrm{K}$ in the full range of magnetic fields, whereas panel (b) shows a zoom of the low-field part, highlighted by the red dashed box in (a), for different temperatures $T = 2\,\mathrm{K}$, $4.2\,\mathrm{K}$, $5.5\,\mathrm{K}$ and $7\,\mathrm{K}$. Panel (c) illustrates the temperature dependence of the Hall bar inversion fields B^*_inv(Hall bar) extracted from panel (b) as well as the first and second inversion fields B_inv(Corbino) and B^*_inv(Corbino) detected in Corbino disk sample #5. The dashed lines are linear fits to the data points. Adapted from Ref. [23].

analysis of the temperature dependence of the inversion fields in both Hall bar and Corbino disk geometries presented in Fig. 22 (c) reveals that the inversion field B^*_inv increases with rising temperatures. Furthermore, the temperature dependence of B^*_inv is strikingly similar in both geometries. In contrast, the first inversion point B_inv, which is observed in photoconductivity only, shows no measurable dependence on temperature. This results clearly point towards the conclusion that the origin of the sign inversion at B^*_inv is the same in both sample geometries. On the other hand, the sign inversion at B_inv, which is independent of temperature and radiation frequency, seems to be characteristic for the photoconductivity measured in Corbino disk geometry.

Analogue behavior was also observed in other investigated samples with different quantum well widths. Figures 23 (a) and (b) present photoresistivity data obtained under similar conditions ($f = 2.54\,\mathrm{THz}$ and $T = 4.2\,\mathrm{K}$) on Hall

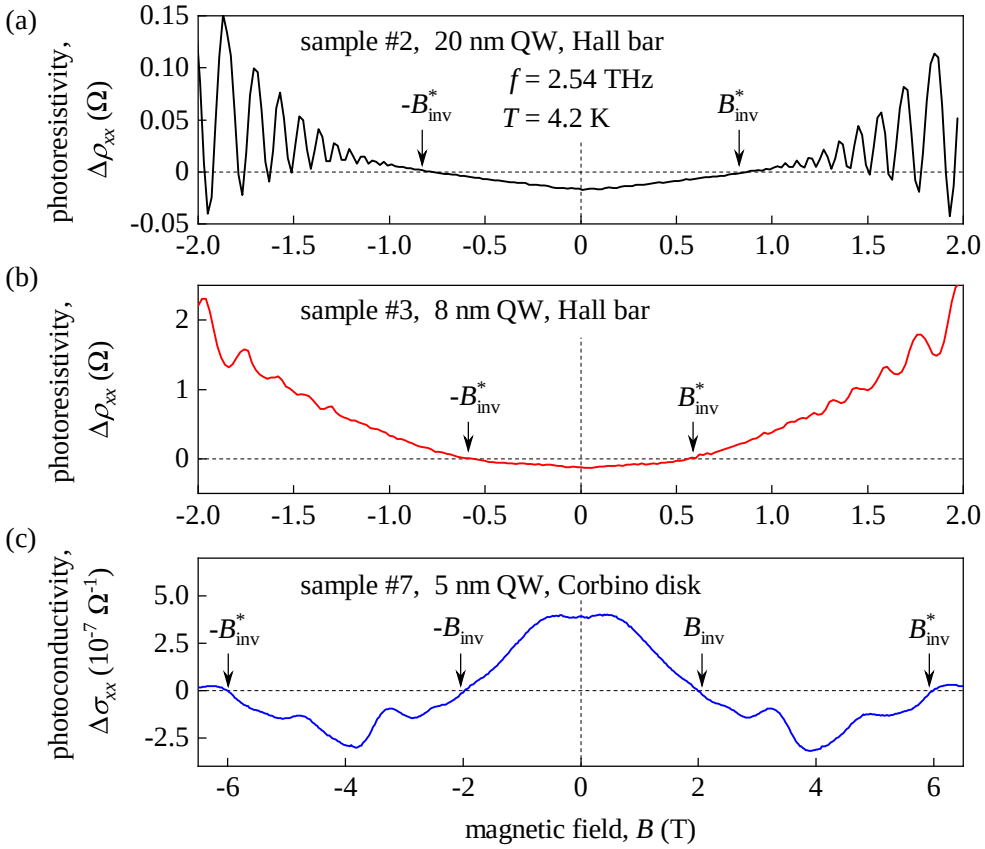

Figure 23: Magnetic field dependence of the photoresponse in samples #2, #3, and #7 measured at $T = 4.2\,\mathrm{K}$ under incidence of linearly polarized radiation with frequency $f = 2.54\,\mathrm{THz}$ and intensity $I_\mathrm{R} \simeq 0.7\,\mathrm{W/cm^2}$. Panels (a) and (b) present the photoresistivity $\Delta\rho_{xx}$ in Hall bar samples #2 ($d = 20\,\mathrm{nm}$) and #3 ($d = 8\,\mathrm{nm}$), whereas panel (c) shows the photoconductivity $\Delta\sigma_{xx}$ in Corbino disk sample #7 ($d = 5\,\mathrm{nm}$). Adapted from Ref. [23].

bar samples #2 ($d = 20\,\mathrm{nm}$) and #3 ($d = 8\,\mathrm{nm}$), both corresponding to the regime of inverted band ordering. In both cases, the photoresistivity exhibits a similar magnetic field dependence with negative $\Delta\rho_{xx}$ at zero field, a sign inversion at B^*_inv, and $1/B$-periodic oscillations at higher fields. Furthermore, the photoconductivity measured in Corbino disk samples with different QW widths exhibits a qualitatively similar behavior as described for sample #5, featuring two sign inversions in magnetic field. This is shown in Fig. 24 (b) for sample #4 with $d = 6.6\,\mathrm{nm}$ and in Fig. 23 (c) for sample #7 with a QW width of $d = 5\,\mathrm{nm}$. The only significant difference between data obtained for different QW widths is the position of the inversion fields B_inv and B^*_inv. Especially for sample #7, which exhibits the lowest carrier mobility, the inversion field B_inv is significantly higher than in other samples.

To gain a better understanding of the high-field photoconductivity which performs $1/B$-periodic oscillations, supporting dark magnetotransport measure-

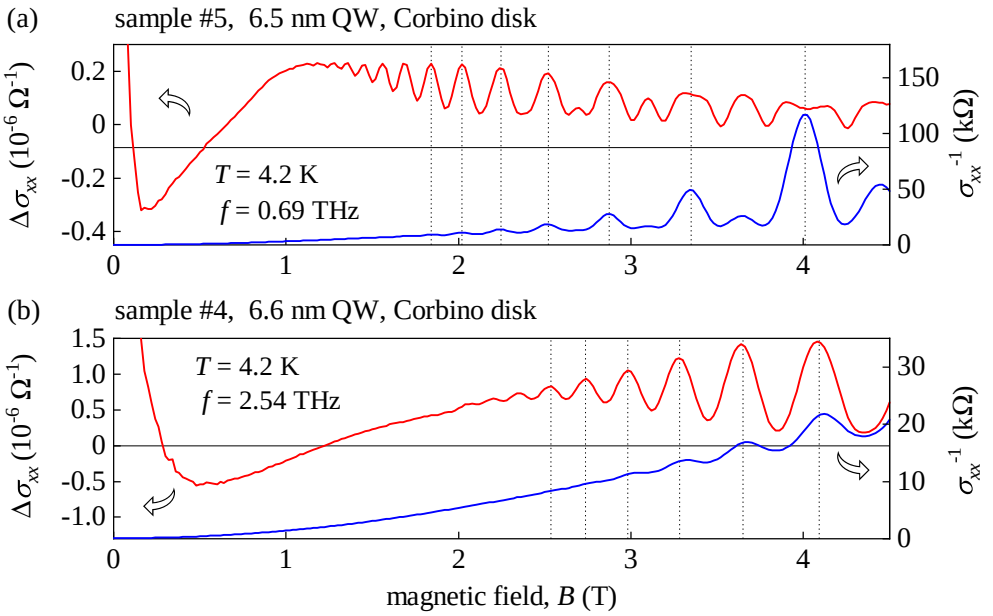

Figure 24: Comparison of the terahertz photoconductivity $\Delta\sigma_{xx}$ with the reciprocal dark conductivity σ_{xx}^{-1} at $T = 4.2\,\mathrm{K}$ for Corbino disk samples #5 (a) and #4 (b). In panel (a), the photoconductivity in sample #5 is obtained for radiation with $f = 0.69\,\mathrm{THz}$ and $I_\mathrm{R} = 0.14\,\mathrm{W/cm^2}$, whereas panel (b) includes photoconductivity data for sample #4 measured at $f = 2.54\,\mathrm{THz}$ and $I_\mathrm{R} = 1\,\mathrm{W/cm^2}$. Adapted from Ref. [23].

ments were carried out without THz irradiation. Figures 24 (a) and (b) present a comparison between the inverse dark conductivity σ_{xx}^{-1} and the photoconductivity $\Delta\sigma_{xx}$ in the two Corbino disk samples #5 ($d = 6.5\,\mathrm{nm}$) and #4 ($d = 6.6\,\mathrm{nm}$), respectively. The data clearly demonstrate that the photoconductivity oscillations at higher magnetic fields coincide with the Shubnikov-de Haas (SdH) oscillations observed in dark magnetotransport. Such a behavior, that has also been detected in all other QW samples, is typical for photoconductivity resulting from free carrier heating. Here, the terahertz radiation-induced electron heating leads to a thermal suppression of the amplitude of SdH oscillations [20]. Note that for samples #5 and #6 (both with a QW width $d = 6.5\,\mathrm{nm}$ close to the critical one) the shape of the SdH oscillations becomes more complicated at higher fields $B \gtrsim 2.5\,\mathrm{T}$ (see e.g. Fig. 24 (a) or Fig. 27 (a)) because both cyclotron and spin gaps in the density of states are resolved. This manifests also in the photoconductivity traces which exhibit additional extrema, see e.g. Fig. 24 (a).

Further analysis of the photoconductivity signals obtained for different radiation frequencies shows that for high photon energies, the former are substantially enhanced at the positions of CR, as e.g. shown in Fig. 25 (a). Here, the photoconductivity obtained at $f = 2.54\,\mathrm{THz}$ in Corbino disk sample #5

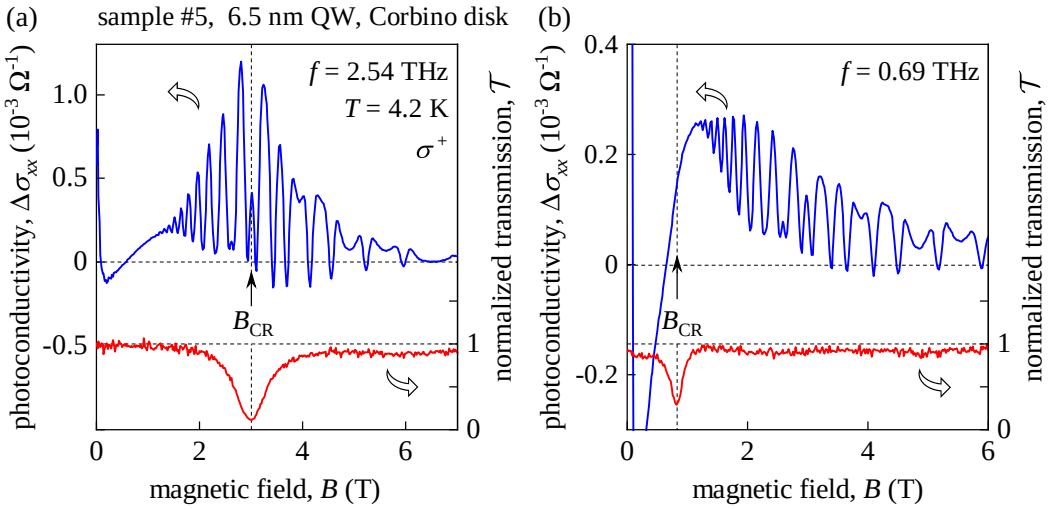

Figure 25: Comparison of magnetic field dependences of the photoconductivity $\Delta\sigma_{xx}$ and radiation transmission $\mathcal{T}$ for Corbino disk sample #5 at $T = 4.2\,\mathrm{K}$. The curves presented in panel (a) were obtained by illuminating the sample with a right-handed circularly polarized laser beam with $f = 2.54\,\mathrm{THz}$ and $I_\mathrm{R} = 0.3\,\mathrm{W/cm^2}$, whereas panel (b) shows data for $f = 0.69\,\mathrm{THz}$ and $I_\mathrm{R} = 0.2\,\mathrm{W/cm^2}$. Vertical dashed lines mark the positions of B_CR extracted from the magnetotransmission curves (in panel (a): $B_\mathrm{CR} = 3.0\,\mathrm{T}$, in panel (b): $B_\mathrm{CR} = 0.82\,\mathrm{T}$). Adapted from Ref. [23].

is shown with respect to magnetic field alongside the simultaneously recorded radiation transmission from which the corresponding CR magnetic fields B_CR were extracted. Such resonant enhancement is in accordance with previous studies of the terahertz photoresponse in HgTe QWs under conditions of CR [20]. Surprisingly, in the present experiments, no cyclotron-resonant increase of the photoresponse magnitude is present at the lowest radiation frequency $f = 0.69\,\mathrm{THz}$, as displayed in Fig. 25 (b). In this case, the position of CR lies below the onset of SdH oscillations and the photoconductivity is completely featureless at B_CR.

To summarize, a sign-alternating photoconductive/photoresistive response was found in HgTe QW samples with different energy dispersions and geometries. In Corbino disk samples, two sign inversions at magnetic fields B_inv and B^*_inv were systematically observed, whereas in Hall bar samples only the inversion at B^*_inv was detected.

5.2 Discussion

At first, the sign inversion at B_inv, characteristic for the Corbino disk geometry, is discussed. In the previous chapter, it was shown that the inversion field B_inv

is independent of temperature as well as photon energy, see Figs. 22 (c) and 21 (b). Intriguingly, such a sign inversion of the photoconductivity is expected to necessarily occur in Corbino disk samples within the semiclassical Drude description of the electron bolometric effect as a result of the transition from classically weak to classically strong magnetic fields at $\omega_c\tau = 1$. According to the Drude model, the conductivity

$$\sigma_{xx} \propto \frac{\tau}{(1+\omega_c^2\tau^2)} \tag{55}$$

is proportional to the transport scattering time τ in the parametric region of classically weak magnetic fields ($\omega_c \ll 1/\tau$), whereas in the opposite limit $\omega_c \gg 1/\tau$ the conductivity is proportional to $1/\tau$. Assuming a bolometric mechanism, i.e. the incident terahertz radiation field modifies τ due to heating of the charge carriers, the sign of photoconductivity is indeed opposite in these two magnetic field regions. Within this model, the inversion field B_{inv} is therefore given by

$$B_{\mathrm{inv}} = \frac{m^*}{e\tau} = \frac{1}{\mu} \, . \tag{56}$$

This relation has been checked by extraction of the transport scattering time τ and mobility μ from dark magnetotransport measurements and calculation of the cyclotron mass m_{CR} from B_{CR} detected in magnetotransmission experiments. In fact, it is possible to correctly reproduce the inversion field B_{inv} from these extracted parameters, which demonstrates the bolometric nature of the observed low-field photoconductivity. Note that due to a possible influence of the contact resistance in two-terminal magnetotransport measurements in Corbino disk geometry, the transport parameters obtained on corresponding Hall bar samples made from the same wafer were used, if available, to achieve higher accuracy. Moreover, the bolometric origin is also supported by the temperature and frequency independence of B_{inv} detected in the experiment. Indeed, within the mechanism of μ-photoconductivity, the position of the inversion field B_{inv} is expected to be independent of temperature and radiation frequency, since a change in frequency only modifies the magnitude of heating. The independence of temperature holds true as long as the terahertz-induced variation of τ due to heating remains small. It is important to note that the sign inversion at B_{inv} allows to directly calculate the carrier mobility according to Eq. (56). This provides a powerful optoelectronic method to measure the

carrier mobility in such systems.

While the inversion of the photoconductivity at B_{inv} can be well understood within the model of carrier heating, the absolute sign of the photosignal for $B < B_{\mathrm{inv}}$ and $B > B_{\mathrm{inv}}$ is contrary to what one would expect. Within the temperature range used in the experiments, typically electron-phonon scattering is the dominant contribution to momentum relaxation. Therefore, electron gas heating should result in a reduction of the scattering time τ, i.e. $\mathrm{d}\tau(T)/\mathrm{d}T < 0$ [56]. As a consequence, the conductivity σ_{xx} in Corbino disk geometry should decrease due to incident terahertz radiation for $|B| < B_{\mathrm{inv}}$, resulting in a negative photoconductivity $\Delta\sigma_{xx}$, and increase for $|B| > B_{\mathrm{inv}}$ (i.e. positive photoconductivity). Contrary to that, in the experiment, positive photoconductivity has been observed for $|B| < B_{\mathrm{inv}}$, that changes to negative photoconductivity for $|B| > B_{\mathrm{inv}}$. This implies that here the radiation-induced heating causes an increase of the transport scattering time, i.e. $\mathrm{d}\tau(T)/\mathrm{d}T > 0$, at $B \lesssim B_{\mathrm{inv}}$.

Now, the discussion of the results within the framework of electron gas heating is extended to the photoresistivity obtained on Hall bar samples. Within the Drude model, the classical longitudinal resistivity ρ_{xx} is proportional to the momentum relaxation rate $1/\tau$ for both classically weak as well as classically strong magnetic fields. Therefore, generally no sign inversion of the photoresistivity is expected in Hall bar geometry, in particular not at B_{inv}. The sign of the photoresistivity should simply reflect the temperature dependence of the scattering time τ. In accordance with the results obtained on Corbino disk samples, the photoresistivity in Hall bar samples is expected to be negative in the region of small magnetic fields including $B = 0$ and $B = B_{\mathrm{inv}}$. Indeed, this is fully consistent with the experimental data, see e.g. Figs. 22 and 23. In turn, this also implies that the sign inversion at B^*_{inv}, where both photoconductivity and photoresistivity change sign, may originate from the temperature dependence of the scattering time τ. Indeed, it could be interpreted as the transition point to a more conventional temperature dependence of τ at $|B| > B^*_{\mathrm{inv}}$, where the terahertz radiation-induced heating reduces the scattering time (i.e. $\mathrm{d}\tau(T)/\mathrm{d}T < 0$) due to more pronounced electron-phonon scattering.

It is important to mention that the high-field inversion at B^*_{inv} lies well within the region of classically strong magnetic fields ($\omega_{\mathrm{c}} \gg 1/\tau$), where $\rho_{xx} \ll \rho_{xy}$, i.e. the longitudinal resistivity ρ_{xx} exceeds the Hall resistivity $\rho_{xy} \simeq eB/n$. Thus, the longitudinal conductivity σ_{xx} is given by $\sigma_{xx} \simeq \rho_{xx}/\rho^2_{xy}$. As a conse-

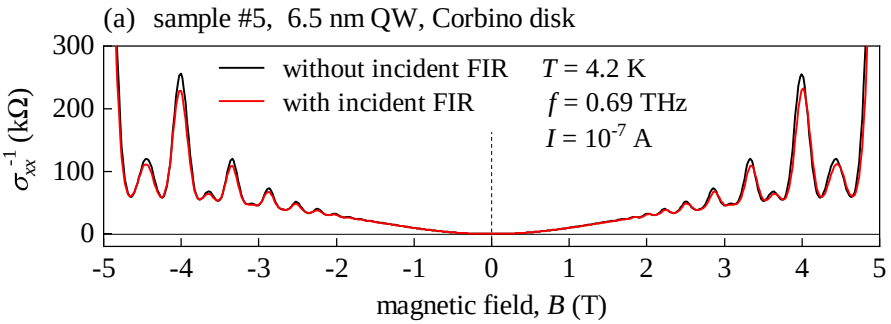

Figure 26: Comparison of the inverse dark conductivity σ_{xx}^{-1} (black curve) of Corbino disk sample #5 with σ_{xx}^{-1} obtained under continuous irradiation with non-modulated terahertz radiation (red curve) with frequency $f = 0.69\,\mathrm{THz}$ and intensity $I_\mathrm{R} = 0.27\,\mathrm{W/cm^2}$. The data were obtained at $T = 4.2\,\mathrm{K}$ with an applied driving current of $I = 100\,\mathrm{nA}$. Adapted from Ref. [23].

quence, the behavior and sign of the photoconductivity $\Delta\sigma_{xx}$ and photoresistivity $\Delta\rho_{xx}$ is expected to be the same in the vicinity of B^*_inv, assuming that the electron density n is not influenced by the incident terahertz radiation. This is in perfect agreement with the experimental data, see e.g. Figs. 20 and 23, where both the photoconductivity in Corbino disk geometry and photoresistivity in Hall bar geometry change from negative to positive at B^*_inv. A deeper analysis of the Shubnikov-de Haas oscillations reveals that their period is almost unaffected by the incident terahertz radiation (see Fig. 26) or a variation of the temperature (see Fig. 27). This demonstrates that the electron density is only very weakly sensitive to temperature and terahertz irradiation in conditions of the experiments. When comparing photoconductivity and photoresistivity, it is worth mentioning that the visibility of features is enhanced in photoconductivity within the parametric region $|B| \gtrsim B^*_\mathrm{inv}$. This is because of the large scaling factor $\Delta\sigma_{xx} \propto \rho_{xy}^{-2} \propto B^{-2}$. Indeed, this is in accordance with the experimental data. On the other hand, the fact that for low excitation frequencies, no enhanced cyclotron-resonant photoresponse was detected (see Fig. 25 (b)) remains unclear and requires further study.

As suggested above, the observation of the sign-alternating photoresponse in the experiment is consistent with the model of μ-photoconductivity, assuming that the sign inversion at B^*_inv originates from an unconventional temperature behavior of the momentum scattering time τ, which increases with rising temperature for $|B| < B^*_\mathrm{inv}$ and decreases with temperature for $|B| > B^*_\mathrm{inv}$. To probe the temperature dependence of τ, supporting four-terminal dark magnetotransport measurements were carried out on Hall bar sample #6 at different temperatures. The results are presented in Fig. 27. At first glance, the longi-

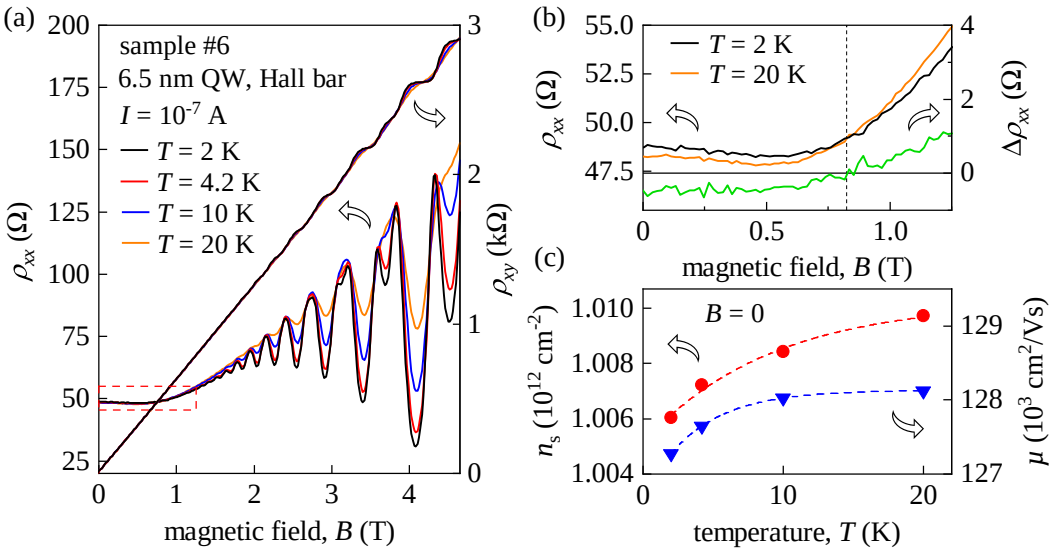

Figure 27: Magnetotransport data for sample #6 with Hall bar geometry and QW width $d = 6.5$ nm. Panel (a) features longitudinal ρ_{xx} (left axis) and Hall magnetoresistivity ρ_{xy} (right axis) for a driving current $I = 100$ nA at $T = 2$ K (black trace), 4.2 K (red trace), 10 K (blue trace), and 20 K (orange trace). Panel (b) shows a zoom of the data presented in panel (a) around the low-field region highlighted by the red dashed box. The green curve corresponding to the right axis indicates the difference $\Delta\rho_{xx} = \rho_{xx}(20\,\mathrm{K}) - \rho_{xx}(2\,\mathrm{K})$ of the longitudinal resistance obtained at 20 K and 2 K. The black dashed line highlights the sign inversion of $\Delta\rho_{xx}$. In panel (c), extracted values of the carrier density n_s and mobility μ at zero magnetic field are plotted against temperature. Adapted from Ref. [23].

tudinal resistance ρ_{xx} appears to be only weakly dependent on temperature in the relevant classical range of magnetic fields before the onset of Shubnikov-de Haas oscillations (see Fig. 27 (a)). Actually, this is in line with the fact that the longitudinal resistance $\rho_{xx} \propto 1/\tau$ is only sensitive to the temperature variation of the momentum scattering rate $1/\tau$ in the regime of classical fields, whereas the amplitude of the SdH oscillations at higher fields is governed by an additional, in this case, much stronger exponential temperature-dependent factor [98]. However, a closer look (see. Fig. 27 (b)) reveals that the temperature dependence of the longitudinal resistivity ρ_{xx} indeed changes from $\mathrm{d}\rho_{xx}/\mathrm{d}T < 0$ for small magnetic fields to $\mathrm{d}\rho_{xx}/\mathrm{d}T > 0$ for higher fields at around 0.8 T. This is highlighted by the green curve in Fig. 27 (b) which presents the difference of the longitudinal resistivities obtained at 20 K and 2 K. Furthermore, the temperature dependence of the carrier mobility at zero field extracted from the dark magnetotransport measurements (see Fig. 27 (c)) clearly demonstrates that at $B = 0$, the mobility $\mu \propto \tau$ slightly increases with temperature. This, indeed, confirms the temperature behavior of the momentum relaxation rate

$1/\tau$ that was suggested from the shape of the photoresponse. It decreases with temperature for $B \lesssim 0.8\,\mathrm{T}$ and increases for $B \gtrsim 0.8\,\mathrm{T}$. In fact, this value agrees reasonably well with the inversion field B^{*}_{inv} detected in Corbino disk sample #5 and Hall bar sample #6. Here, it is important to bear in mind that μ-photoconductivity generally measures the sensitivity of the transport properties to the electron temperature T_{e} under non-equilibrium conditions, where T_{e} is larger than the lattice temperature T_{l} due to radiation-induced carrier heating. Temperature-dependent dark magnetotransport, however, yields information on the temperature evolution of the scattering time τ only in conditions where electrons and lattice are in thermal equilibrium, i.e. $T_{\mathrm{e}} = T_{\mathrm{l}}$. This may explain the slight variation of the inversion fields, where $\mathrm{d}\tau/\mathrm{d}T$ changes from positive to negative, detected in photoresistivity and dark magnetotransport. All together, this provides a strong support to the bolometric interpretation of the sign-alternating photoresponse presented above.

6 Terahertz-induced resistance oscillations in HgTe quantum wells

While the previous chapter was centered on the description of the sign-alternating photoconductivity observed in QWs with moderate carrier mobilities, this chapter addresses the photoconductivity in a gated 20 nm QW with significantly higher mobility. Besides the SdH-like oscillations at higher magnetic fields, the measurements reveal additional $1/B$-periodic oscillations in the terahertz photoresponse at considerably low magnetic fields. These oscillations are presented for different applied gate voltages and afterwards discussed within the framework of photo-assisted transitions between disorder-broadened Landau levels.

6.1 Experimental results

Upon irradiation with the terahertz electric field, an oscillatory photoresponse was observed in sample #1 for small magnetic fields applied normally to the QW plane, as shown in Fig. 28 (a). This Hall bar sample hosts a 20 nm wide HgTe quantum well and is additionally equipped with a semitransparent top gate structure which allows to tune the Fermi energy. For positive applied gate voltages, a mobility up to $5 \cdot 10^5\,\mathrm{cm^2/(V\,s)}$ is achieved, which exceeds the mobility of all other investigated QW samples, see Tab. 3. The data presented in Fig. 28 (a) were obtained for different applied gate voltages at a temperature $T = 2\,\mathrm{K}$, using linearly polarized radiation with frequency $f = 0.69\,\mathrm{THz}$. Analysis of the magnetic field dependences reveals that the nodes of the oscillatory photoresistivity coincide with the position of cyclotron resonance at B_{CR} and its second harmonic $B_{\mathrm{CR}}/2$, as illustrated by the dashed vertical lines in Fig. 28 (a). This demonstrates that the oscillations are caused by an interplay between the photon energy $\hbar\omega$ and the cyclotron energy $\hbar\omega_{\mathrm{c}}$, a phenomenon known as microwave-induced resistance oscillations (MIRO). Such oscillations exhibit a distinctive $\omega/\omega_{\mathrm{c}}$-periodicity with nodes at harmonics of the cyclotron resonance and minima and maxima shifted away from integer $\omega/\omega_{\mathrm{c}}$ by a quarter cycle [99]. This is in full agreement with the experimental data. Note that for excitation frequencies in the terahertz range, this effect is often referred to as terahertz-induced resistance oscillations (TIRO), describing a high-frequency MIRO analogue. For low applied driving currents $I \lesssim 1\,\mu\mathrm{A}$,

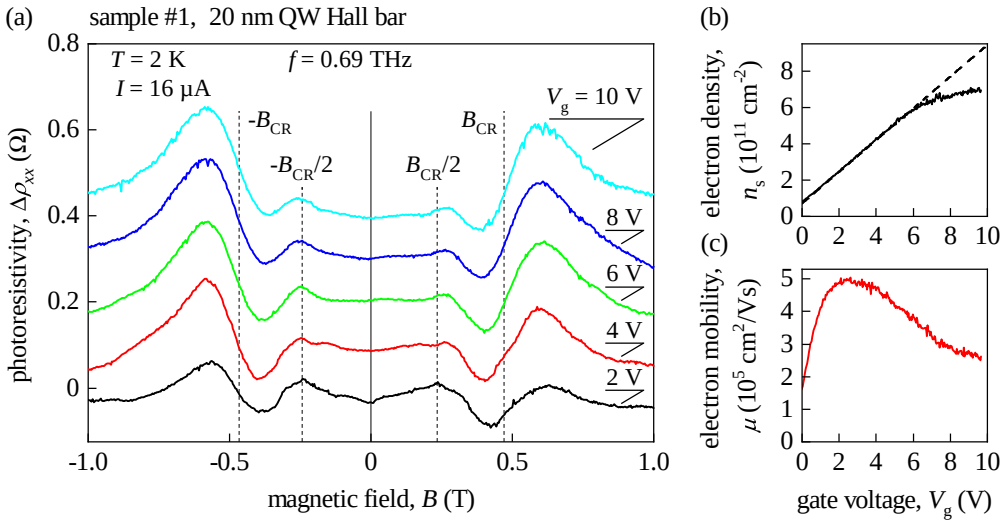

Figure 28: Panel (a) displays the magnetic field dependence of the photoresistivity $\Delta\rho_{xx}$ measured at $T = 2\,\mathrm{K}$ in Hall bar sample #1 which hosts a quantum well with $d = 20\,\mathrm{nm}$. The data were measured with the double modulation technique using an applied alternating current $I = 16\,\mu\mathrm{A}$ and a linearly polarized radiation field with frequency $f = 0.69\,\mathrm{THz}$ and intensity $I_\mathrm{R} = 0.2\,\mathrm{W/cm^2}$. Curves obtained at different gate voltages in the range between $V_\mathrm{g} = 2\,\mathrm{V}$ and $10\,\mathrm{V}$ are vertically offset from each other by $0.1\,\Omega$ for clarity. The vertical dashed lines correspond to the CR magnetic field $B_\mathrm{CR} = 0.47\,\mathrm{T}$ and its second harmonic $B_\mathrm{CR}/2$ extracted from radiation transmission measurements. Panels (b) and (c) show the sheet electron density n_s and mobility μ with respect to gate voltage for sample #1 obtained at $T = 2\,\mathrm{K}$. Adapted from Ref. [23].

additional overlapping $1/B$-periodic oscillations emerge at fields $B \gtrsim B_\mathrm{CR}$ that correspond to Shubnikov-de Haas oscillations, which were also observed in dark magnetotransport measurements. Therefore, in the presented curves the driving current has been adjusted to $I = 16\,\mu\mathrm{A}$, which completely suppresses the SdH oscillations in the measured photosignals. This fact clearly rules out that the oscillations at higher applied currents presented in Fig. 28 are caused by a decrease of the SdH oscillation amplitude due to carrier heating similar to the results discussed in Chap. 5. Instead, all findings described above provide strong evidence that the oscillations in Fig. 28 indeed originate from the TIRO effect. Note that the respective resonance field $B_\mathrm{CR} = 0.47\,\mathrm{T}$, which corresponds to a cyclotron mass of $m_\mathrm{CR} = 0.019\ m_\mathrm{e}$, with m_e being the electron mass, has been extracted from separate magnetotransmission measurements. Irradiation of the sample by circularly polarized terahertz radiation yields CR dips of the radiation transmission at positive fields for σ^+ polarization, and at negative fields for σ^-. These results have been double-checked on ungated square-shaped samples with a side length of 5 mm that were fabricated from

the same wafer as sample #1. Such macroscopic samples generally yield more pronounced dips in radiation transmission measurements than Hall bar samples with a micrometer-sized conduction channel.

The MIRO-like photoresistivity oscillations were observed for a Fermi level position in the conduction band within a wide electron density range corresponding to applied gate voltages between $V_\mathrm{g} = 2\,\mathrm{V}$ and $10\,\mathrm{V}$. However, they disappear in the range below $2\,\mathrm{V}$ where Hall measurements without incident radiation indicate the transition to a transport regime with two types of carriers. In this range, the Fermi energy crosses both conduction and valence band resulting in the coexistence of electron and holes in the system, see Fig. 17 (b). Figures 28 (b) and (c) present the sheet electron density n_s and mobility μ as a function of the applied gate voltage. Here, the density $n_\mathrm{s}\,(V_\mathrm{g})$ has been extracted from the Hall resistivity $\rho_{xy}\,(V_\mathrm{g})$ with respect to the applied gate voltage measured for a constant applied magnetic field $B = 0.2\,\mathrm{T}$. Note that the linearity of $\rho_{xy}\,(B)$ has been checked for $2\,\mathrm{V} < V_\mathrm{g} < 10\,\mathrm{V}$ to ensure proper results with this method. In this range, the electron density rises from $2 \cdot 10^{11}\,\mathrm{cm}^{-2}$ up to $7 \cdot 10^{11}\,\mathrm{cm}^{-2}$ and the mobility reduces from $5 \cdot 10^5\,\mathrm{cm}^2/(\mathrm{V\,s})$ to $2.5 \cdot 10^5\,\mathrm{cm}^2/(\mathrm{V\,s})$, see Figs. 28 (b) and (c). Note that for $V_\mathrm{g} \gtrsim 6\,\mathrm{V}$ the carrier density dependence $n_\mathrm{s}\,(V_\mathrm{g})$ featured in Fig. 28 (b) begins to deviate from a linear dependence $n_\mathrm{s} \propto V_\mathrm{g}$. This is most probably linked to the occupation of the second electron subband in the HgTe quantum well [100]. As can be seen in Fig. 28 (a), the increase of the electron density at higher gate voltages leads to a moderate boost of the MIRO amplitude, whereas the positions of the MIRO nodes as well as oscillation extrema do not change.

6.2 Discussion

In the following, the characteristic features of the observed MIRO-like oscillations in the 20 nm HgTe quantum well are explained in the framework of the displacement mechanism [102, 103] which captures the experimental findings well. Note that there are also other theoretical descriptions of the MIRO effect, such the inelastic mechanism [104–106] or other approaches, that attribute MIRO to boundary effects, originating from the finite sample size [59, 107], or classical memory effects [108].

Essentially, the quasiclassical displacement model describes how the spatial displacements of electron cyclotron orbits due to radiation-assisted impurity scat-

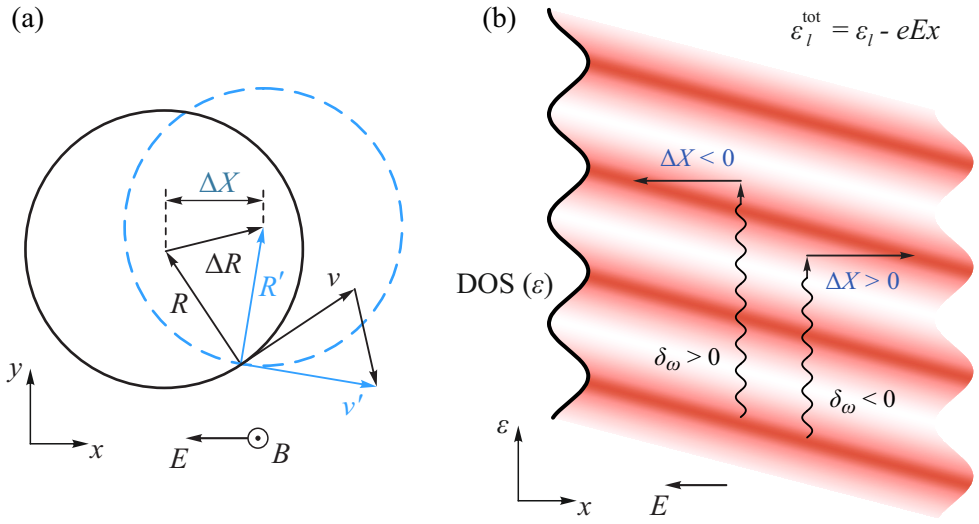

Figure 29: Panel (a): Schematic illustration of the scattering-induced guiding center shift ΔR of the cyclotron orbit with radius R normal to the magnetic field $\boldsymbol{B} \parallel \hat{\boldsymbol{z}}$. ΔX denotes the component of ΔR parallel to the electric force $-e\boldsymbol{E}$ resulting from the dc electric field $\boldsymbol{E}$ applied along negative x-direction. R and v (R' and v') designate the CR orbit center and direction of motion of the electron before (after) the scattering event. Panel (b): Sketch of the correlation between the direction of the guiding center shifts ΔX and the sign of the excitation frequency detuning δ_ω from the second harmonic of cyclotron resonance. The red graded areas correspond to the maxima of the density of states of the Landau levels $\varepsilon_l^{\mathrm{tot}}$ that are spatially tilted because of the external electric field $\boldsymbol{E}$. Adapted from Ref. [101].

tering can lead to ω/ω_c-periodic oscillations in the photoconductivity. There are several prerequisites for the model, such as an applied magnetic field that induces Landau quantization and a symmetry breaking dc electric field that leads to a tilting of the Landau energies in real space. Furthermore, the model requires the existence of defects that can act as scattering centers as well as lead to a broadening of the Landau levels (LLs). The displacement mechanism can be intuitively understood on a qualitative level. First, the Landau quantization due to the normally applied magnetic field leads to a periodic modulation in the density of states (DOS) for a system with parabolic dispersion described by

$$\mathrm{DOS}(\varepsilon) \simeq \mathrm{DOS}(\varepsilon + \hbar\omega_c) \ . \tag{57}$$

In an ideal, clean system with a delta-like DOS of the LLs, radiation-induced excitation of the carriers is only possible by dipole-allowed transitions between neighboring LLs for radiation energies equivalent to the cyclotron energy $\hbar\omega_c$. However, introducing impurities to the system causes a disorder-broadening of

the LLs and also lifts the selection rules, which permits also optical transitions between distant LLs. Thus, the carriers can also be excited by radiation energies that are smaller or greater than integer multiples of the cyclotron energy. Due to the spatial asymmetry of the DOS induced by the dc electric field $\boldsymbol{E}$, carriers that are excited in such a way into regions where the DOS is not maximal will statistically scatter more likely into the direction of increasing DOS, see Fig. 29 (b). This leads to an average shift ΔX of the cyclotron orbit guiding centers as illustrated in Fig. 29 (a). For excitation of a state, initially located at a maximum of the DOS, with radiation energies slightly smaller than multiples of $\hbar\omega$, i.e. a small negative detuning $\delta_\omega = \omega/\omega_\mathrm{c} - N < 0$ from the Nth harmonic of CR, the charge carriers therefore have an increased probability to scatter against the direction of the applied dc electric field ($\Delta X > 0$). On the other hand, for energies with a slight positive detuning $\delta_\omega > 0$ from CR, scattering in the direction of the dc bias field becomes more likely, which results in an average spatial shift of the cyclotron motion guiding centers $\Delta X < 0$. This directional scattering of charge carriers leads to either an increase (for $\Delta X > 0$) or decrease (for $\Delta X < 0$) of the current flow depending on the excitation energy. To be more precise, the preferred direction of the described displacement with respect to the symmetry breaking dc field oscillates with ω/ω_c. In turn, this manifests in radiation-induced oscillations of the observed longitudinal resistivity with period ω/ω_c as observed in the experiment. Note that for carriers which are excited from a maximum of the DOS to another maximum by radiation energies equal to exact multiples of the cyclotron energy, no preferred scattering direction exists since the DOS decreases symmetrically in both directions. This results in nodes of the photoresistivity at multiples of the cyclotron frequency, in accordance to the obtained experimental findings.

In the limit $\omega_\mathrm{c}\tau_\mathrm{q} \ll 1$, which describes strongly disorder-broadened and overlapping LLs, the magnetic field dependence of MIRO is expressed by [101]

$$\frac{\Delta\rho_{xx}}{\rho_{xx}} = -A\frac{\omega}{\omega_\mathrm{c}}\sin\left(\frac{2\pi\omega}{\omega_\mathrm{c}}\right)\exp\left(\frac{-2\pi}{\omega_\mathrm{c}\tau_\mathrm{q}}\right) \ . \tag{58}$$

Here, $\Delta\rho_{xx}$ stands for the radiation-induced correction to the dark dissipative resistivity ρ_{xx}, A is an amplitude factor which is proportional to the radiation power P in case of sufficiently low P, and τ_q denotes the quantum scattering time responsible for an exponential damping of the oscillations at small magnetic fields. Due to this damping at low B, the radiation frequency f

has to be comparable or larger than the quantum scattering rate $1/\tau_q$, i.e. $f\tau_q \gtrsim 1$, in order to observe MIRO [101]. In most materials, this scattering rate lies in the picosecond or subpicosecond range [56]. Thus, strong MIRO and particularly associated zero-resistance states so far could only be observed in two-dimensional electron systems with ultra-high quality, such as high-mobility GaAs/AlGaAs quantum wells with mobilities up to $\mu \gtrsim 10^7\,\mathrm{cm}^2/(\mathrm{V\,s})$ [24, 99], or ultraclean two-dimensional electron systems on the surface of liquid helium [109–111]. In contrast, the mobility of carriers in the investigated HgTe quantum well sample #1 is significantly smaller (see Tab. 3), which yields rather short momentum relaxation times τ, ranging from 2.8 ps to 5.7 ps in the relevant gate voltage range, and even smaller quantum lifetimes $\tau_q < \tau$. However, MIRO-like oscillations are still clearly detected in the terahertz range of frequencies. In fact, recent experiments have successfully demonstrated that by using terahertz radiation frequencies, the rigid requirements on the material properties are significantly alleviated and pronounced MIRO-like (or in this case TIRO) oscillations can be excited even in GaAs heterostructures with a rather low mobility of only $\mu = 1.5 \cdot 10^5\,\mathrm{cm}^2/(\mathrm{V\,s})$ [27, 28]. In the present study of terahertz-induced resistance oscillations in 20 nm HgTe quantum wells, the experimental conditions yield a fairly small value of $f\tau_q \approx 1$, which leads to a fast decay of the oscillations at small magnetic fields, see Fig. 28 (a). In the experiment, TIRO were only detected for the lowest radiation frequency $f = 0.69\,\mathrm{THz}$ and were absent at higher frequencies. However, this is in line with previous theoretical and experimental studies (see, e.g., Refs. [28, 101]) which indicate a swift decline of the MIRO amplitude for higher radiation frequencies corresponding to a theoretical ω^{-4}-scaling of the amplitude parameter A in Eq. (58). Therefore, it is not surprising that TIRO were not observed at higher frequencies $f = 1.63\,\mathrm{THz}$ and $2.54\,\mathrm{THz}$ within the range of intensities available, in spite of the considerably higher value of $f\tau_q$ at higher frequencies. Note that the results displayed in this chapter and published in the original paper [23] present the first observation of terahertz-induced resistance oscillations in HgTe quantum wells.

It should be mentioned that the experimental findings are also in agreement with the inelastic model of MIRO [104, 105]. In contrast to the displacement mechanism where an equilibrium electron distribution function is assumed, in the inelastic model MIRO emerge due to a radiation-induced correction to the distribution function. However, since both models yield a similar periodic-

ity and phase of the resulting resistance oscillations, effectively they can be regarded as two different contributions that add up in the generation of the MIRO phenomenon. Which of the two mechanisms dominates is in general strongly dependent on temperature and the correlation properties of the disorder present in the respective system [101]. In systems with a fast energy relaxation of the carriers, i.e. a high inelastic scattering rate $1/\tau_{\mathrm{in}}$, the inelastic contribution proportional to τ_{in} is small compared to the displacement contribution. On the other hand, the inelastic contribution dominates in systems with a slow energy thermalization, i.e. large inelastic scattering times τ_{in} [104]. Even though the experimental findings for MIRO-like oscillations in 20 nm HgTe quantum wells can be well explained in the framework of both models, it is difficult to identify which mechanism dominates in said case because it is not known experimentally which kind of impurities dominate in HgTe quantum well structures. Then again, the type of disorder is crucially important for the displacement contribution, which becomes small in case of dominant small-angle scattering [112, 113]. To conclude, the MIRO-like effect resulting from the interplay between photon energy and cyclotron energy provides a solid theoretical basis for understanding the oscillatory terahertz photoresistivity in high mobility HgTe quantum wells, as demonstrated above.

7 Cyclotron resonance of topological surface states in $Cd_xHg_{1-x}Te$ bulk films

In the previous chapters photoconductivity in two-dimensional quantum well structures was discussed. Now, we turn to the terahertz magnetospectroscopy of three-dimensional $Cd_xHg_{1-x}Te$ films. In the following, results of photogalvanic, photoconductivity, and radiation transmission studies of samples with different cadmium concentrations are presented and discussed. It will be demonstrated that cyclotron resonance of the topologically protected surface states has been observed in topologically non-trivial $Cd_xHg_{1-x}Te$ films.

7.1 Cyclotron resonances in $Cd_xHg_{1-x}Te$ films

Let us begin with the description of magnetic field dependences of the terahertz radiation transmission obtained for two almost identical $Cd_{0.15}Hg_{0.85}Te$ films #A and #B. With a Cd content of $x = 0.15$ both samples exhibit a negative band gap, i.e. inverted band ordering, in the flat region for temperatures $T \lesssim 90\,\mathrm{K}$ [9]. Additionally, the flat region is encapsulated by areas with gradually increasing Cd content providing smooth interfaces to domains without band inversion, see Figs. 18 (b) and (c). Magnetotransmission measurements in Faraday geometry at liquid helium temperature using a continuous wave molecular gas laser at frequency $f = 2.54$ and $1.63\,\mathrm{THz}$ reveal three resonant dips for both negative and positive values of the out-of-plane magnetic field: Two narrow sharp resonances at magnetic fields $\pm B_{\mathrm{CR1}}$ and $\pm B_{\mathrm{CR2}}$, and broad minima at higher magnetic fields $\pm B_{\mathrm{i}}$, as highlighted in Figs. 30 (a) and (b). Note that the positions of all resonances are always symmetrically offset from $B = 0$ and the exact values can be found in Tab. 4. The two sharp, low-field resonances are sensitive to the helicity of the incident radiation, i.e. resonances at $+B_{\mathrm{CR1,2}}$ only appear for σ^+ polarization, while dips at $-B_{\mathrm{CR1,2}}$ solely emerge for a σ^--polarized laser beam. In addition, the resonance positions scale linearly with the frequency of the electric field, as shown in Fig. 30 (d). Those characteristics point towards cyclotron resonance of negatively charged free carriers being the cause of the sharp, low-field magnetotransmission dips. The broad minima in the magnetotransmission curve at $\pm B_{\mathrm{i}}$, however, are insensitive to the radiation helicity and appear at positive and negative magnetic fields for both σ^+- and σ^--polarized radiation.

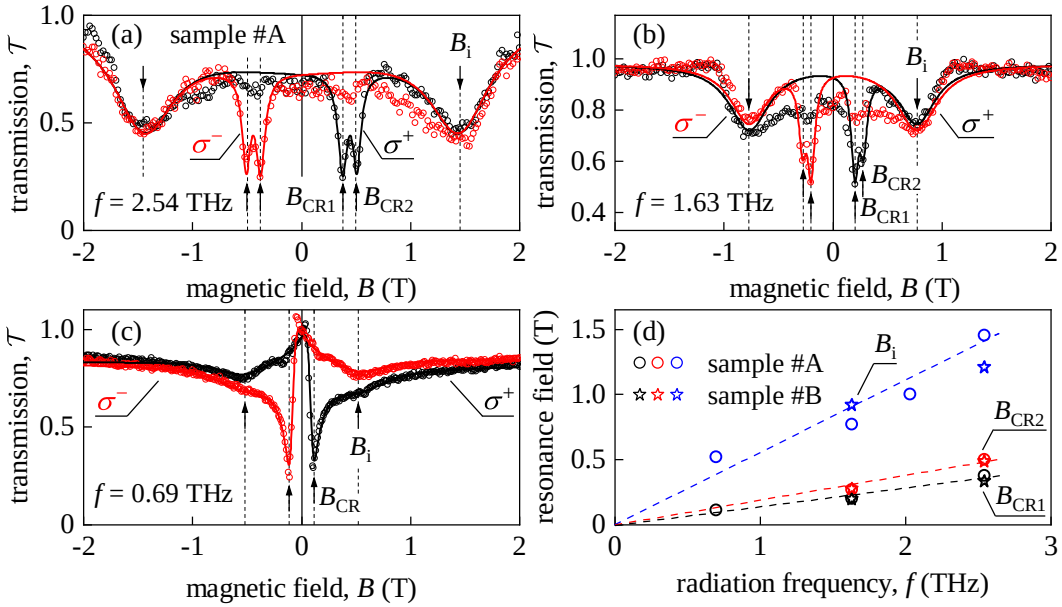

Figure 30: Panels (a) to (c): Magnetotransmission normalized to its maximum value for sample #A with a cadmium content of $x = 0.151$ corresponding to a band inversion in the flat region. The data were obtained in Faraday configuration at $T = 4.2\,\mathrm{K}$ using σ^+- and σ^--polarized radiation with frequency $f = 2.54\,\mathrm{THz}$ (a), $1.63\,\mathrm{THz}$ (b), and $0.69\,\mathrm{THz}$ (c) and is shown by open circles whereas solid lines are fits after Eq. 60, as described in Chap. 7.3. In all cases sharp, deep, helicity-dependent minima are observed at the position of cyclotron resonance (Narrow double resonances B_{CR1} and B_{CR2} in panels (a) and (b), and a single resonance B_{CR} in panel (c)) as indicated by arrows and labeled for positive magnetic fields. At higher fields a wide symmetric minima insensitive to the radiation helicity is observed at B_i. Panel (d) shows the extracted resonance fields B_{CR1}, B_{CR2} and B_i plotted against radiation frequency for sample #A (circles) and #B (stars). Dashed lines correspond to linear fits through the coordinate origin. Adapted from Ref. [30].

These resonances are attributed to photoionization of impurities and will be addressed in detail later in Chap. 7.2. Certainly, the presence of two distinct CRs at B_{CR1} and B_{CR2}, as clearly observed for 2.54 THz (see Fig. 30 (a)), evidently reveals the existence of two kinds of electrons with different cyclotron masses in the system. These could either be bulk electrons or protected surface state electrons that form at the interfaces of the topologically non-trivial flat region and the surrounding, topologically trivial areas of increasing Cd content. Note that for lower radiation frequencies, the two distinct CRs begin to merge and at $f = 0.69\,\mathrm{THz}$ cannot be resolved and appear as a single merged dip at $\pm B_{CR}$ in the magnetotransmission curve, see Fig. 30 (c). For sample #B the observed CR positions are almost identical to those detected in sample #A, as shown in Fig. 30 (d).

Along with the transmission data, photovoltage signals were additionally mon-

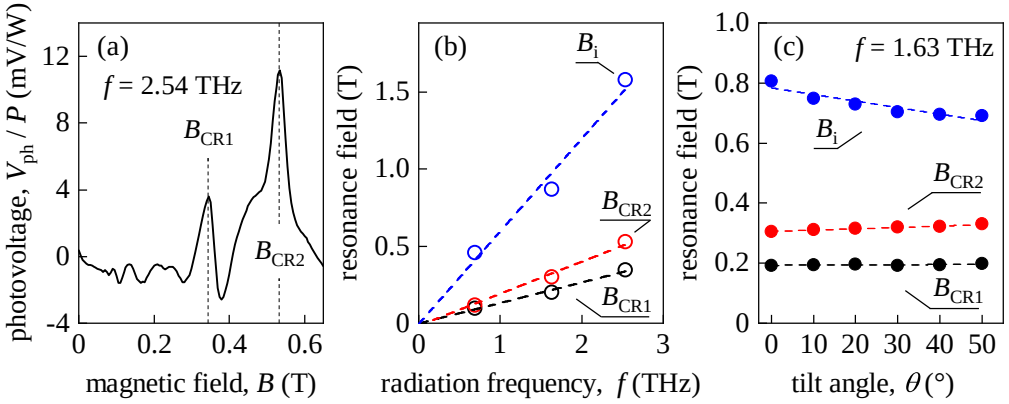

Figure 31: Panel (a): Photovoltage V_{ph} normalized to the incident radiation power P with respect to magnetic field. The data were obtained on sample #A in Faraday configuration at $f = 2.54\,\mathrm{THz}$ and $T = 4.2\,\mathrm{K}$. Dashed lines highlight the characteristic maxima at B_{CR1} and B_{CR2}. Panel (b) displays the dependence of the resonance fields B_{CR1}, B_{CR2} and B_{i}, extracted from the photovoltage signals measured on sample #A at $T = 4.2\,\mathrm{K}$, on the radiation frequency. Panel (c): Dependence of the resonance fields on the tilt angle θ. The data were extracted from photovoltage measurements on sample #A at $T = 4.2\,\mathrm{K}$ and $f = 1.63\,\mathrm{THz}$ in Faraday configuration with the sample tilted by the angle θ. Dashed lines correspond to linear fits of the data. Adapted from Ref. [30].

itored using corner or edge contacts of van der Pauw samples. Cyclotron resonance was also observed in the photovoltage traces in form of sharp resonant peaks as exemplarily demonstrated for sample #A and frequency $f = 2.54\,\mathrm{THz}$ in Fig. 31 (a). The positions of the two resonant photovoltage peaks coincide with the CR dips in magnetotransmission at B_{CR1} and B_{CR2}, as indicated by the dashed black lines. Similar to the magnetotransmission data, the magnetic field values of both CR-resonant photovoltage peaks also scale linearly with radiation frequency, see Fig. 31 (b). Note that in the photovoltage traces, the two resonances are distinctly resolved even at the lowest frequency $f = 0.69\,\mathrm{THz}$, in contrast to magnetotransmission where the resonances are merged into one dip for this frequency, see Fig. 30 (c).

To check whether the two CRs stem from bulk or topological surface states, experiments with tilted magnetic field were carried out. In a two-dimensional electron gas, the cyclotron resonance position is known to shift to significantly higher magnetic fields B for increasing tilt angles θ. This is because CR of carriers bound to a two-dimensional plane is only sensitive to the magnetic field component $B_{\perp} = B\cos\theta$ normal to this plane. In a three-dimensional electron system, however, the carriers are free to perform the cyclotron motion normal to the applied magnetic field $\boldsymbol{B}$ and the resonance position therefore

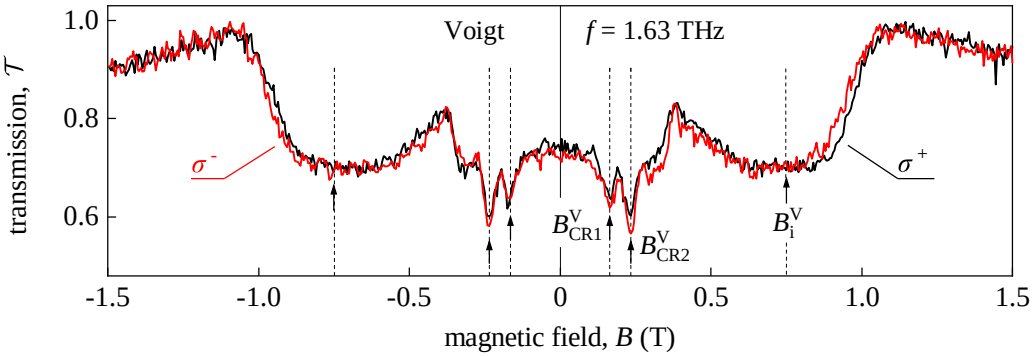

Figure 32: Normalized magnetotransmission traces measured in Voigt configuration on sample #A at $T = 4.2\,\mathrm{K}$ with σ^+- (black curve) and σ^--polarized (red curve) radiation with $f = 1.63\,\mathrm{THz}$. Two pairs of sharp, well resolved CR dips at $B^{\mathrm{V}}_{\mathrm{CR1}}$ and $B^{\mathrm{V}}_{\mathrm{CR2}}$ are observed symmetrically for positive as well as negative magnetic fields for both radiation helicities. In addition, broad helicity-insensitive resonances emerge for higher magnetic fields at $B^{\mathrm{V}}_{\mathrm{i}}$. Adapted from Ref. [30].

is independent of the tilt angle. Note that even in case of three-dimensional electrons, the resonance position may vary slightly with θ due to anisotropy of the effective mass. However, this shift is substantially smaller than the shifts at large tilting angles in case of two-dimensionally confined carriers. Experimentally, tilted magnetic fields were implemented by rotation of the sample by an angle θ. This leads to a reduced magnetic field component normal to the sample surface, as well as oblique incidence of radiation. The analysis of the photovoltage traces for different tilt angles, presented in Fig. 31 (c), shows that the positions of $B_{\mathrm{CR1,2}}$ are almost independent of θ. These findings indicate a three-dimensional nature of the charge carriers responsible for the CR at $B_{\mathrm{CR1,2}}$ rather than a two-dimensional character. This conclusion is confirmed by further magnetotransmission measurements in Voigt configuration. Here, both CRs are still observable even for an in-plane orientation of the magnetic field, as shown in Fig. 32, providing a clear evidence that the resonances are excited in a three-dimensional electron system. Note that in Voigt geometry the CR dips, as expected, are independent of the radiation helicity and present at positive and negative magnetic fields for both helicities. Additionally, the CR magnetic fields $B^{\mathrm{V}}_{\mathrm{CR1,2}}$ observed in sample #A with an applied in-plane magnetic field are slightly smaller than those detected with the out-of-plane field orientation, see Tab. 4. This fact can be attributed to well-known plasmonic shifts [114] which will be discussed later in Chap. 7.3. However, such shifts are not detected for the other samples, as can be seen in Tab. 4.

Alongside samples #A and #B with gradually increasing Cd content on both

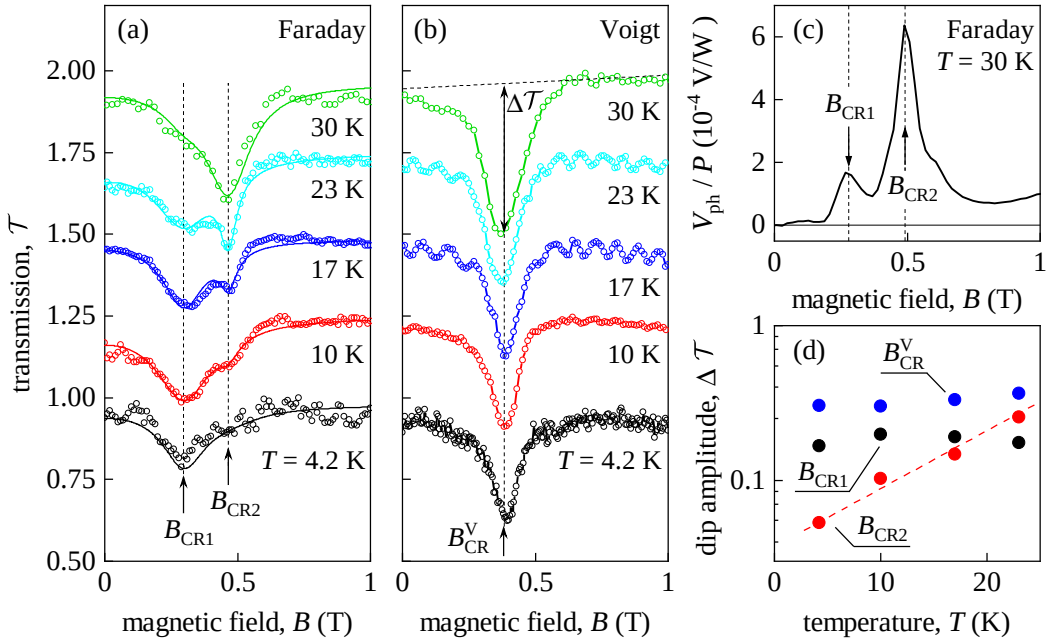

Figure 33: Normalized magnetotransmission data measured on sample #C in Faraday (a) and Voigt configuration (b) at different temperatures with a radiation frequency of $f = 2.54\,\mathrm{THz}$. Here, empty circles correspond to measurement data points, whereas solid lines in panel (a) are fits according to Eq. (60). Note that the traces are offset by 0.25 each for clarity. Panel (c) shows the photovoltage signal normalized to the incident radiation power P measured on sample #C in Faraday configuration at a temperature $T = 30\,\mathrm{K}$. Panel (d) presents the temperature dependences of the dip amplitudes $\Delta\mathcal{T}$ of the CR dips at B_{CR1} (black circles), B_{CR2} (red circles) in Faraday and B_{i} (blue circles) in Voigt geometry, extracted from the magnetotransmission data presented in panel (a) and (b). The red dashed line is a guide for the eye. Adapted from Ref. [30].

sides of the flat region, a $Cd_{0.15}Hg_{0.85}Te$ film with an abrupt boundary between the flat region with $x = 0.15$ and the cap layer, termed sample #C (see Fig. 18 (d)), was also studied. Despite the fact that the Cd content in the flat region is the same and that the films only differ in the top interface of the flat region, the behavior of the CRs is qualitatively different in sample #C. Similar to samples #A and #B, two clearly resolved CRs were observed for sample #C in both magnetotransmission (see Fig. 33 (a)) and photovoltage (see Fig. 33 (c)) in Faraday configuration. However, when switching to the in-plane orientation of the magnetic field, only one CR dip was detected in magnetotransmission in sample #C, as shown in Fig. 33 (b). The fact that the other resonance cannot be excited for an in-plane magnetic field is a clear evidence that it stems from two-dimensionally confined electronic states.

To further investigate the nature of the charge carriers responsible for the

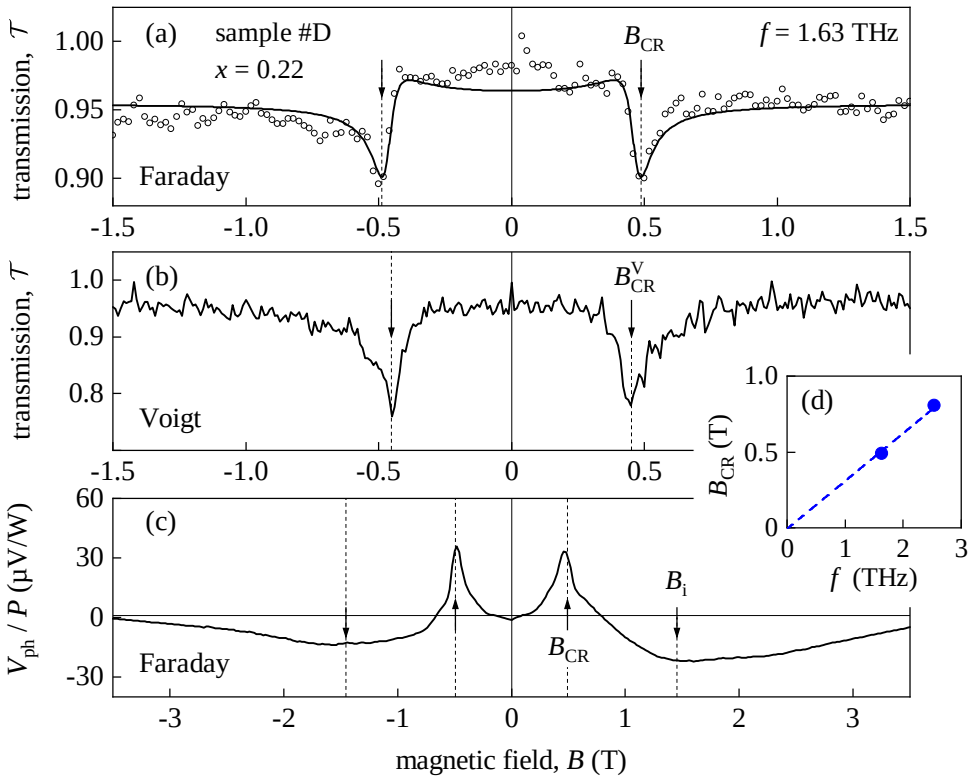

Figure 34: Normalized magnetotransmission measured in Faraday (a) and Voigt configuration (b) on sample #D with a cadmium content of $x = 0.22$ (i.e. without band inversion in the flat region). The data were obtained at $T = 4.2\,\mathrm{K}$ using linearly polarized radiation with $f = 1.63\,\mathrm{THz}$. Black circles in panel (a) correspond to measurement data while the black solid line is a fit according to Eq. (60). Panel (c) shows the photovoltage V_{ph} normalized to the incident radiation power P obtained under the same conditions as panel (a) in Faraday geometry. Panel (d) displays the extracted resonance fields B_{CR} with respect to radiation frequency. The blue dashed line is a linear fit through the coordinate origin. Adapted from Ref. [30].

two CRs, the dip amplitudes $\Delta\mathcal{T}$ at B_{CR1}, B_{CR2}, and $B_{\mathrm{CR}}^{\mathrm{V}}$ were extracted for different temperatures. These data are depicted in Fig. 33 (d). While for B_{CR1} (Faraday configuration) and $B_{\mathrm{CR}}^{\mathrm{V}}$ (Voigt configuration), $\Delta\mathcal{T}$ is almost independent of temperature, the dip amplitude at B_{CR2}, which is detected only for the out-of-plane magnetic field orientation, is strongly increasing with rising temperature. This behavior is remarkably similar to the temperature evolution of the CR dip amplitude for the topological surface states previously observed in strained 80 nm and 200 nm HgTe films [18, 19]. Thus, these findings indicate the formation of two-dimensional surface states at the sharp interface between the topologically non-trivial flat region with $x = 0.15$ and the topologically trivial cap layer.

So far, all investigated samples have a Cd content of $x = 0.15$ in the flat region

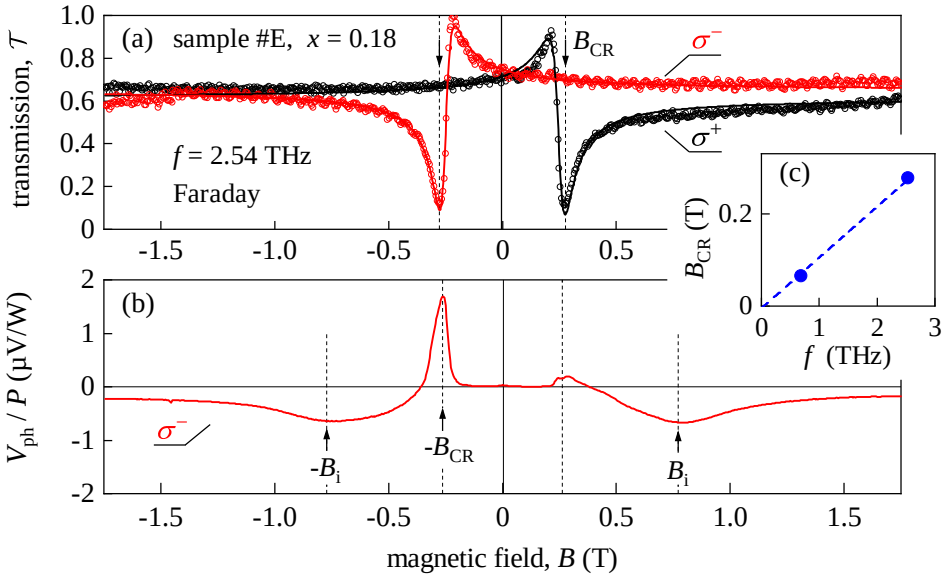

Figure 35: Panel (a): Normalized magnetotransmission of circularly polarized radiation with $f = 2.54\,\mathrm{THz}$ measured on sample #E with a cadmium content of $x = 0.18$. The data were obtained at $T = 4.2\,\mathrm{K}$ in Faraday configuration. The simultaneously recorded normalized photovoltage V_{ph}/P is shown in panel (b) for a σ^--polarized laser beam. Panel (c) features the extracted resonance fields B_{CR} plotted against the radiation frequency. The blue dashed line is a linear fit through the coordinate origin. Adapted from Ref. [30].

resulting in a negative bandgap and therefore inverted band ordering at low temperatures. Now, let us turn to the investigation of samples #D ($x = 0.22$) and #E ($x = 0.18$) with a higher Cd content that results in a conventional band ordering in the flat region. At liquid helium temperature, where the measurements were carried out, the critical Cd content indicating the transition from positive to negative gap energy, i.e. from conventional to inverted band ordering, is around $x_{\mathrm{c}}(4.2\,\mathrm{K}) \simeq 0.17$ [9, 115], see Fig. 7 (b). Consequently, in conditions of our experiments, sample #D and #E are expected to behave as topologically trivial narrow-gap semiconductors. Indeed, in both samples only a single CR is observed in the experiment. Figures 34 (a) and (b) show the magnetotransmission data obtained on sample #D for out-of-plane (Faraday configuration) and in-plane magnetic fields (Voigt configuration). In both cases, only one CR is present at B_{CR} or $B_{\mathrm{CR}}^{\mathrm{V}}$. Note that the data in Fig. 34 were obtained with linearly polarized terahertz radiation, which results in the resonances being present for both polarities of magnetic field. A similar picture is observed in the magnetotransmission spectrum of sample #E presented in Fig. 35 (a) which features only one highly asymmetrical CR. Similar to previous samples, the CR magnetic fields B_{CR} in sample #D and #E also scale

linearly with radiation frequency, as shown in Figs. 34 (d) and Fig. 35 (c), respectively. However, it is worth highlighting that the corresponding cyclotron masses m_{CR} in samples #D ($x = 0.22$) and #E ($x = 0.18$) (see Tab. 4) are significantly different to those detected in samples with $x = 0.15$. Actually, this is in agreement with the evolution of the band structure for a variation of the cadmium content. The largest cyclotron mass is expected for the $x = 0.22$ sample because of the large band gap and corresponding parabolic dispersion. On the other hand, the lowest mass is predicted to occur in the $x = 0.18$ sample, which is closest to the critical Cd content $x_c(T = 4.2\,K) \simeq 0.17$ associated with a gapless, linear energy dispersion. In fact, the obtained cyclotron masses shown in Tab. 4 exactly match this anticipated behavior.

The monitoring of photogalvanics reveals a strong resonant enhancement of the photovoltage at the CR magnetic field B_{CR} in both sample #D and #E, as shown in Figs. 34 (c) and 35 (b). Under linearly polarized terahertz irradiation, the photovoltage peaks appear symmetrically at positive and negative magnetic fields (see Fig. 34 (c)), while for circular polarization they behave helicity-dependent and emerge solely for the respective active magnetic field polarity (see Fig. 35 (b)). Note that in Fig. 35 (b), an additional peak with a substantially smaller amplitude was detected at the corresponding CR inactive magnetic field polarity. This is most probably caused by parasitic antenna effects produced by the contact wires which can cause a slight distortion of the incident radiation polarization. In addition to CR, the photovoltage traces in all investigated samples (#A to #E) also exhibit a broad helicity-independent resonance at the magnetic field B_i which is exemplarily shown and highlighted in Fig. 34 (c) and Fig. 35 (b) for sample #D and #E, respectively. These resonances appear due to photoionization of impurities and will be discussed in the following chapter.

7.2 Impurity resonances in $Cd_xHg_{1-x}Te$ films

Besides the CRs at low magnetic fields, which represent the main focus of this study, broader resonances at higher magnetic fields were observed in all investigated samples in magnetotransmission, photovoltage, and also photoconductivity, see e.g. in Figs. 30 or 35. As will be demonstrated later, these resonant features appear due to the photoionization of impurity states in the $Cd_xHg_{1-x}Te$ films and, thus, they are referred to as impurity resonances in the

following. These impurity resonances always emerge at moderate magnetic fields $\pm B_i$ for both in-plane and out-of-plane orientation (see Figs. 30 and 32). Furthermore, they are insensitive to the radiation helicity and appear symmetrically in magnetic field for both σ^+ and σ^-, as well as linear polarization (see Figs. 30, 32, and 34). This fact clearly rules out that these resonances are caused by CR. The impurity resonance fields scale linearly with radiation frequency, as demonstrated in Figs. 30 (d) and 31 (b) for B_i extracted from magnetotransmission and photovoltage in samples #A and #B. Magnetotransmission measurements at different temperatures reveal that the dip amplitude $\Delta\mathcal{T}$ at B_i greatly decreases with rising temperatures and even vanishes for $T \gtrsim 30\,\mathrm{K}$, see Fig. 36 (a). Moreover, also the resonance positions B_i themselves are sensitive to temperature and drift to slightly smaller magnetic fields with increasing temperature, as shown Fig. 36 (b). This strongly contrasts the temperature evolution of the observed low-field CRs with the resonance fields $B_{CR1,2}$ being independent of temperature and the dip amplitude $\Delta\mathcal{T}$ being either constant or increasing for rising temperatures, see Fig. 33. Note that the impurity resonance fields B_i for a given radiation frequency substantially differ between samples with different Cd content, as can be seen in Tab. 4. In addition, it is worth noting that while for samples #A, #B, and #C, with $x = 0.15$ in the flat region, the impurity resonance was detected in both magnetotransmission and photogalvanics, in samples #D and #E, with $x > x_c$, they were observed only in photovoltage but not in magnetotransmission.

So far, these features point towards photoionization of impurity states as cause of the resonant behavior at B_i if one considers the effect of the magnetic freeze-out of impurities [116]. This effect describes the significant increase of the activation energies of shallow impurities due to an applied magnetic field. If the resonant behavior at B_i indeed stems from such an ionization of impurites, this would result in different kinetics of the photoresponse at B_i compared to that at $B_{CR1,2}$. Therefore, the photoconductive response of the $Cd_xHg_{1-x}Te$ films to terahertz radiation was probed using cw radiation as well as a pulsed molecular THz laser for additional time-resolved photoconductivity measurements. Similar to the photovoltage data, a very strong enhancement of the photoresponse at magnetic fields around the impurity resonance $\pm B_i$ was also observed in the photoconductivity $\Delta\sigma/\sigma$ traces, as shown exemplarily for sample #A in Fig. 36 (c). An analysis of the time-resolved photoconductivity signals indeed reveals substantial different kinetics at B_i and B_{CR}, see Fig. 36 (d). The

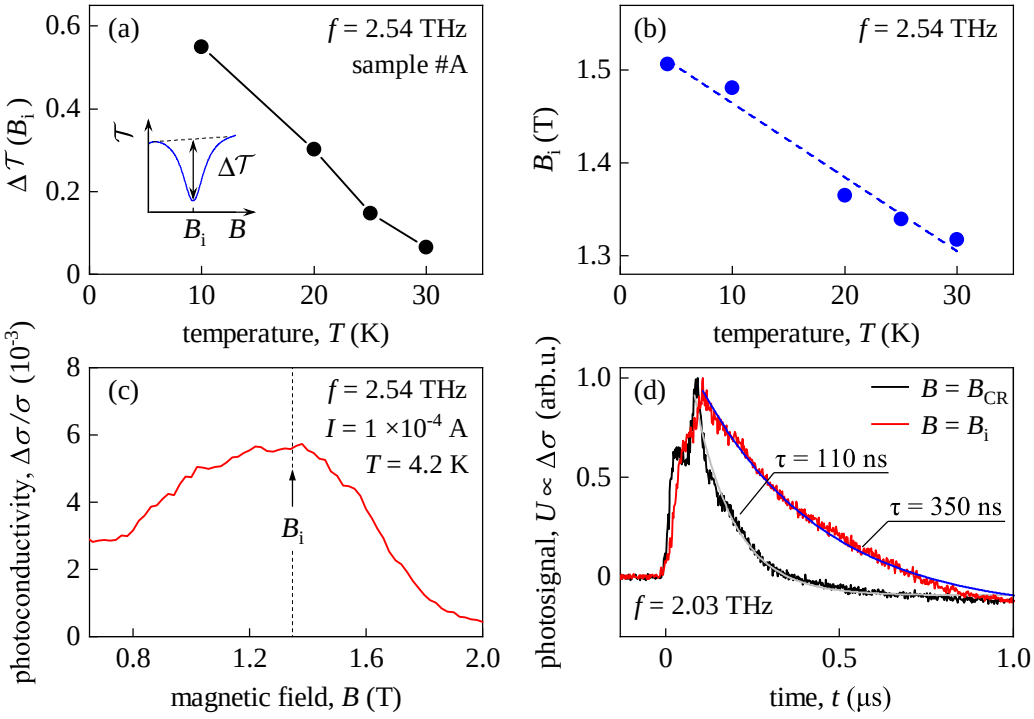

Figure 36: Panel (a): Temperature dependence of the amplitudes $\Delta\mathcal{T}$ of the Lorentzian dips in magnetotransmission around the impurity resonance at B_i extracted from data measured on sample #A for $f = 2.54\,\mathrm{THz}$. The inset illustrates how the dip amplitudes were obtained. Panel (b) depicts the temperature dependence of the impurity resonance position B_i extracted from the same data set. Note that the dashed blue curve is a guide for the eye. Panel (c): Magnetic field dependence of the normalized photoconductivity $\Delta\sigma/\sigma$ measured on sample #A at liquid helium temperature and $f = 2.54\,\mathrm{THz}$ with an applied current of 100 µA. Panel (d): Time-resolved photoconductivity responses $U \propto \Delta\sigma$ normalized to their maximum value obtained on sample #A at $T = 4.2\,\mathrm{K}$ using a pulsed molecular gas laser operating at $f = 2.03\,\mathrm{THz}$. The black curve was recorded at an applied magnetic field $B = B_\mathrm{CR} = 0.29\,\mathrm{T}$ corresponding to CR, whereas the red curve was obtained at the center of the impurity resonance at $B = B_\mathrm{i} = 1.0\,\mathrm{T}$. Solid blue and grey curves indicate exponential fits $\propto \exp(-t/\tau)$ with the corresponding decay times $\tau = 110\,\mathrm{ns}$ at B_CR and $\tau = 350\,\mathrm{ns}$ at B_i. Adapted from Ref. [30].

decay of the photoresponse at the impurity resonance B_i (red trace in Fig. 36 (d)) is several times slower than that at B_CR (black trace in Fig. 36 (d)), where the photosignal essentially reproduces the temporal shape of the terahertz laser pulse (not shown). This indicates that the kinetics of the electrons involved in CR is fast on the time scale of the pulse duration which is given by $\tau_\mathrm{pulse} \approx 100\,\mathrm{ns}$. On the other hand, the photoresponse at B_i exhibits a considerable long time tail that can be well fitted by an exponential function $\exp(-t/\tau)$ (blue line in Fig. 36 (d)) with a decay time $\tau = 350\,\mathrm{ns}$. Note that in photoconductivity only a single merged CR at B_CR was resolved in sample

#A even at the highest frequency $f = 2.54\,\mathrm{THz}$ instead of the split resonance detected in photovoltage and transmission experiments.

These findings provide clear evidence that the resonance at B_i is indeed caused by the magnetic field-mediated photoionization of shallow impurity states in the $Cd_xHg_{1-x}Te$ films. In this model, the magnetic freeze-out of the impurities defines a parametric region of moderate magnetic fields around B_i where the photoionization of impurity states into the conduction band becomes possible. At zero or low magnetic fields, the impurity activation energy is so small that all impurities are already thermally ionized even at low temperatures as in our experiments. This effectively inhibits the photoionization of the impurity states [117]. However, with increasing magnetic field the activation energy of the impurities increases so that, at sufficiently low temperatures, they are no longer thermally activated but remain in their neutral state. At the same time, the photon energy is larger than the activation energy, which allows photoionization of electrons from impurity states to the conduction band. In this region of magnetic fields, a significant influence of the photoionization process manifests in the transmission, photogalvanic, and photoconductive signals. Upon further increase of the magnetic field strength, however, photoionization is no longer possible as soon as the energy distance between ground impurity level and vacant unbound conduction band states exceeds the photon energy. In this way, photoionization is limited to a range of intermediate magnetic fields centered around a characteristic field B_i, and sufficiently small temperatures, as observed in the experiments. Furthermore, B_i is expected to increase with radiation frequency and should, additionally, be strongly sensitive to temperature and Cd content in the film, since both of these parameters modify the energy band dispersion and, therefore, also affect the position of impurity levels. The temperature dependence of B_i can additionally be affected by possible processes where electrons on hydrogen-like impurity states are first photoexcited into higher bound levels and, subsequently, thermally activated into the continuum of unbound conduction band states [118, 119].

7.3 Discussion

As discussed above, cyclotron resonances from two types of carriers with different cyclotron masses were observed in magnetotransmission and photovoltage traces obtained on samples with a topologically non-trivial flat region, see e.g.

Fig. 30. Strikingly, one of these CRs behaves qualitatively different in samples with a sharp top interface between layers with inverted and non-inverted band ordering compared to samples with smooth interfaces. In sample #C, which hosts a sharp top interface, the two-dimensional nature of the corresponding carriers has been demonstrated by experiments with an in-plane magnetic field orientation where the respective CR is absent. The strong temperature dependence observed in Faraday configuration additionally distinguishes this CR from other resonances present in both Faraday and Voigt geometry which likely originate from three-dimensional carriers localized at smooth interfaces.

All these results support the conclusion that smooth interfaces between layers with inverted and non-inverted band ordering lead to the formation of multiple surface states, also known as Volkov-Pankratov states (VPSs) [15, 120–122]. In systems where multiple VPSs are occupied, the carrier dynamics can be effectively three-dimensional, which provides an explanation for the experimental observations. This behavior is similar to the quasi two-dimensional nature of electrons populating multiple subbands in a wide quantum well, e.g. at higher temperature. Aside from the requirement for at least one VPS at the interface between materials with different topology, the number of VPSs is generally not fixed and their number and properties are affected by various parameters, such as the material choice, growth conditions, form of interfaces, and strain profile.

However, an important fact that at first glance seems to contradict the conclusion that the discussed resonance stems from topologically protected two-dimensional surface states is the observed frequency dependence of the resonance position. As presented in Figs. 30 (d) and 31 (b), the resonance positions scale fairly linearly with radiation frequency. Yet, this seemingly conflicts the well-known fact that the transition energies between adjacent Landau levels scale with $\sqrt{B}$ in systems with linear dispersion, such as topologically protected surface states [75]. In fact, in the semiclassical limit of high chemical potential, where many Landau levels are populated and the radiation energy is significantly smaller than the Fermi energy, the linear scaling on B, known from systems with parabolic band dispersion, is approximately restored even for Dirac quasiparticles, as shown in Chap. 2.4 and Refs. [74, 77]. Although this quasiclassical approach works well for all radiation frequencies used in this work, a reliable determination of the exact chemical potential in the investigated structures turned out to be quite difficult due to the presence of several

types of carriers as well as surface states. At the same time, an experimental evidence for the scaling according to $\sqrt{B}$ would require further CR studies in a broader frequency range.

Another point that needs to be addressed is the highly asymmetrical shape of the CR dips in the magnetotransmission curves, e.g. in Figs. 30 (c) and 35 (a). This asymmetry is a signature of strong interference effects [123] and is well captured by the displayed fits based on a two-component Drude model which considers interference of the electric field due to multiple reflections within the sample substrate. In this model, the complex terahertz conductivity σ, which determines the electric field transmitted through the sample, is calculated as the sum of all contributions from the prevailing conduction channels. Following the Drude formula, the conductivity σ_j of each electron transport channel j is given by [30]

$$\sigma_j = \frac{e n_{\mathrm{s},j}}{\mu_j^{-1} + i\left(B_{\mathrm{CR}j} \pm B\right)} \ . \tag{59}$$

Here, e denotes the elementary charge, $n_{\mathrm{s},j}$ and μ_j are the respective electron sheet density and mobility in transport channel j, and $B_{\mathrm{CR}j} = m_{\mathrm{CR}j} 2\pi f/e$ is the magnetic field strength where CR occurs for a given frequency f. This magnetic field value is characteristic for each conduction channel j and defined by the corresponding cyclotron mass $m_{\mathrm{CR}j}$ of the charge carriers within this channel. Note that the plus and minus sign before B in Eq. (59) correspond to the left-handed and right-handed circular polarization state of the incident terahertz electric field, respectively. The total terahertz conductivity $\sigma = \sum_j \sigma_j$ is then given as the sum over all contributions and with $\tilde{\sigma} = \sigma/\left(2\varepsilon_o c\right)$ the fraction of power transmitted through the sample in Faraday configuration can be expressed by [30]

$$\mathcal{T}\left(B\right) = \left| \left(1+\tilde{\sigma}\right)\cos\phi - i\frac{1+n_{\mathrm{r}}^2+2\tilde{\sigma}}{2n_{\mathrm{r}}}\sin\phi \right|^{-2} \ . \tag{60}$$

Here, ε_0 denotes the vacuum permittivity, c is the speed of light, n_{r} the refractive index of the substrate, and ϕ denotes the interference phase that the electromagnetic wave accumulates after a single reflection in the substrate. Depending on this interference phase, the shape of the transmission dips can be either symmetrical in B under conditions of constructive interference ($\sin\phi = 0$) or destructive interference ($\cos\phi = 0$), or asymmetrical for intermediate values

of ϕ [123]. With this model it is possible to qualitatively fit all magnetotransmission curves with good agreement even those that are highly asymmetrical. In fact, the observation of such strong asymmetry in the experiment clearly underlines the importance of interference effects in terahertz magnetotransmission studies. However, the magnetotransmission curves normalized to the respective maximum, as measured in the experiment, do not provide sufficient information to precisely extract all model parameters. Therefore, additional amplitude scaling and a constant offset accounting for non-resonant contributions of other transport channels were implemented in the fitting process. Note that for higher magnetic fields, two additional, identical, negative Lorentzian functions centered at B_i and $-B_\mathrm{i}$ were added to Eq. (60) to consider the additional resonant radiation absorption due to the impurity resonance at $\pm B_\mathrm{i}$.

As briefly mentioned in Chap. 7.1, the CRs observed in sample #A in Voigt configuration exhibit a slight down-shift to smaller magnetic fields $B^\mathrm{V}_\mathrm{CR1,2}$ in comparison to the Faraday resonance positions $B_\mathrm{CR1,2}$, see Tab. 4. This is attributed to the plasmonic shift of resonances emerging in Voigt geometry. Here, the resonance condition is given by $\omega^2 = \omega_\mathrm{p}^2 + \omega_\mathrm{c}^2$, which implies that the resonant frequency ω is affected by the plasma frequency $\omega_\mathrm{p} = ne^2/m\varepsilon$ of the three-dimensional electron gas [114]. In Faraday configuration, on the other hand, this condition is simply given by $\omega^2 = \omega_\mathrm{c}^2$ and resonance and cyclotron frequency correspond to each other. A rough estimation of the relative permittivity $\varepsilon_\mathrm{r} = \varepsilon/\varepsilon_0 \approx 10$ in the $Cd_{0.15}Hg_{0.85}Te$ film allows to calculate the carrier density corresponding to the observed plamonic shift in sample #A according to

$$B^\mathrm{V}_\mathrm{CR}/B_\mathrm{CR} = \sqrt{1 - \omega_\mathrm{p}^2/\omega^2}\ . \tag{61}$$

Taking the extracted cyclotron mass of about $m_\mathrm{CR}/m_\mathrm{e} = 0.004$ (see Tab. 4), one finds that the detected relative shifts $B^\mathrm{V}_\mathrm{CR}/B_\mathrm{CR} \approx 0.8$ correspond to a volume carrier density of about $n \approx 5 \cdot 10^{14}\,\mathrm{cm}^{-3}$, which agrees almost perfectly with the value obtained from magnetotransport characterization, see Tab. 2. However, it is surprising that in sample #B no significant plasmonic shift has been detected although sample #A and #B have essentially the same design and Cd content.

A well-known related material where topological states have been intensively studied for systems with sharp interfaces are strained HgTe films [18, 124, 125].

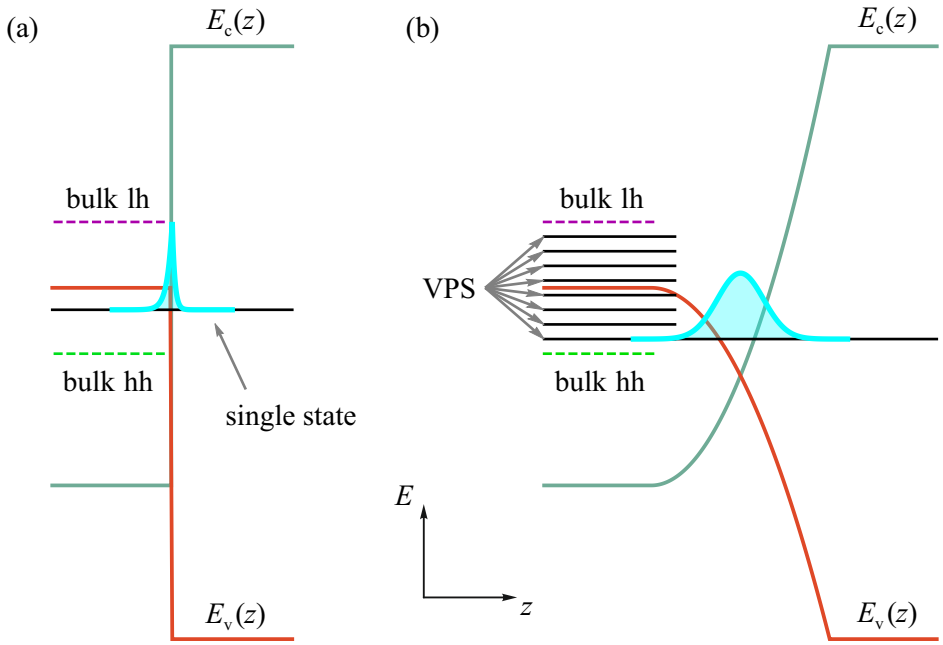

Figure 37: Illustration of the spatial probability density distribution (highlighted in cyan) of the surface states emerging in $Cd_xHg_{1-x}Te$ films with sharp (a) and smooth interfaces (b) between the CdHgTe film with inverted band ordering on the left side and the cap layer with regular band ordering on the right. Orange and turquoise solid lines picture the evolution of the main energy bands $E_v(z)$ and $E_c(z)$ with respect to the z-direction. In case of a smooth interface (b) multiple VPS levels arise between the bulk light and heavy hole subbands that are indicated by the green and purple dashed lines, whereas for a sharp interface (a) only a single topologically protected surface state is present. Adapted from Ref. [30].

In such films, the energies of the protected surface states lie between the energy levels of the light and heavy hole subbands depending on the wavevector $k_\parallel$ in the interface plane [16, 47]. For $k_\parallel = 0$, the energy of the lowest topological surface state corresponds to the top of the heavy-hole subband, while for $\left|k_\parallel\right| \to \infty$, the high-energy surface state dispersion converges to the light hole one. Internal strain in the crystal opens up an energy gap between the two hole subbands that is only crossed by the surface state dispersion. Therefore, in strained HgTe films with the Fermi level right in this gap, the transport properties at low temperatures are expected to be determined strongly by the topologically protected surface states. Note that the surface state dispersion, at the same time, is significantly affected by hybridization with the heavy hole band [30]. $Cd_xHg_{1-x}Te$ films with a band inversion and sharp interfaces behave quite similar to strained HgTe films concerning the properties mentioned above.

However, the situation changes if one considers smooth interfaces with grad-

ually varying Cd content between materials with and without band inversion. The following calculations demonstrate that rather than a single topologically protected state, a smooth interface can indeed host multiple VPSs [15, 120–122]. The VPS energies also lie between the light and heavy hole bands, analogously to the case of sharp interfaces described above. Figure 37 schematically illustrates the forming of the surface states at a sharp interface (a) as well as at a smooth interface (b). The left parts correspond to the flat region in a $Cd_{0.15}Hg_{0.85}Te$ film with inverted band ordering, the right parts to the cap layer with non-inverted dispersion, and the middle parts to the different types of interfaces. In case of the sharp interface sketched in panel (a), the topological surface state forms directly at the sharp interface and its spatial extension is characterized by a rather fast exponential decay of the wave function inside the CdHgTe film and the cap layer. On the other hand, for smooth interfaces, the extension of the VPSs is determined by the spatial gradient of the band gap near the band inversion point. The spatial distribution of the probability density for the respective wave functions is depicted in Fig. 37 in cyan color. Thus, an enlargement of the transition region between the materials with different topology leads to an increase in both the total number and width of the VPSs. This provides an explanation for the qualitatively different behavior of the CR in Voigt configuration observed in samples #A and #C which have nearly identical design and differ only in the interface type. Sample #C with a sharp, abrupt interface hosts two-dimensional surface states that cannot be excited into CR by an in-plane magnetic field parallel to the interface. Sample #A, however, displays the typical behavior of a quasi two-dimensional system with several occupied subbands.

Supporting numerical calculations were carried out by Dr. G. V. Budkin in the framework of the six-band Kane model, additionally considering a static crystal strain that leads to a splitting of heavy and light hole subbands. The corresponding Kane Hamiltonian is given in the basis of the Γ_6 and Γ_8 states as

$$\mathcal{H} = \begin{pmatrix} E_c \mathbb{1}_2 & H_{cv} \\ H_{cv}^\dagger & E_v \mathbb{1}_4 + H_{BP} \end{pmatrix} . \tag{62}$$

Here, $\mathbb{1}_n$ represents the $n \times n$ identity matrix and

$$H_{\mathrm{cv}}^{\dagger} = P_{\mathrm{cv}} \begin{pmatrix} -\frac{k_x - ik_y}{\sqrt{2}} & 0 \\ \sqrt{\frac{2}{3}} k_z & -\frac{k_x - ik_y}{\sqrt{6}} \\ \frac{k_x + ik_y}{\sqrt{6}} & \sqrt{\frac{2}{3}} k_z \\ 0 & \frac{k_x + ik_y}{\sqrt{2}} \end{pmatrix} , \tag{63}$$

where P_{cv} is the Kane parameter and H_{BP} represents the Bir-Pikus Hamiltonian. Additionally, the splitting of the heavy and light hole bands is introduced by adding a non-zero u_{zz} component to the strain tensor. In this case, the Bir-Pikus Hamiltonian is given by the diagonal matrix

$$H_{\mathrm{BP}} = b u_{zz} \,\mathrm{diag}\,(-1, 1, 1, -1) \tag{64}$$

with b being the valence band deformation potential. In the following, u_{zz} is chosen in such a way that the heavy hole subband is below the light-hole one.

The resulting Hamiltonian for the CdHgTe bulk film has three double-degenerate eigenstates: on top, the light hole subband states with energy $\varepsilon_{\mathrm{l}}(k)$, then the dispersionless heavy hole subband states described by $\varepsilon_{\mathrm{h}}(k)$ below them, followed by the low-lying conduction band states with dispersion $\varepsilon_{\mathrm{c}}(k)$. The corresponding energies are given by

$$\varepsilon_{\mathrm{l,c}} = E_0 \pm \sqrt{\delta^2 + 2P_{\mathrm{cv}}^2 k^2/3} \tag{65}$$

and

$$\varepsilon_{\mathrm{h}}(k) = E_{\mathrm{v}} - b u_{zz} \tag{66}$$

with

$$2E_0 = E_{\mathrm{v}} + b u_{zz} + E_{\mathrm{c}} \quad \text{and} \quad 2\delta = E_{\mathrm{v}} + b u_{zz} - E_{\mathrm{c}} \; . \tag{67}$$

Now, the wave functions and VPS spectrum for a smooth interface are calculated by considering the dependence of the band edges E_{c} and E_{v} on the z coordinate which corresponds to the growth direction of the $\mathrm{Cd}_x\mathrm{Hg}_{1-x}\mathrm{Te}$ films. For the calculation of the VPSs in sample #A, the gap energy $E_{\mathrm{c}} - E_{\mathrm{v}} = -32\,\mathrm{meV}$ for $\mathrm{Cd}_{0.15}\mathrm{Hg}_{0.85}\mathrm{Te}$ is introduced [46], the parameter $2m_0 \left(P_{\mathrm{cv}}/\hbar\right)^2 = 18.8\,\mathrm{eV}$ is fixed according to Ref. [126], and the dependences of $E_{\mathrm{c}}(z)$ and $E_{\mathrm{v}}(z)$ are ex-

tracted from the sample compound profiles shown in Fig. 18. Furthermore, the parameter $bu_{zz} = 2\,\mathrm{meV}$ is set and a static electric field $E = 2\,\mathrm{kV/cm}$ at the band closing is added. For $k_{\parallel} = 0.02\,\mathrm{nm}^{-1}$, the calculations yield the existence of three VPSs in the $Cd_{0.15}Hg_{0.85}Te$ film at energies 3 meV, 5 meV, and 8 meV with respect to the heavy hole energy at the Γ point. Their probability density is distributed over hundreds of nanometers, which is larger than the cyclotron radius r_c of the carriers in the $Cd_{0.15}Hg_{0.85}Te$ samples. The corresponding cyclotron radii $r_c = v/\omega = v/(2\pi f)$ for the frequencies $f = 2.54\,\mathrm{THz}$, $1.63\,\mathrm{THz}$, and $0.69\,\mathrm{THz}$ in the experiment are calculated as $r_c = 65\,\mathrm{nm}$, $100\,\mathrm{nm}$, and $240\,\mathrm{nm}$, respectively, by using the estimate $v = \sqrt{2/3}P_{cv}/\hbar \approx 10^8\,\mathrm{cm/s}$ for the carrier velocity. Note that the calculations have also shown that the variation of the band gap as well as the energy splitting of the light and heavy hole bands, introduced by the strain and the static electric field, have a very strong influence on the number of VPSs emerging at such smooth interfaces. Since these parameters are not precisely known, they are implemented here as phenomenological parameters. To summarize, the presented calculations demonstrate that in $Cd_xHg_{1-x}Te$ films smooth interfaces with gradually varying Cd content x can indeed result in the emergence of Volkov-Pankratov states. This, in turn, results in a quasi two-dimensional character of the charge carriers polulating the VPSs and, consequently, cyclotron resonance can be excited for magnetic fields in both in-plane and out-of-plane orientation.

sample	cadmium content, x	frequency, f(THz)	B_{CR1}(T) or B_{CR}(T)	B_{CR2}(T)	B_{i}(T)	$B^{\mathrm{V}}_{\mathrm{CR1}}$(T) or $B^{\mathrm{V}}_{\mathrm{CR}}$(T)	$B^{\mathrm{V}}_{\mathrm{CR2}}$(T)	$m_{\mathrm{CR1}}/m_{\mathrm{e}}$	$m_{\mathrm{CR2}}/m_{\mathrm{e}}$
# A	0.15	2.54	0.38	0.50	1.45			0.0042	0.0055
		1.63	0.20	0.27	0.77	0.16	0.24	0.0035	0.0046
		0.69	0.09*	0.11	0.52*			0.0035	0.0044
# B	0.15	2.54	0.33	0.49	1.25	0.36	0.50	0.00365	0.0053
		1.63	0.20	0.28	0.92	0.20	0.28	0.0034	0.0047
# C	0.15	2.54	0.30	0.46	1.35*	0.39	–	0.0033	0.0051
# D	0.22	2.54	0.81	–	2.33*	0.82	–	0.0089	–
		1.63	0.49	–	1.45*	0.45	–	0.0084	–
# E	0.18	2.54	0.28	–	0.77*			0.0031	–
		0.69	0.065	–	0.25*			0.0026	–

Table 4: Resonance magnetic fields and the corresponding cyclotron masses extracted from magnetotransmission and photovoltage traces obtained at $T = 4.2\,\mathrm{K}$. Note that resonances marked with an asterisk were visible in photovoltage only and were not resolved in magnetotransmission. Dashed entries indicate that the corresponding resonances were not detected in the measurements.

8 Summary and Outlook

In the framework of this thesis, optical excitation of two- and three-dimensional HgTe-based structures was studied in the topologically trivial as well as non-trivial regime. By means of terahertz spectroscopy, intriguing optoelectronic effects were observed in these materials. In HgTe quantum wells of different width, a photoconductive response was detected that systematically changes its sign depending on the external out-of-plane magnetic field [23]. Moreover, terahertz-induced resistance oscillations resulting from the interplay of the photon and cyclotron energies were observed in a high-mobility 20 nm QW. This represents the first observation of TIRO in HgTe QWs so far [23]. Furthermore, cyclotron resonance of the two-dimensional surface states was detected in topologically non-trivial $Cd_xHg_{1-x}Te$ films [30]. All here mentioned experimental findings were presented and discussed in Chaps. 5, 6, and 7.

The sign-alternating photoconductivity, presented in Chap. 5, was observed in several HgTe QWs corresponding to normal and inverted band ordering as well as linear dispersion. Variation of the radiation frequency showed that the photoconductive signal at zero magnetic field decreases for rising frequencies following the dependence of classical, Drude-like radiation absorption. This demonstrates that photoconductivity is caused by free carrier heating. In both photoconductivity and photoresistivity, the experiments revealed a sign inversion at a moderate magnetic field strength that increases for rising temperatures. Within the model of μ-photoconductivity it was shown that this sign inversion implies a non-monotonic behavior of the transport scattering rate, which was indeed confirmed by dark magnetotransport measurements. Further studies revealed an additional sign inversion that was observed at very low fields solely in the photoconductivity signals. This sign inversion was shown to emerge as a result of the transition from classically weak to classically strong magnetic fields. Comparison with dark magnetotransport data demonstrates that the respective inversion field is inversely proportional to the carrier mobility in the QW offering an unconventional optoelectronical method to probe the carrier mobility [23].

In Chap. 6, the oscillatory photoresponse observed in a high-mobility 20 nm HgTe QW was presented. The experiments revealed ω/ω_c-periodic oscillations in the photoresistivity at low magnetic fields. Extraction of the corresponding cyclotron mass showed that the oscillation nodes coincide with the position

of CR and its higher harmonics. This demonstrated that these oscillations are caused by the interplay of the photon and cyclotron energies similar to MIRO but for illumination with terahertz radiation [23]. It was shown that the TIRO can be well described by the displacement and inelastic mechanisms established for MIRO. However, from the data of the current study it is hard to state which mechanism dominates in the generation of the TIRO in HgTe QWs. In future investigations, a more detailed study of the temperature dependence of the observed TIRO could help in understanding the different weights of both inelastic and displacement contribution. Still, interpretation of such data has to be performed with great care, since temperature not only modifies the inelastic MIRO contribution but also affects the density of states which becomes relevant at high temperatures for both mechanisms [101].

Besides two-dimensional systems, terahertz optoelectronics were also studied in three-dimensional $Cd_xHg_{1-x}Te$ films with different Cd contents and interface types. These experiments, presented in Chap. 7, demonstrated that the formation of fully two-dimensional topological surface states requires sharp interfaces between layers with and without band inversion. This finding is of high importance for future investigations of the topologically non-trivial nature of epitaxially grown $Cd_xHg_{1-x}Te$ crystals. Indeed, it was shown that only in case of a sharp top boundary, the corresponding surface state CR was observed for an out-of-plane orientation of the external magnetic field but absent for an in-plane orientation. On the other hand, in samples with a top interface with gradually varying Cd content, the surface state CR was detected for both out-of-plane and in-plane magnetic fields revealing the effectively three-dimensional nature of the associated carriers. The subsequent discussion of the results within the framework of Volkov-Pankratov states and a theoretical modeling of the surface states for different film designs carried out by G. V. Budkin from the Ioffe Institute in St. Petersburg demonstrated the strong influence of the interface type on the formation of two-dimensional surface states [30]. Moreover, the experiments revealed additional broad, helicity-independent resonances with slower kinetics and a higher temperature sensitivity in all samples, which were attributed to photoionization of impurity states. Note that besides the semiclassical regime of high chemical potential that was investigated in this work, future studies of the surface state CR in topological $Cd_xHg_{1-x}Te$ films should address the quantum-mechanical limit, where the photon energy becomes comparable to the Fermi energy. In this

limit, the scaling of $\omega_c \propto \sqrt{B}$ should be clearly observable. Furthermore, the studies should be focused on films with sharp boundaries between the flat region and the buffer and cap layers to ensure the perfectly two-dimensional character of the surface states.

References

[1] W. D. Lawson, S. Nielsen, E. H. Putley, and A. S. Young, *Preparation and properties of HgTe and mixed crystals of HgTe-CdTe*, J. Phys. Chem. Solids **9**, 325–329 (1959).

[2] P. Norton, *HgCdTe infrared detectors*, Opto-Electron. Rev. **10**, 159–174 (2002).

[3] V. S. Varavin, S. A. Dvoretsky, V. I. Liberman, N. N. Mikhailov, and Y. G. Sidorov, *Molecular beam epitaxy of high quality $Hg_{1-x}Cd_xTe$ films with control of the composition distribution*, J. Cryst. Growth **159**, 1161–1166 (1996).

[4] S. A. Dvoretsky, Z. D. Kvon, N. N. Mikhailov, V. A. Shvets, A. L. Aseev, B. Wittmann, S. N. Danilov, and S. D. Ganichev, *CdHgTe-based nanostructures for photodetectors*, J. Opt. Technol. **76**, 787–790 (2009).

[5] S. A. Dvoretsky, N. N. Mikhailov, Y. G. Sidorov, V. A. Shvets, S. N. Danilov, B. Wittman, and S. D. Ganichev, *Growth of HgTe Quantum Wells for IR to THz Detectors*, J. Electron. Mater. **39**, 918–923 (2010).

[6] N. N. Berchenko and M. V. Pashkovskiĭ, *Mercury telluride – a zero-gap semiconductor*, Sov. Phys. Uspekhi **19**, 462–480 (1976).

[7] R.-L. Chu, W.-Y. Shan, J. Lu, and S.-Q. Shen, *Surface and edge states in topological semimetals*, Phys. Rev. B **83**, 075110 (2011).

[8] M. Orlita, D. M. Basko, M. S. Zholudev, F. Teppe, W. Knap, V. I. Gavrilenko, N. N. Mikhailov, S. A. Dvoretskii, P. Neugebauer, C. Faugeras, A.-L. Barra, G. Martinez, and M. Potemski, *Observation of three-dimensional massless Kane fermions in a zinc-blende crystal*, Nat. Phys. **10**, 233–238 (2014).

[9] F. Teppe, M. Marcinkiewicz, S. S. Krishtopenko, S. Ruffenach, C. Consejo, A. M. Kadykov, W. Desrat, D. But, W. Knap, J. Ludwig, S. Moon, D. Smirnov, M. Orlita, Z. Jiang, S. V. Morozov, V. Gavrilenko, N. N. Mikhailov, and S. A. Dvoretskii, *Temperature-driven massless Kane fermions in HgCdTe crystals*, Nat. Commun. **7**, 12576 (2016).

[10] B. A. Bernevig, T. L. Hughes, and S.-C. Zhang, *Quantum Spin Hall Effect and Topological Phase Transition in HgTe Quantum Wells*, Science **314**, 1757–1761 (2006).

[11] M. König, S. Wiedmann, C. Brüne, A. Roth, H. Buhmann, L. W. Molenkamp, X.-L. Qi, and S.-C. Zhang, *Quantum Spin Hall Insulator State in HgTe Quantum Wells*, Science **318**, 766–770 (2007).

[12] M. Z. Hasan and C. L. Kane, *Colloquium: Topological insulators*, Rev. Mod. Phys. **82**, 3045–3067 (2010).

[13] J. E. Moore, *The birth of topological insulators*, Nature **464**, 194–198 (2010).

[14] S.-Q. Shen, *Topological Insulators: Dirac Equation in Condensed Matters* (Springer Berlin Heidelberg, 2012).

[15] B. A. Volkov and O. A. Pankratov, *Two-dimensional massless electrons in an inverted contact*, Pis'ma Zh. Eksp. Teor. Fiz. **42**, 145–148 (1985), [JETP Lett. **42**, 178 (1985)].

[16] O. A. Pankratov, S. V. Pakhomov, and B. A. Volkov, *Supersymmetry in heterojunctions: Band-inverting contact on the basis of* $Pb_{1-x}Sn_xTe$ *and* $Hg_{1-x}Cd_xTe$, Solid State Commun. **61**, 93–96 (1987).

[17] K.-M. Dantscher, D. A. Kozlov, M. T. Scherr, S. Gebert, J. Bärenfänger, M. V. Durnev, S. A. Tarasenko, V. V. Bel'kov, N. N. Mikhailov, S. A. Dvoretsky, Z. D. Kvon, J. Ziegler, D. Weiss, and S. D. Ganichev, *Photogalvanic probing of helical edge channels in two-dimensional HgTe topological insulators*, Phys. Rev. B **95**, 201103(R) (2017).

[18] K.-M. Dantscher, D. A. Kozlov, P. Olbrich, C. Zoth, P. Faltermeier, M. Lindner, G. V. Budkin, S. A. Tarasenko, V. V. Bel'kov, Z. D. Kvon, N. N. Mikhailov, S. A. Dvoretsky, D. Weiss, B. Jenichen, and S. D. Ganichev, *Cyclotron-resonance-assisted photocurrents in surface states of a three-dimensional topological insulator based on a strained high-mobility HgTe film*, Phys. Rev. B **92**, 165314 (2015).

[19] S. Candussio, G. V. Budkin, M. Otteneder, D. A. Kozlov, I. A. Dmitriev, V. V. Bel'kov, Z. D. Kvon, N. N. Mikhailov, S. A. Dvoretsky, and S. D. Ganichev, *Cyclotron-resonance-induced photogalvanic effect in surface states of 200-nm-thick strained HgTe films*, Phys. Rev. Mater. **3**, 054205 (2019).

[20] C. Zoth, P. Olbrich, P. Vierling, K.-M. Dantscher, V. V. Bel'kov, M. A. Semina, M. M. Glazov, L. E. Golub, D. A. Kozlov, Z. D. Kvon, N. N. Mikhailov, S. A. Dvoretsky, and S. D. Ganichev, *Quantum oscillations of photocurrents in HgTe quantum wells with Dirac and parabolic dispersions*, Phys. Rev. B **90**, 205415 (2014).

[21] P. Olbrich, C. Zoth, P. Vierling, K.-M. Dantscher, G. V. Budkin, S. A. Tarasenko, V. V. Bel'kov, D. A. Kozlov, Z. D. Kvon, N. N. Mikhailov, S. A. Dvoretsky, and S. D. Ganichev, *Giant photocurrents in a Dirac fermion system at cyclotron resonance*, Phys. Rev. B **87**, 235439 (2013).

[22] E. L. Ivchenko and S. D. Ganichev, "Spin-Photogalvanics", in *Spin Physics in Semiconductors* (Springer Berlin Heidelberg, 2008), 245–277.

[23] M. Otteneder, I. A. Dmitriev, S. Candussio, M. L. Savchenko, D. A. Kozlov, V. V. Bel'kov, Z. D. Kvon, N. N. Mikhailov, S. A. Dvoretsky, and S. D. Ganichev, *Sign-alternating photoconductivity and magnetoresistance oscillations induced by terahertz radiation in HgTe quantum wells*, Phys. Rev. B **98**, 245304 (2018).

[24] M. A. Zudov, R. R. Du, J. A. Simmons, and J. L. Reno, *Shubnikov–de Haas-like oscillations in millimeterwave photoconductivity in a high-mobility two-dimensional electron gas*, Phys. Rev. B **64**, 201311 (2001).

[25] P. D. Ye, L. W. Engel, D. C. Tsui, J. A. Simmons, J. R. Wendt, G. A. Vawter, and J. L. Reno, *Giant microwave photoresistance of two-dimensional electron gas*, Appl. Phys. Lett. **79**, 2193–2195 (2001).

[26] R. G. Mani, J. H. Smet, K. von Klitzing, V. Narayanamurti, W. B. Johnson, and V. Umansky, *Zero-resistance states induced by electromagnetic-wave excitation in GaAs/AlGaAs heterostructures*, Nature **420**, 646–650 (2002).

[27] T. Herrmann, I. A. Dmitriev, D. A. Kozlov, M. Schneider, B. Jentzsch, Z. D. Kvon, P. Olbrich, V. V. Bel'kov, A. Bayer, D. Schuh, D. Bougeard, T. Kuczmik, M. Oltscher, D. Weiss, and S. D. Ganichev, *Analog of microwave-induced resistance oscillations induced in GaAs heterostructures by terahertz radiation*, Phys. Rev. B **94**, 081301 (2016).

[28] T. Herrmann, Z. D. Kvon, I. A. Dmitriev, D. A. Kozlov, B. Jentzsch, M. Schneider, L. Schell, V. V. Bel'kov, A. Bayer, D. Schuh, D. Bougeard, T. Kuczmik, M. Oltscher, D. Weiss, and S. D. Ganichev, *Magnetoresistance*

oscillations induced by high-intensity terahertz radiation, Phys. Rev. B **96**, 115449 (2017).

[29] M. L. Savchenko, M. Otteneder, I. A. Dmitriev, N. N. Mikhailov, Z. D. Kvon, and S. D. Ganichev, *Terahertz photoresistivity of a high-mobility 3D topological insulator based on a strained HgTe film*, Appl. Phys. Lett. **117**, 201103 (2020).

[30] M. Otteneder, D. Sacré, I. Yahniuk, G. V. Budkin, K. Diendorfer, D. A. Kozlov, I. A. Dmitriev, N. N. Mikhailov, S. A. Dvoretsky, V. V. Bel'kov, W. Knap, and S. D. Ganichev, *Terahertz Magnetospectroscopy of Cyclotron Resonances from Topological Surface States in Thick Films of* $Cd_xHg_{1-x}Te$, Phys. Status Solidi B **258**, 2000023 (2020).

[31] L. Fu, C. L. Kane, and E. J. Mele, *Topological Insulators in Three Dimensions*, Phys. Rev. Lett. **98**, 106803 (2007).

[32] H. Eschrig, *Topology and Geometry for Physics* (Springer Berlin Heidelberg, 2011).

[33] D. Xiao, M.-C. Chang, and Q. Niu, *Berry phase effects on electronic properties*, Rev. Mod. Phys. **82**, 1959–2007 (2010).

[34] B. A. Bernevig and T. L. Hughes, *Topological Insulators and Topological Superconductors* (Princeton University Press, 2013).

[35] C. L. Kane and E. J. Mele, *Quantum Spin Hall Effect in Graphene*, Phys. Rev. Lett. **95**, 226801 (2005).

[36] C. L. Kane and E. J. Mele, Z_2 *Topological Order and the Quantum Spin Hall Effect*, Phys. Rev. Lett. **95**, 146802 (2005).

[37] P. A. M. Dirac, *The quantum theory of the electron*, Proceedings of the Royal Society of London. Series A, Containing Papers of a Mathematical and Physical Character **117**, 610–624 (1928).

[38] S.-Q. Shen, W.-Y. Shan, and H.-Z. Lu, *Topological insulator and the Dirac equation*, Spin **01**, 33–44 (2011).

[39] T. Ihn, *Semiconductor Nanostructures* (Oxford University Press, 2009).

[40] G. Dresselhaus, *Spin-Orbit Coupling Effects in Zinc Blende Structures*, Phys. Rev. **100**, 580–586 (1955).

[41] E. I. Rashba and V. I. Sheka, *Symmetry of Energy Bands in Crystals of Wurtzite Type II. Symmetry of Bands with Spin-Orbit Interaction Included*, Fiz. Tverd. Tela: Collected Papers **2**, 62–76 (1959).

[42] Y. A. Bychkov and E. I. Rashba, *Properties of a 2D electron gas with a lifted spectrum degeneracy*, Pis'ma Zh. Eksp. Teor. Fiz. **39**, 66–69 (1984), [JETP Lett. **39**, 78–81 (1984)].

[43] G. Bihlmayer, O. Rader, and R. Winkler, *Focus on the Rashba effect*, New J. Phys. **17**, 050202 (2015).

[44] D. J. Chadi, J. P. Walter, M. L. Cohen, Y. Petroff, and M. Balkanski, *Reflectivities and Electronic Band Structures of CdTe and HgTe*, Phys. Rev. B **5**, 3058–3064 (1972).

[45] C. R. Whitsett and D. A. Nelson, *Lattice Thermal Conductivity of p-Type Mercury Telluride*, Phys. Rev. B **5**, 3125–3138 (1972).

[46] J. P. Laurenti, J. Camassel, A. Bouhemadou, B. Toulouse, R. Legros, and A. Lusson, *Temperature dependence of the fundamental absorption edge of mercury cadmium telluride*, J. Appl. Phys. **67**, 6454 (1990).

[47] C. Brüne, C. X. Liu, E. G. Novik, E. M. Hankiewicz, H. Buhmann, Y. L. Chen, X. L. Qi, Z. X. Shen, S. C. Zhang, and L. W. Molenkamp, *Quantum Hall Effect from the Topological Surface States of Strained Bulk HgTe*, Phys. Rev. Lett. **106**, 126803 (2011).

[48] E. B. Olshanetsky, Z. D. Kvon, S. S. Kobylkin, D. A. Kozlov, N. N. Mikhailov, S. A. Dvoretskii, and J. C. Portal, *Quantum Hall effect in a quasi-three-dimensional HgTe film*, JETP Lett. **93**, 526–529 (2011).

[49] J.-W. Luo and A. Zunger, *Design Principles and Coupling Mechanisms in the 2D Quantum Well Topological Insulator* HgTe/CdTe, Phys. Rev. Lett. **105**, 176805 (2010).

[50] O. E. Raichev, *Effective Hamiltonian, energy spectrum, and phase transition induced by in-plane magnetic field in symmetric HgTe quantum wells*, Phys. Rev. B **85**, 045310 (2012).

[51] B. Wittmann, S. N. Danilov, V. V. Bel'kov, S. A. Tarasenko, E. G. Novik, H. Buhmann, C. Brüne, L. W. Molenkamp, Z. D. Kvon, N. N. Mikhailov, S. A. Dvoretsky, N. Q. Vinh, A. F. G. van der Meer, B. Murdin, and S. D. Ganichev, *Circular photogalvanic effect in HgTe/CdHgTe quantum well structures*, Semicond. Sci. Technol. **25**, 095005 (2010).

[52] D. A. Kozlov, Z. D. Kvon, N. N. Mikhailov, and S. A. Dvoretsky, *Weak localization of Dirac fermions in HgTe quantum wells*, JETP Lett. **96**, 730–734 (2013).

[53] Y. Tsay, S. Mitra, and J. Vetelino, *Temperature dependence of energy gaps in some II–VI compounds*, J. Phys. Chem. Solids **34**, 2167–2175 (1973).

[54] R. Dornhaus and G. Nimtz, "The properties and applications of the $Hg_{1-x}Cd_xTe$ alloy system", in *Narrow-gap semiconductors* (Springer Berlin Heidelberg, 1976), 119–286.

[55] M. Martyniuk, J. W. Dell, and L. Faraone, "Mechanical and Thermal Properties", in *Mercury Cadmium Telluride: Growth, Properties and Applications*, edited by P. Capper and J. W. Garland (John Wiley & Sons, Chichester, 2011), 153–204.

[56] S. D. Ganichev and W. Prettl, *Intense Terahertz Excitation of Semiconductors* (Oxford University Press, 2005).

[57] V. I. Belinicher and B. I. Sturman, *The photogalvanic effect in media lacking a center of symmetry*, Sov. Phys. Uspekhi **23**, 199–223 (1980).

[58] M. M. Glazov and S. D. Ganichev, *High frequency electric field induced nonlinear effects in graphene*, Phys. Rep. **535**, 101–138 (2014).

[59] S. A. Mikhailov, *Theory of the giant plasmon-enhanced second-harmonic generation in graphene and semiconductor two-dimensional electron systems*, Phys. Rev. B **84**, 045432 (2011).

[60] P. Olbrich, L. E. Golub, T. Herrmann, S. N. Danilov, H. Plank, V. V. Bel'kov, G. Mussler, C. Weyrich, C. M. Schneider, J. Kampmeier, D. Grützmacher, L. Plucinski, M. Eschbach, and S. D. Ganichev, *Room-Temperature High-Frequency Transport of Dirac Fermions in Epitaxially Grown* Sb_2Te_3- *and* Bi_2Te_3-*Based Topological Insulators*, Phys. Rev. Lett. **113**, 096601 (2014).

[61] M. Otteneder, S. Hubmann, X. Lu, D. A. Kozlov, L. E. Golub, K. Watanabe, T. Taniguchi, D. K. Efetov, and S. D. Ganichev, *Terahertz Photogalvanics in Twisted Bilayer Graphene Close to the Second Magic Angle*, Nano Lett. **20**, 7152–7158 (2020).

[62] S. A. Tarasenko, *Electron scattering in quantum wells subjected to an in-plane magnetic field*, Phys. Rev. B **77**, 085328 (2008).

[63] K. Seeger, *Semiconductor Physics* (Springer Berlin Heidelberg, 1982).

[64] D. Neamen, *Semiconductor Physics and Devices: Basic Principles* (McGraw-Hill, New York, NY, 2012).

[65] C. Hamaguchi, *Basic Semiconductor Physics* (Springer Berlin Heidelberg, 2010).

[66] S. Hunklinger, *Festkörperphysik* (De Gruyter, München, 2009).

[67] H. Ibach and H. Lüth, *Festkörperphysik* (Springer Berlin Heidelberg, 2009).

[68] T. Numai, *Fundamentals of semiconductor lasers* (Springer, New York, 2004).

[69] S. A. Mikhailov, *Microwave-induced magnetotransport phenomena in two-dimensional electron systems: Importance of electrodynamic effects*, Phys. Rev. B **70**, 165311 (2004).

[70] T. Herrmann, I. A. Dmitriev, D. A. Kozlov, M. Schneider, B. Jentzsch, Z. D. Kvon, P. Olbrich, V. V. Bel'kov, A. Bayer, D. Schuh, D. Bougeard, T. Kuczmik, M. Oltscher, D. Weiss, and S. D. Ganichev, *Analog of microwave-induced resistance oscillations induced in GaAs heterostructures by terahertz radiation*, Phys. Rev. B **94**, 081301 (2016).

[71] Q. Zhang, T. Arikawa, E. Kato, J. L. Reno, W. Pan, J. D. Watson, M. J. Manfra, M. A. Zudov, M. Tokman, M. Erukhimova, A. Belyanin, and J. Kono, *Superradiant Decay of Cyclotron Resonance of Two-Dimensional Electron Gases*, Phys. Rev. Lett. **113**, 047601 (2014).

[72] L. D. Landau and E. M. Lifshitz, *Quantum Mechanics: Non-Relativistic Theory* (Elsevier Science, Burlington, 1977).

[73] N. M. R. Peres, F. Guinea, and A. H. Castro Neto, *Electronic properties of disordered two-dimensional carbon*, Phys. Rev. B **73**, 125411 (2006).

[74] A. M. Witowski, M. Orlita, R. Stępniewski, A. Wysmołek, J. M. Baranowski, W. Strupiński, C. Faugeras, G. Martinez, and M. Potemski, *Quasiclassical cyclotron resonance of Dirac fermions in highly doped graphene*, Phys. Rev. B **82**, 165305 (2010).

[75] M. L. Sadowski, G. Martinez, M. Potemski, C. Berger, and W. A. de Heer, *Landau Level Spectroscopy of Ultrathin Graphite Layers*, Phys. Rev. Lett. **97**, 266405 (2006).

[76] Y. Zhang, *Electronic Transport in Graphene*, PhD thesis, Columbia University, 2006.

[77] U. Briskot, I. A. Dmitriev, and A. D. Mirlin, *Quantum magneto-oscillations in the ac conductivity of disordered graphene*, Phys. Rev. B **87**, 195432 (2013).

[78] O. Svelto, *Principles of Lasers* (Springer US, 2010).

[79] Y.-S. Lee, *Principles of Terahertz Science and Technology* (Springer Nature, 2008).

[80] P. Olbrich, *THz radiation induced spin polarized currents in low dimensional semiconductor structures*, PhD thesis, Universität Regensburg, 2010.

[81] C. Zoth, *Terahertz laser radiation induced opto-electronic effects in HgTe based nanostructures*, PhD thesis, Universität Regensburg, 2015.

[82] S. Hubmann, *Terahertz optoelectronics in HgTe-based heterostructures*, PhD thesis, Universität Regensburg, 2020.

[83] S. Jacobsson, *Optically pumped far infrared lasers*, Infrared Phys. **29**, 853–874 (1989).

[84] D. Meschede, *Optics, Light and Lasers* (Wiley VCH Verlag GmbH, 2017).

[85] B. E. A. Saleh and M. C. Teich, *Fundamentals of Photonics* (John Wiley & Sons, Inc., 1991).

[86] T. Chang, "Optical Pumping in Gases", in *Nonlinear Infrared Generation*, Vol. 16, edited by Y. Shen (Springer Berlin Heidelberg, 1977), 215–272.

[87] P. Faltermeier, *Terahertz Laser Induced Ratchet Effects and Magnetic Quantum Ratchet Effects in Semiconductor Nanostructures*, PhD thesis, Universität Regensburg, 2017.

[88] F. Bréhat and B. Wyncke, *Measurement of the optical constants of crystal quartz at 10 K and 300 K in the far infrared spectral range: 10–600 cm^{-1}*, Int. J. Infrared Millimet. Waves **18**, 1663–1679 (1997).

[89] L. J. van der Pauw, *A method of measuring specific resistivity and Hall effect of discs of arbitrary shape*, Philips Res. Rep. **13**, 1–9 (1958).

[90] L. J. van der Pauw, *A Method of Measuring the Resistivity and Hall Coefficient on Lamellae and Arbitrary Shape*, Philips Tech. Rev. **20**, 220–224 (1958).

[91] D. A. Kozlov, Z. D. Kvon, N. N. Mikhailov, S. A. Dvoretskii, and J. C. Portal, *Cyclotron resonance in a two-dimensional semimetal based on a HgTe quantum well*, JETP Lett. **93**, 170–173 (2011).

[92] S. A. Dvoretsky, D. G. Ikusov, D. K. Kvon, N. N. Mikhailov, N. Dai, R. N. Smirnov, Y. G. Sidorov, and V. A. Shvets, *Growing* $HgTe/Cd_{0.735}Hg_{0.265}Te$ *quantum wells by molecular beam epitaxy*, Optoelectron. Instrum. Data Process. **43**, 375–381 (2007).

[93] G. V. Budkin, private communication, 2018.

[94] Z. D. Kvon, E. B. Olshanetsky, D. A. Kozlov, N. N. Mikhailov, and S. A. Dvoretskii, *Two-dimensional electron-hole system in a HgTe-based quantum well*, JETP Lett. **87**, 502–505 (2008).

[95] M. L. Savchenko, D. A. Kozlov, N. N. Vasilev, Z. D. Kvon, N. N. Mikhailov, S. A. Dvoretsky, and A. V. Kolesnikov, *Topological surface states in thick partially relaxed HgTe films*, Phys. Rev. B **99**, 195423 (2019).

[96] D. A. Kozlov, Z. D. Kvon, E. B. Olshanetsky, N. N. Mikhailov, S. A. Dvoretsky, and D. Weiss, *Transport Properties of a 3D Topological Insulator based on a Strained High-Mobility HgTe Film*, Phys. Rev. Lett. **112**, 196801 (2014).

[97] Z. D. Kvon, S. N. Danilov, D. A. Kozlov, C. Zoth, N. N. Mikhailov, S. A. Dvoretskii, and S. D. Ganichev, *Cyclotron resonance of Dirac fermions in HgTe quantum wells*, JETP Lett. **94**, 816–819 (2012).

[98] T. Ando, A. B. Fowler, and F. Stern, *Electronic properties of two-dimensional systems*, Rev. Mod. Phys. **54**, 437–672 (1982).

[99] R. G. Mani, J. H. Smet, K. von Klitzing, V. Narayanamurti, W. B. Johnson, and V. Umansky, *Demonstration of a* 1/4*-Cycle Phase Shift in the Radiation-Induced Oscillatory Magnetoresistance in* GaAs/AlGaAs *Devices*, Phys. Rev. Lett. **92**, 146801 (2004).

[100] A. A. Dobretsova, A. D. Chepelianskii, N. N. Mikhailov, and Z. D. Kvon, *Spin mixing between subbands and extraordinary Landau-level shift in wide HgTe quantum wells*, Phys. Rev. B **98**, 155310 (2018).

[101] I. A. Dmitriev, A. D. Mirlin, D. G. Polyakov, and M. A. Zudov, *Nonequilibrium phenomena in high Landau levels*, Rev. Mod. Phys. **84**, 1709–1763 (2012).

[102] A. C. Durst, S. Sachdev, N. Read, and S. M. Girvin, *Radiation-Induced Magnetoresistance Oscillations in a 2D Electron Gas*, Phys. Rev. Lett. **91**, 086803 (2003).

[103] V. Ryzhii, *Photoconductivity Characteristics in Thin Films Subjected to Crossed Electric and Magnetic Fields*, Sov. Phys. Solid State **11**, 2078 (1970).

[104] I. A. Dmitriev, A. D. Mirlin, and D. G. Polyakov, *Cyclotron-Resonance Harmonics in the ac Response of a 2D Electron Gas with Smooth Disorder*, Phys. Rev. Lett. **91**, 226802 (2003).

[105] I. A. Dmitriev, M. G. Vavilov, I. L. Aleiner, A. D. Mirlin, and D. G. Polyakov, *Theory of the oscillatory photoconductivity of a two-dimensional electron system*, Physica E Low Dimens. Syst. Nanostruct. **25**, 205–211 (2004).

[106] I. A. Dmitriev, M. G. Vavilov, I. L. Aleiner, A. D. Mirlin, and D. G. Polyakov, *Theory of microwave-induced oscillations in the magnetoconductivity of a two-dimensional electron gas*, Phys. Rev. B **71**, 115316 (2005).

[107] A. D. Chepelianskii and D. L. Shepelyansky, *Microwave stabilization of edge transport and zero-resistance states*, Phys. Rev. B **80**, 241308 (2009).

[108] Y. M. Beltukov and M. I. Dyakonov, *Microwave-Induced Resistance Oscillations as a Classical Memory Effect*, Phys. Rev. Lett. **116**, 176801 (2016).

[109] D. Konstantinov and K. Kono, *Novel Radiation-Induced Magnetoresistance Oscillations in a Nondegenerate Two-Dimensional Electron System on Liquid Helium*, Phys. Rev. Lett. **103**, 266808 (2009).

[110] D. Konstantinov and K. Kono, *Photon-Induced Vanishing of Magnetoconductance in 2D Electrons on Liquid Helium*, Phys. Rev. Lett. **105**, 226801 (2010).

[111] R. Yamashiro, L. V. Abdurakhimov, A. O. Badrutdinov, Y. P. Monarkha, and D. Konstantinov, *Photoconductivity Response at Cyclotron-Resonance Harmonics in a Nondegenerate Two-Dimensional Electron Gas on Liquid Helium*, Phys. Rev. Lett. **115**, 256802 (2015).

[112] M. Khodas and M. G. Vavilov, *Effect of microwave radiation on the nonlinear resistivity of a two-dimensional electron gas at large filling factors*, Phys. Rev. B **78**, 245319 (2008).

[113] I. A. Dmitriev, M. Khodas, A. D. Mirlin, D. G. Polyakov, and M. G. Vavilov, *Mechanisms of the microwave photoconductivity in two-dimensional electron systems with mixed disorder*, Phys. Rev. B **80**, 165327 (2009).

[114] D. B. Tanner, *Optical Effects in Solids* (Cambridge University Press, 2019).

[115] C. Rigaux, "Interband magnetooptics in narrow gap semiconductors", in *Narrow Gap Semiconductors Physics and Applications*, edited by W. Zawadzki (Springer Berlin Heidelberg, Berlin, Heidelberg, 1980), 110–124.

[116] M. I. Dyakonov, A. L. Efros, and D. L. Mitchell, *Magnetic Freeze-Out of Electrons in Extrinsic Semiconductors*, Phys. Rev. **180**, 813–818 (1969).

[117] V. J. Goldman, H. D. Drew, M. Shayegan, and D. A. Nelson, *Observation of Impurity Cyclotron Resonance in $Hg_{1-x}Cd_xTe$*, Phys. Rev. Lett. **56**, 968–971 (1986).

[118] T. M. Lifshitz and Y. F. Nad', *Photoconductivity in germanium alloyed with V group elements when the photon energies are lower than the admixture ionization energy*, Dokl. Akad. Nauk SSSR **162**, 801 (1965), [Sov. Phys.-Doklady **10**, 532 (1965)].

[119] E. M. Gershenzon, G. N. Gol'tsman, and N. G. Ptitsina, *Submillimeter spectroscopy of semiconductors*, Zh. Eksp. Teor. Fiz. **64**, 587–598 (1973), [Sov. Phys. JETP **37**, 299–304 (1973)].

[120] A. Inhofer, S. Tchoumakov, B. A. Assaf, G. Fève, J. M. Berroir, V. Jouffrey, D. Carpentier, M. O. Goerbig, B. Plaçais, K. Bendias, D. M. Mahler, E. Bocquillon, R. Schlereth, C. Brüne, H. Buhmann, and L. W. Molenkamp, *Observation of Volkov-Pankratov states in topological HgTe heterojunctions using high-frequency compressibility*, Phys. Rev. B **96**, 195104 (2017).

[121] D. M. Mahler, J.-B. Mayer, P. Leubner, L. Lunczer, D. D. Sante, G. Sangiovanni, R. Thomale, E. M. Hankiewicz, H. Buhmann, C. Gould, and L. W. Molenkamp, *Interplay of Dirac Nodes and Volkov-Pankratov Surface States in Compressively Strained HgTe*, Phys. Rev. X **9**, 031034 (2019).

[122] S. Tchoumakov, V. Jouffrey, A. Inhofer, E. Bocquillon, D. Carpentier, and M. O. Goerbig, *Volkov-Pankratov states in topological heterojunctions*, Phys. Rev. B **96**, 201302 (2017).

[123] G. Abstreiter, J. P. Kotthaus, J. F. Koch, and G. Dorda, *Cyclotron resonance of electrons in surface space-charge layers on silicon*, Phys. Rev. B **14**, 2480–2493 (1976).

[124] J. N. Hancock, J. L. M. van Mechelen, A. B. Kuzmenko, D. van der Marel, C. Brüne, E. G. Novik, G. V. Astakhov, H. Buhmann, and L. W. Molenkamp, *Surface State Charge Dynamics of a High-Mobility Three-Dimensional Topological Insulator*, Phys. Rev. Lett. **107**, 136803 (2011).

[125] O. V. Kibis, O. Kyriienko, and I. A. Shelykh, *Structure of surface electronic states in strained mercury telluride*, New J. Phys. **21**, 043016 (2019).

[126] E. G. Novik, A. Pfeuffer-Jeschke, T. Jungwirth, V. Latussek, C. R. Becker, G. Landwehr, H. Buhmann, and L. W. Molenkamp, *Band structure of semimagnetic* $Hg_{1-y}Mn_yTe$ *quantum wells*, Phys. Rev. B **72**, 035321 (2005).

Acknowledgements

Finally, I would like to use the last and probably most important pages of my thesis to thank all the people that helped me on my way.

First of all, a sincere and warm-hearted thanks to Sergey, who supported and motivated me all along the way. Thank you for giving me the fantastic opportunity to do my dissertation in your group, even though I initially did not plan on doing one. The great working atmosphere in your group nevertheless convinced me to stay. I don't want to imagine what I would have missed if I decided otherwise.

Special thanks goes also to Vanya for countless long discussions on questions of mine, theory support in many joint publications, as well as for taking the time to proofread my thesis and providing a lot of helpful comments. Furthermore, I also want to thank Grisha Budkin for theoretical support, the VPS energy calculation of the $Cd_{0.15}Hg_{0.85}Te$ alloy, and band structure calculations of HgTe quantum wells.

On top of that, I would like to thank my collaborators from the Rzhanov institute in Novosibirsk, Dima Kvon, Dima Kozlov, and Maxim Savchenko for the excellent time we had together in the lab as well as for sharing your knowledge with me and answering all my stupid questions. Moreover, also huge thanks to the growth team of the Rzhanov institute including Nikolai Mikhailov, Sergey Dvoretsky, and all the guys involved in the fabrication process for providing us with high-quality HgTe and CdHgTe wafers on demand. Concerning sample fabrication, I also thank Johannes Ziegler for clean room support, help, and for sharing his expertise on the preparation of MCT-based samples with me.

Kind and open-hearted thanks also go to Stefan, Susi, Erwin, and Marcel for the great time and fun we had together, as well as for proofreading my manuscript. In the same way, I also want to thank our technician Christian not only for realizing the technical improvements I had in mind, but also for the many diverting lab talks we had in the last years. Apart from the active members of our group, I also thank our alumni, especially Helene Plank, Kathrin-Maria Dantscher, Tobias Herrmann, and Philipp Faltermeier for handing over their knowledge to us and the good mood they radiated into the group. In addition, I want to thank Sergey Danilov, all my coauthors, and our regularly visiting guests, in particular Vasily Bel'kov, the master of physical humor. Beyond that, my thanks also go to my former Bachelor and

Master students Daniel Sacré, Kilian Diendorfer and Jonathan Neuwald and the rest of our group, as well as everyone I forgot to mention. Please don't be sad, I did not forget to mention you on purpose!

Besides that, generous and honest thanks go to my family, especially to my mom and my dad for supporting and helping me become what I am today. Likewise, I thank all my friends for their company and the possibility to carry out even the absurdest hobbies together. At last, I want to thank the most important person and love of my life Katharina. Thank you for accepting me as I am and supporting me in all situations.